POLITECNICO DI MILANO
Facoltà di Ingegneria Industriale
Dipartimento di Ingegneria Aerospaziale
Corso di Laurea Specialistica in Ingegneria Aeronautica

TIME-RESOLVED REGRESSION RATES OF PARAFFIN BASED FUELS FOR HYBRID PROPULSION

Relatore: Prof. Luigi T. DE LUCA

Tesi di Laurea di:
Giovanni Massini
Matr. 720776

Anno Accademico 2010-2011

To my Parents and to Elisabetta,
with love

ABSTRACT

Objective of this Thesis is the relative characterization of different solid fuel formulations in terms of regression rate. Solid paraffin wax is considered in the analysis. The effect on regression rate of various additives is investigated as well; nano-sized and micron-sized metals and metal hydrides were tested. Influence of chamber pressure on ballistics of paraffin fuel was also evaluated.

Experimental investigations were carried out at the Space Propulsion Laboratory of Politecnico di Milano (SPLab) in a lab-scale 2D-radial microburner by a time-resolved non intrusive optical technique.

Combustion tests were performed on cylindrical fuel samples with a single central port perforation, under different chamber pressures ranging from 7 to 16 bar and with a volumetric flow rate of 210 Nlpm of gaseous oxygen (corresponding to an initial nominal mass flux of nearly 390 kg/m^2s).

A time-resolved technique for regression rate measurement developed at SPLab was used to determine solid fuel regression rate and other ballistic parameters.

Reference solid paraffin wax-based tested fuel formulation (SW) was a mixture of paraffin with 10% (by mass) of stearic acid and 2% (by mass) of graphite. SW fuel ballistics was compared to HTPB (Hydroxyl-terminated polybutadiene) fuel burnt under similar conditions, with the aim of evaluating regression rate enhancement achieved by paraffin-based fuel with respect to HTPB.

The effects of pressure on SW fuel regression rate was explored over the range 7 to 16 bars, allowing to find a definite pressure dependence under the investigated conditions. SW fuel showed an increasing regression rate enhancement for decreasing pressure.

Various kinds of additives were used as doping for SW fuel, leading to further regression rate enhancements over HTPB baseline. At the investigated operating conditions and at an oxidizer mass flux of 200 kg/m^2s, hydrides doped paraffin-based fuels exhibited percent regression rate enhancements with respect to HTPB baseline that range from 267% for aluminum hydride doped fuel to 448% achieved by fuel formulation loaded with lithium aluminum hydride.

Also metal additives allowed to enhance paraffin-based fuel regression rate. Magnesium-boron composite additive (MgB), two types of micron-sized aluminum powders and nano-sized iron powder, enabled regression rate enhancement. Percent increase with respect to baseline ranges from 223% for micron-aluminum flaked doped fuel to 308% of nano-iron additivated SW.

Keywords: hybrid propulsion, paraffin wax, ballistics, metal hydrides

ESTRATTO

Motivazioni

Gli endoreattori chimici a propellenti ibridi, diversamente dai propulsori spaziali a liquido e a solido, sono stati poco studiati nel corso degli anni e hanno visto scarse applicazioni pratiche, a causa delle difficoltà intrinseche che tali tipi di propulsori presentano.

Un endoreattore ibrido presenta un'architettura intermedia tra quella dei propulsori a liquido e quella dei propulsori a solido (vedi Figura 1).

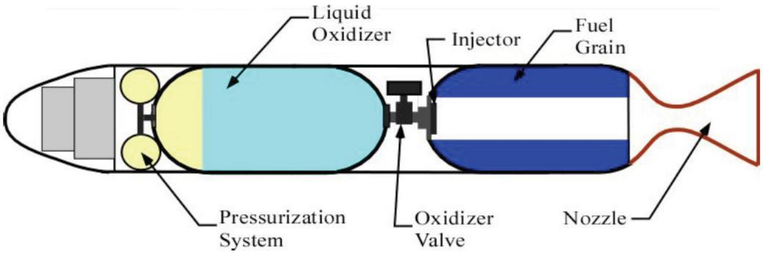

Figura 1: Configurazione generale di un tipico endoreattore ibrido (configurazione di ibrido diretto).

Gli ibridi infatti prevedono la presenza di un propellente solido (solitamente il combustibile) disposto in una camera di combustione, e di un propellente liquido o gassoso (normalmente l'ossidante) contenuto in un serbatoio separato. La perforazione presente nel grano solido consente il passaggio del flusso di ossidante, così che sulla superficie del grano si instauri uno strato limite fluidodimanico che diventa sede di una fiamma di diffusione turbolenta; la combustione è pertanto dominata dal flusso di ossidante. Queste caratteristiche consentono ai motori ibridi di unire i vantaggi dei due tipi propulsori tradizionali a propellenti liquido e solido:

- sicurezza intrinseca. Combustibile e ossidante sono conservati e installati nel propulsore separatamente, eliminando il rischio di accensioni accidentali;

- flessibilità operativa. Analogamente ai propulsori a liquido, gli ibridi permettono modulazione della spinta mediante la regolazione del flusso di ossidante, nonché possibilità di accensioni e spegnimenti multipli;

- affidabilità operativa. Per la natura stessa del tipo di combustione che vi si instaura, i motori ibridi non risentono di eventuali difetti del grano di propellente solido, quali cricche, rotture o distacchi;
- semplicità realizzativa. Rispetto ai propulsori a liquido, gli ibridi necessitano solo della metà dei componenti necessari per lo stoccaggio e la gestione del propellente liquido;
- costi inferiori. I vantaggi legati alla maggiore sicurezza consentono anche costi di gestione inferiori;
- ridotto impatto ambientale. Generalmente i propellenti ibridi utilizzano coppie di combustibile-ossidante poco inquinanti anche a livello di prodotti di combustione.

Esistono tuttavia alcuni svantaggi legati alla realizzazione e all'impiego pratico di questi propulsori:

- bassa velocità di regressione del grano. Risulta essere il maggiore impedimento alla realizzazione di motori ibridi, soprattutto su grande scala;
- bassa qualità di combustione. Gli ibridi presentano una combustione 'ruvida' e una bassa efficienza di combustione (circa il 95%);
- variazione temporale dei parametri di combustione: questa caratteristica rende difficoltoso l'effettivo controllo della spinta mediante la regolazione della portata di ossidante.

Negli ultimi anni si è visto un rinnovato interesse nei confronti della propulsione idrida, grazie ai citati vantaggi specifici che essa comporta rispetto ai propulsori tradizionali. La ricerca ha puntato soprattutto sul superamento del principale limite, la bassa velocità di regressione. E' in questo frangente che il presente lavoro di tesi si inserisce.

I combustibili a base di paraffina, come altri combustibili solidi come cherosene e pentano criogenici, offrono interessanti prospettive per la propulsione ibrida. Essi formano uno strato liquido di bassa viscosità e tensione superficiale sulla superficie di regressione del grano durante la combustione. L'iniezione dell'ossidante gassoso provoca il trascinamento (*entrainment*) delle gocce di combustibile liquefatto, che vengono poi trascinate dal flusso gassoso, incrementando la velocità di regressione. Questo meccanismo permette velocità di regressione molto superiori (fino a 3 o 4 volte [29][27]) per almeno due motivi: le gocce non assorbono calore di vaporizzazione ma solo di fusione, normalmente più basso, e, in secondo luogo, l'effetto di bloccaggio dello scambio termico convettivo è più basso dato che il flusso gassoso dalla superficie è ridotto.

Obiettivi

L'obiettivo è stato quello di investigare la balistica di combustibili per propulsori spaziali ibridi a base di paraffina. La formulazione di riferimento a base di paraffina, una miscela di paraffina, acido stearico (10% in massa) e grafite (2% in massa) denominata SW, è stata investigata a diverse pressioni di camera con lo scopo di valutare l'effetto della pressione sulla velocità di regressione.

Tale formulazione di riferimento è stata poi additivata con l'aggiunta di diversi additivi energetici, quali polveri di metallo, nano e micrometriche, e idruri di metallo. L'ossidante utilizzato durante tutte le combustioni è stato ossigeno puro.

Le diverse campagne sperimentali intraprese sono state realizzate con la linea sperimentale ibrida, presente presso il Laboratorio di Propulsione Spaziale del Politecnico di Milano (SPLab). La linea ha permesso di eseguire test balistici mediante l'analisi di riprese video della combustione di provini a geometria cilindrica a singola perforazione centrale. Le condizioni operative delle combustioni intraprese sono state quelle di alto flusso di ossidante (210 Nlpm, pari ad un flusso specifico iniziale di circa 390 kg/m^2s) e di pressioni di camera variabili dai 7 ai 16 bar.

Linea sperimentale

La linea sperimentale utilizzata consente di impostare tutti i parametri relativi alla prova di combustione, in particolare modificando la portata di ossidante, la pressione in camera di prova e il tipo di combustibile e di ossidante. I diversi elementi della linea sperimentale, mostrata in Figura 2, sono:

- camera di prova. Camera di combustione nella quale è posizionato il provino;
- apparato di ignizione laser. Ignisce la carica pirotecnica presente nella perforazione centrale dei provini avviando così la combustione;
- apparato di iniezione dell'ossidante. Consente l'introduzione e la regolazione del flusso di ossidante in camera;

- sistema di controllo della pressione. Permette il mantenimento della pressione nel corso della prova;

- sistema acquisizione dati. Costituito da un oscilloscopio collegato al trasduttore di pressione, permette di raccogliere dati per studiare la qualità della combustione;

- impianto di acquisizione video. Acquisisce in digitale i filmati di combustione per la successiva analisi.

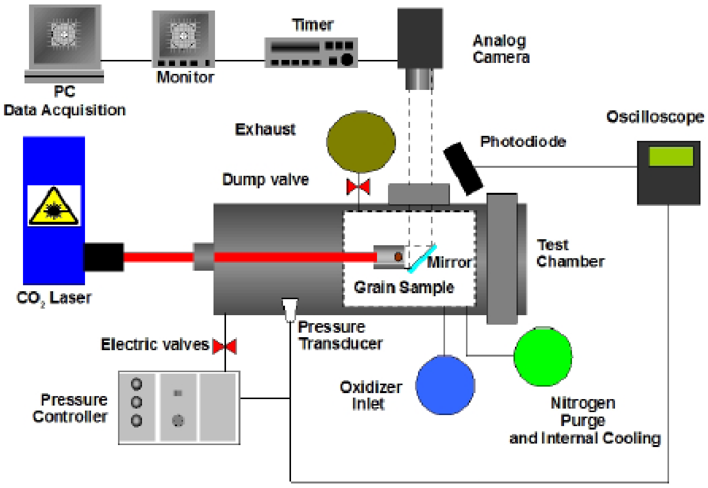

Figura 2: Schema della linea sperimentale impiegata [15].

Analisi dei test di combustione

I filmati ottenuti hanno permesso di campionare l'andamento del diametro medio della perforazione centrale nel tempo. L'insieme dei diametri raccolti è stato poi interpolato mediante un'opportuna legge a potenza, ottenendo una funzione continua dei diametri nel tempo ($\overline{D}(t)$):

$$\overline{D}(t) - D_0 = a_D \left(t - t_0\right)^{n_D} \qquad t \geq t_{ign} > t_0 \tag{1}$$

Tale interpolazione è stata eseguita per ogni test singolo a partire da un tempo di ignizione ad hoc (t_{ign}) definito in modo da massimizzare la qualità dell'interpolazione (R^2). Da questa funzione continua è stato possibile calcolare gli andamenti nel tempo del flusso specifico di ossidante (G_{Ox}), della portata massica di combustibile ($\dot{m}_f$) e del rapporto di miscela (O/F). Infine, sulla base della teoria classica della propulsione ibrida (il modello di Marxman e collaboratori), si è prodotta un'approssimazione a potenza della velocità di regressione (r_f) in funzione del flusso specifico di ossidante:

$$r_f(G_{Ox}) = \, a_r \, G_{Ox}^{n_r} \tag{2}$$

I dati così raccolti ed elaborati per ciascun test singolo sono stati poi condensati in curve d'insieme (*ensemble*), una per ciascuna formulazione investigata.

Risultati sperimentali

Le campagne sperimentali intraprese hanno portato alla caratterizzazione balistica di diverse formulazioni di combustibile a base di paraffina, nello specifico:

Tabella 1: Sommario delle formulazioni investigate.

Formulazioni investigate	Flusso di ossidante [$Nlpm$]	Pressione [bar]
SW	210	16
SW	210	13
SW	210	7
SW w/o SA	210	16
SW w MgB	210	16
SW w nFe	210	10
SW w AlH_3	210	16
SW w MgH_2	210	16
SW w LAH	210	16
SW w 3LAH	210	16
SW w μAl	210	16
SW w μAl Flaked	210	16

Nelle condizioni operative investigate, tutti i combustibili a base di paraffina hanno esibito notevoli incrementi in termini di velocità di regressione rispetto al combustibile HTPB considerato come *baseline*. Le rispettive leggi di approssimazione a potenza sono mostrate nelle Tabelle 2, 3 e 4, e risultano concordi con i valori tipicamente riportati in letteratura. Le formulazioni SW hanno mostrato incrementi percentuali di r_f, rispetto ad HTPB testato alle stesse condizioni operative, del 293% a 7 bar, 231% a 13 bar e 187% a 16 bar (per un flusso specifico di ossidante di 200 kg/m^2s).

Nella Figura 3 è possibile stimare la non trascurabile dipendenza dalla pressione in camera (p_c) esibita dal combustibile SW, rappresentata dalla risultante legge di interpolazione (Equazione 3).

$$r_f\,(G_{Ox}, p_c) = (0.062 \pm 0.018)\, G_{Ox}^{(0.879\pm0.045)} p_c^{(-0.415\pm0.069)} \qquad R^2 = 0.908 \quad (3)$$

Le formulazioni additivate con idruri e metalli, grazie al loro ulteriore apporto energetico, hanno consentito di raggiungere superiori incrementi della velocità di regressione, sia rispetto al combustibile di riferimento a base di paraffina, SW, sia rispetto al combustibile HTPB, come mostrato nelle successive figure (Figure 4, 5, 6, 7 e 8).

Le formulazioni SW additivate hanno esibito incrementi percentuali di r_f, rispetto ad HTPB testato alle stesse condizioni operative, che vanno dal 267% per idruro di alluminio (AlH_3) al 448% per litio alluminio idruro (LAH) nel caso degli idruri, e dal 223% per micro-alluminio Flaked (μAl Flaked) al 308% per nano-ferro (nFe) per i metalli impiegati (per un flusso specifico di ossidante di 200 kg/m^2s).

Parole chiave: propulsione ibrida, paraffina, balistica, idruri

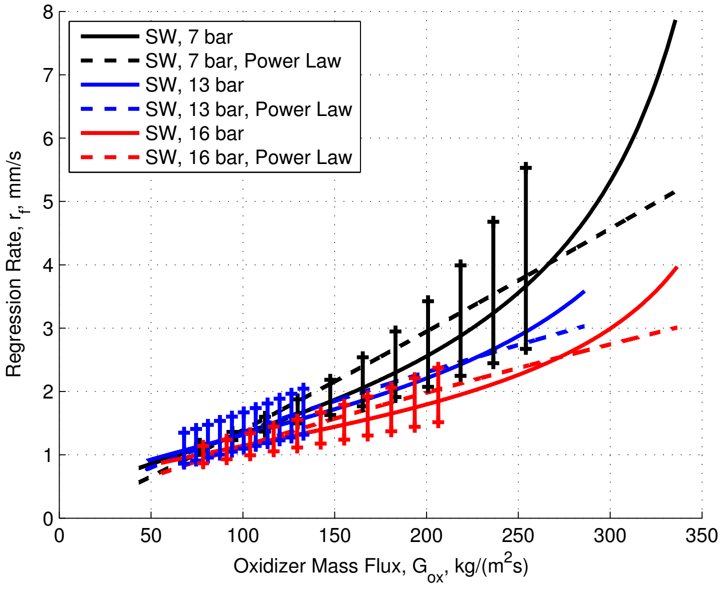

Figura 3: SW testata alle diverse pressioni (7, 13, 16 bar): velocità di regressione in funzione del flusso specifico di ossidante, curve d'insieme.

Tabella 2: SW testata alle diverse pressioni (7, 13, 16 bar): approssimazione con legge a potenza delle curve d'insieme della velocità di regressione in funzione del flusso specifico di ossidante.

Formulazione	a_r	n_r	R^2
SW, 7 bar	0.001 ± .0001	1.083 ± .0028	0.936
SW, 13 bar	0.040 ± .0003	0.765 ± .0014	0.966
SW, 16 bar	0.028 ± .0003	0.805 ± .0021	0.939

Tabella 3: SW caricata con idruri testata a 16 bar: approssimazione con legge a potenza delle curve d'insieme della velocità di regressione in funzione del flusso specifico di ossidante.

Formulazione	a_r	n_r	R^2
SW w/o SA	0.054 ± .0003	0.718 ± .0011	0.977
SW w 11.2% AlH_3	0.036 ± .0003	0.791 ± .0014	0.970
SW w 9.8% MgH_2	0.023 ± .0002	0.900 ± .0018	0.961
SW w 7.1% LAH	0.021 ± .0001	0.957 ± .0011	0.988
SW w 5% 3LAH	0.012 ± .0002	1.053 ± .0033	0.909

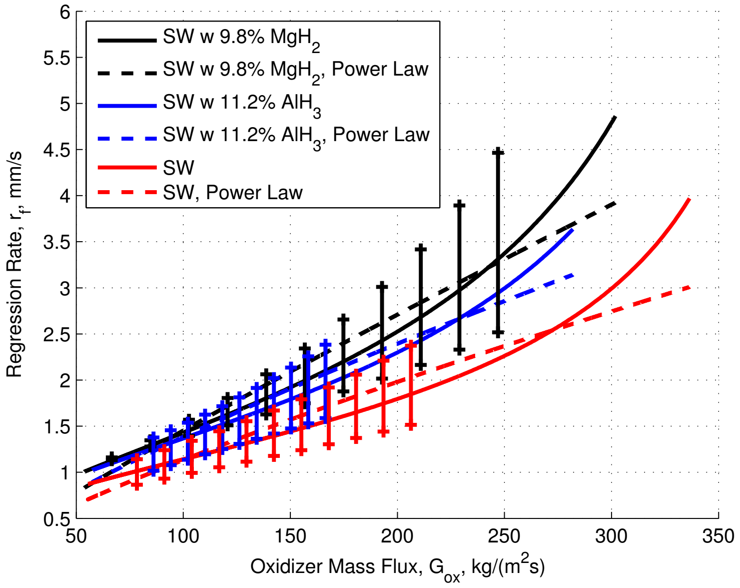

Figura 4: SW caricata con AlH_3 e MgH_2 testata a 16 bar: velocità di regressione in funzione del flusso specifico di ossidante, curve d'insieme.

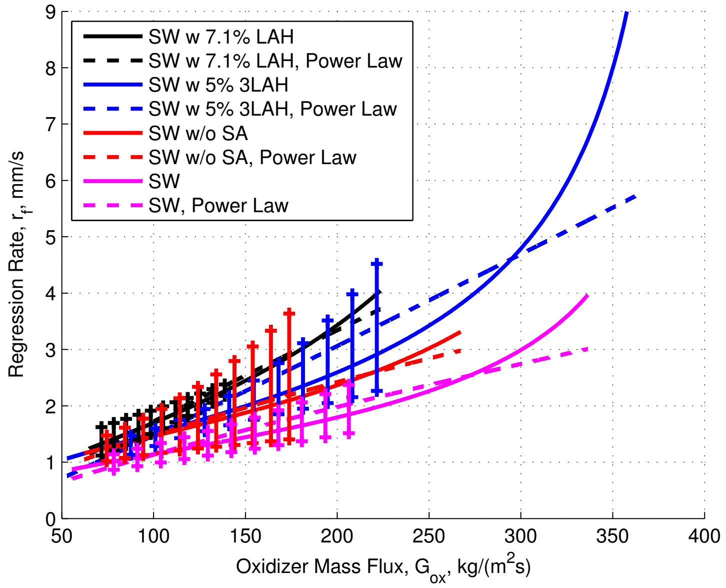

Figura 5: SW caricata con LAH e 3LAH testata a 16 bar: velocità di regressione in funzione del flusso specifico di ossidante, curve d'insieme.

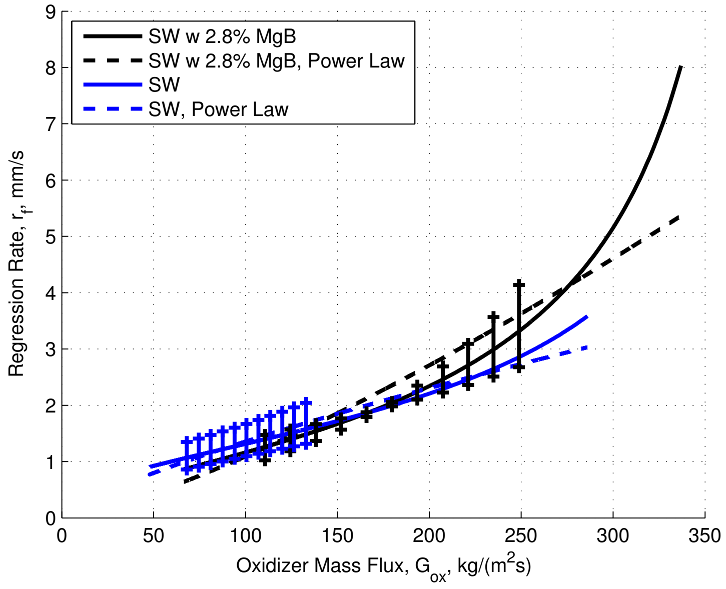

Figura 6: SW caricata con MgB testata a 13 bar: velocità di regressione in funzione del flusso specifico di ossidante, curve d'insieme.

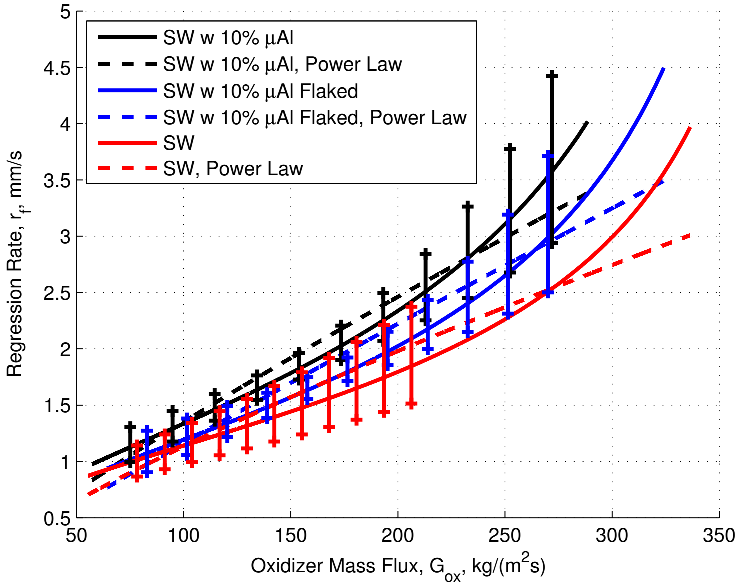

Figura 7: SW caricata con μAl e μAl Flaked testata a 16 bar: velocità di regressione in funzione del flusso specifico di ossidante, curve d'insieme.

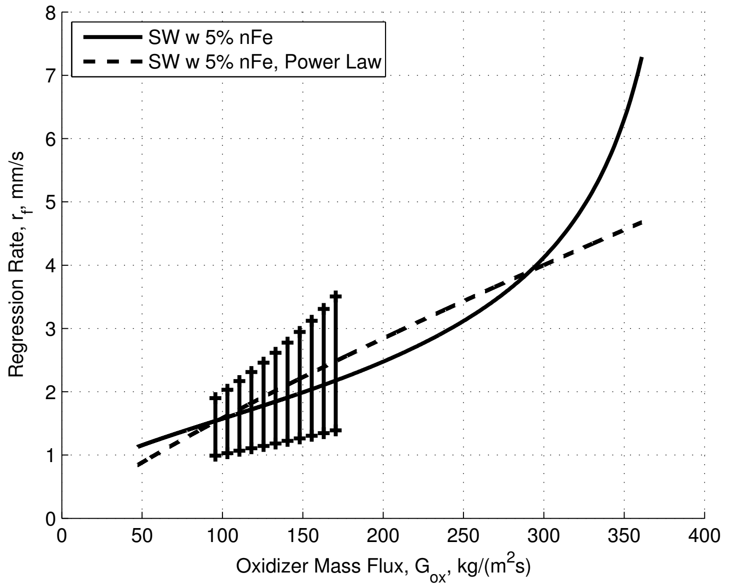

Figura 8: SW caricata con nFe testata a 10 bar: velocità di regressione in funzione del flusso specifico di ossidante, curva d'insieme.

Tabella 4: SW caricata con metalli: approssimazione con legge a potenza delle curve d'insieme della velocità di regressione in funzione del flusso specifico di ossidante.

Formulazione	a_r	n_r	R^2
SW w 2.8% MgB	0.003 ± .0000	1.310 ± .0033	0.942
SW w 10% μAl	0.025 ± .0002	0.867 ± .0016	0.968
SW w 10% μAl Flaked	0.016 ± .0002	0.936 ± .0021	0.951
SW w 5% nFe	0.033 ± .0005	0.844 ± .0027	0.909

CONTENTS

LIST OF FIGURES

LIST OF TABLES

CHAPTER

1

INTRODUCTION

1.1 Motivations

Despite being born at the same time of solid and liquid rocket propulsion systems, hybrid rockets have been the least studied and used during the years, this for reasons both economic, political and practical. Recently hybrid propulsion has returned to the world's attention thanks to a practical application, the *SpaceShipOne* project, that completed the first manned private spaceflight in 2004.

In an hybrid rocket system propellants are stored in two different states of matter, solid and liquid (or gaseous). Two main types of hybrid rocket configurations exist, in the "direct hybrid" type, the fuel, typically a hydrocarbon, is in the solid state and a liquid (or gaseous) oxidizer is stored in a separate tank. The "reverse hybrid", by far less common, presents the opposite propellant configuration, with a solid oxidizer and a liquid or gaseous fuel.

Hybrid motors general configuration, shown in Figure 1.1, is an intermediate between that of solid and liquid propulsion systems. Liquid or gaseous propellant is stored in a pressurized tank, like in liquid rockets, while solid fuel is formed into a grain acting as the combustion chamber, in a way similar to solid fuel rocket motors. In the most common configuration the oxidizer is injected by an injector into the head end of the combustion chamber and burning of the fuel and oxidizer occurs in the fluid-dynamic boundary layer that is developed along the surfaces of the solid fuel. In the case of direct hybrid, fuel is evaporated off the surface and reacts with the oxidizer in the oxidizer-rich core flow. After that the flow pass in a post-combustion chamber where burning processes are completed. Then the produced hot gases are emitted through a gas-dynamic nozzle for propulsive purposes.

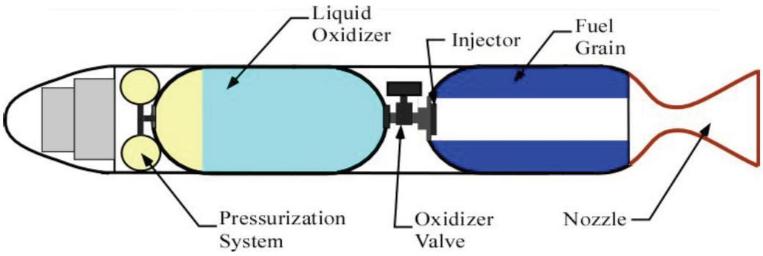

Figure 1.1: Hybrid rocket propulsion system configuration (direct hybrid configuration).

With the use of propellants in two different aggregation states, hybrid motors combine the advantages of solid-propellant motors to those of the liquid-propellant ones:

- intrinsic safety: fuel and oxidizer are stored and installed separately, thus eliminating the risk of accidental ignition and explosion due to shock, vibration, or static electricity. In addition, only inert materials are used in all the phases (manufacturing, assembly, transport operations). In case of emergencies the engine can be switched off simply interrupting the flow of the liquid propellant;

- operational flexibility: these engines allow a modulation of thrust acting on the flow of oxidizer entering in the combustion chamber, as well as engine multiple ignitions and shutdowns. So hybrid motors are throttleable as liquid ones, this feature provides a great advantage over solid motors, in which thrust modulation is allowed only by the careful choice of the propellant grain geometry that can only be imposed a priori;

- operational reliability: hybrid motors have a reduced thermal sensitivity compared to solid motors, also the propellant grain tolerates potential manufacturing or operating defects, as breakage, cracks, detachments. This latter feature is due to the diffusive flame position, being situated inside the boundary layer and not on the surface of the propellant, so possible flame insertions in propellant cracks with disastrous effects are impossible;

- simplicity: hybrid propulsion systems have a higher simplicity of construction than that of liquid motors, needing only half of the components necessary to manage a liquid propellant (tanks, pipelines, pumps);
- lower costs: hybrid propellants are economical, the costs for transport, storage and safety are contained, also because of lower cautions needed using safe propellants;
- reduced environmental impact: less polluting oxidizers and fuels can be utilized, also hybrid motors can provide non-toxic gas combustion products [14];
- flexibility in the choice of propellant: numerous hybrid propellant formulations are currently being studied. For example, NASA considered the idea of using the waste products of the ISS bounded with HTPB (hypothesis rejected for the inability to guarantee reliable physical properties because of the variable composition of waste products) [3].

However hybrid systems present also some disadvantages compared to traditional forms of space propulsion:

- low regression rate of solid grain: as mentioned before, this phenomenon inevitably limits the thrust of the engine, especially with simple grain geometries;
- low combustion efficiency: hybrids presents rough combustion and low combustion efficiency with respect to solid (equal metal loading) and liquid motors. The efficiency of typical hybrid systems is around 95%, while solid and liquid engines can reach values of 98-99% [1];
- time shifting of involved quantities: the time variation of the main parameters that govern the engine operation (oxidizer to fuel ratio, geometry of the grain port, fluid-dynamic characteristics) makes the effective control of the thrust by the oxidizer flow particularly complex.

As previously stated, the nature of hybrid rocket motors, with separated storage of fuel and oxidizer, leads to the formation of a diffusion flame situated in the fluid-dynamic boundary layer. The energy released by the flame promotes the vaporization of the fuel grain, so the combustion process is governed and regulated by the flow of the oxidizer to the fuel and the process of heat transfer to evaporate fuel from the surface. The thrust from a hybrid motor is thus regulated by the oxidizer flow rate which allows to control the overall fuel mass flow rate, a number of other parameters concur in the process, including: internal surface area, fuel port geometry, fuel and oxidizer type.

The diffusive nature of flame and the high energy that the fuel needs for vaporization, lead to low regression rates and thrust (compared to solid rockets) that constitute the main disadvantage of hybrid systems and have limited practical applications during the years (at least for conventional grain configurations). This limit affects especially the use of hybrid motors for very large scale systems such as launch vectors, an application that requires high levels of thrust.

Research about hybrid rocket motors and propellants mainly aims to overcome this shortcoming, one of the proposed solution being the use of liquefying propellants such as paraffin wax [27] that is the object of the present work.

1.2 Hybrid versus liquid and solid rockets

Considering the propulsive performances, hybrid propulsion systems are placed between liquid and solid engines. Hybrids present minimum and maximum specific impulses (where the maximum and minimum is in relation to the propellant used) higher than that of solids and monopropellant liquid systems but lower than that of the bipropellant liquid systems, that can reach values of 500 seconds in the case of cryogenic bipropellants [5].

The typical hybrid propellant couple oxygen/HTPB (LOX / HTPB) shows a specific impulse similar to that of bipropellant liquid couple oxygen / kerosene (LOX/RP-1) [1]. In terms of volumetric specific impulse, hybrids result inferior to solid propellant systems especially when there is the necessity of multi-port grain geometries in order to increase solid grain regression rate [1].

The overall characteristics of hybrid propulsion systems make them suitable for suborbital launchers, upper rocket stages, small satellites and de-orbiting missions. Thanks to their greater advantage, their intrinsic safety, hybrids are convenient also as engines for private access to space.

1.3 Objectives

The aim of this thesis work is to provide a ballistics characterization of paraffin-based fuels to achieve higher regression rates. Different paraffin-based fuels have been investigated, both without and with the addition of metal-based additives (both nano and micron-sized metal powders and hydrides). Furthermore paraffin fuel has been tested under different pressure conditions, in order to define the influence of pressure chamber on regression rate.

The presented experimental work has been based upon several combustion test campaigns undertaken with the experimental plant designed by the Space propulsion laboratory, SPLab, of Politecnico di Milano. This 2D-radial micro-burner has permitted the testing of samples with radial geometry. Regression rate was measured by an optical time-resolved not intrusive technique.

1.4 Presentation plan

- **Chapter 1**: introduction to this work;
- **Chapter 2**: literature survey on hybrid propulsion history with discussion of the main features of this propulsive technology, state of the art, overview of techniques for regression rate enhancement;
- **Chapter 3**: providing informations on properties and characteristics of the ingredients of the produced fuels;
- **Chapter 4**: describing fuel samples preparation procedures;
- **Chapter 5**: depicting the experimental plant used in the tests combustion;
- **Chapter 6**: illustrating the measurement procedure and the data analytical processing;
- **Chapter 7**: exposing and analyzing the results obtained;
- **Chapter 8**: conclusions of the work and possible future developments are drawn and discussed;

CHAPTER

2

DEVELOPMENT AND STATE OF THE ART OF HYBRID ROCKET PROPULSION

2.1 Hybrid rocket propulsion history

Surprisingly, some of the earliest work with rockets involved hybrid propulsion, so the birth of hybrid propulsion is to be placed in the early 30s, at the same time of that of solid and liquid propulsion. As previously mentioned, economic and political reasons hampered hybrid rocket development to the benefit of solid and liquid systems.

First hybrid rocket experimentations started in Russia in 1933, undertaken by Sergei Korolev and Mickhail Tickhonravov. Their *GIRD-09* (Figure 2.1) developed a thrust of 500 N reaching an altitude of 400 m, fueled by liquid oxygen and a mixture of petroleum with collophonium, a natural gum-resin [1] [2] [3].

Rocket societies in the German speaking world and the United States, continued small scale tests as the experiments conducted by H. Oberth in Austria in 1938-39, using liquid oxygen and a tar wood potassium nitrate fuel [2]. Others in this period used wood and coal as fuels. Afterwards,

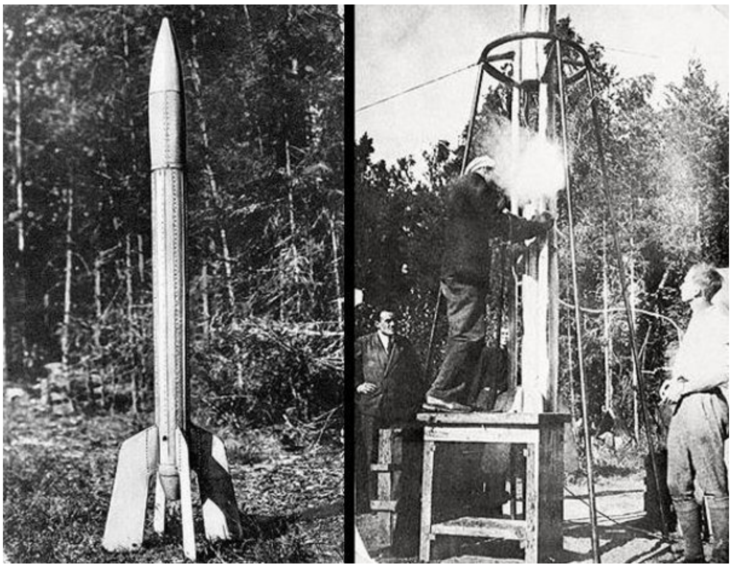

Figure 2.1: The russian *GIRD-09* with its vertical track.

between 1937 and 1943, other tests were performed in Germany. At the IG Farben laboratories, in Ludwigshafen, Andrussow, Nögerrath and Lutz tested a 10 kN hybrid motor constituted by a stack of multi-perforated coal disks burnt with gaseous nitrous oxide as oxidizer. However, all the results were unsatisfactory, as the obtained regression rates were relatively low [1].

In the United States initial research on hybrid rockets was made in the early 40s by the California Pacific Rocket Society, founded by Smith and Gordon [8]. Using liquid oxygen in combination with a wide range of fuels (wood, wax, rubbers) the society realized its maximum result with the launch of a LOX/gum fueled rocket that reached 9000 m in June 1951 [3]. With these trials was noted for the first time that hybrid systems had the ability to tolerate cracks and fissures in the solid grain. These defects could cause explosions in solid propellant rockets.

Research continued in the USA after World War II, in 1946, Bartel and Rannie while working on ramjets, developed the first theoretical model of hybrid combustion [8]. Between 1951 and 1956 Moore and Berman, of the General Electric company, investigated a hybrid motor configuration with hydrogen peroxide and polyethylene, wherewith they showed the possibility of modulating the thrust with relative ease through the control of the oxidizer flow.

Some early studies about reverse hybrids dates back to the 50s. In 1952 Dembrow and Pompa tested the first reverse hybrid rocket, using kerosene as liquid fuel in combination with various types of grains of solid oxidizer. Despite this and subsequent researches, reverse hybrids technology was never been established because of the low quality of combustion and performance, resulting too much poor to justify the increased risks and complexities of realization.

Active sponsorship of hybrid programs in the U.S. began in about 1960 when at least six organizations entered the field. In a series of research contracts sponsored by the Navy, Chemical Systems Division of United Technology Center (CSD/UTC) conducted a group of fundamental investigations on the combustion behavior and internal ballistics in hybrid motors [8]. An important step occurred in those years with the formulation of a combustion model that is still the reference hybrid combustion model. It was developed by Marxman and his team and allowed to evaluate the regression rate assuming a model of diffusive flame placed in a turbulent boundary layer [9].

During this period ONERA in France and Volvo Flygmotor in Sweden had begun a serious investigation of hybrids, designing small sounding rockets. ONERA developed a Hypergolic combination of nitric acid and metatoluene diamine/nylon [8], first flight had been in 1964, a total of eight launches had been performed, reaching 100 km of altitude. Also Volvo Flygmotor developed a program based on a Hypergolic combination, nitric acid and polybutadiene, attaining in 1969 an altitude of 80 km.

Other American flight programs were target drones requested by US Air Force (*Sandpiper*, *HAST*, and *Firebolt*) which required supersonic flight in the upper atmosphere for up to 5 minutes. These latter applications were suitable for the conventional hybrid because its very low burning rate was ideal for a long duration sustained operation. So, in the late 1960's, United Technologies (CSD/UTC) proposed the *Sandpiper*, based on a storable propellant combination composed of RON-25 as oxidizer (Nitric oxide, NO and nitrogen peroxide, N_2O_4) and a PMM-Mg fuel. The first of six flights occurred in January, 1968, this missile was larger than the ONERA rocket, its thrust duration was in excess of 300 seconds and was throttleable on demand over an 8:l range.

A second Air Force program which required a heavier payload was the *HAST* (High Altitude Supersonic Target). In contrast to the *Sandpiper*, the thrust chamber diameter was increased, the propellant changed to RFNA-PB/PIM and the oxidizer was pressurized by a ram air turbine instead of nitrogen. The grain configuration was also changed from a single cylindrical port to a cruciform one [8]. Finally the *Firebolt* was an upgraded version of the *HAST* developed in 1980 and built in 48 copies.

In the mid 80s, there were two situations which created a stimulus for reviving interest in the large hybrid rockets. The first situation arose when concern was expressed for the storage and handling of the large solid propellant segments of the Shuttle boosters. This concern was heightened after the Challenger disaster and the Titan III failure in 1986. This situation stimulated NASA to sponsor a study of the use of hybrids for the Shuttle strap-on boosters.

Four industrial groups were engaged by NASA, the hybrid motors should have at least duplicate the Shuttle solid boosters' performances. All contractors were able to match or improve the performances, But the projects showed larger diameter units and all studies suffered from the fact that ballistic data for the propellants were not available leading to a considerable divergence in the predictions among the contractors [8].

The second situation was the recognition of the growing business in commercial satellites which stimulated many nations to build their own versions of a low cost space vehicle capable of placing communication satellites in orbit.

Moving in this direction was the American Rocket Company, *AMROC*, Founded in 1985, an entrepreneurial industrial company devoted entirely to the development of large hybrid boosters. *AMROC* realized many successful tests (Figure 2.2), reaching over 300 hybrid rocket motor test firings ranging from 4.5 kN to 1.1 MN of thrust. Nevertheless *AMROC* ran into difficulties when the motor was scaled to 6 foot diameter and 250,000 lb. thrust. The low regression rate of the fuel dictated a 15 port grain design and problems of poor grain integrity were the result. In 1995 *AMROC* filed for bankruptcy.

Safety and low cost qualities of hybrid rockets have justified studies and trials up to the present day. In 1995 the Hybrid Propulsion Demonstration Program (HPDP) was promoted with the the aim of developing hybrid propellant boosters. The program involved major industries and government agencies such as NASA, DARPA (Defense Advanced Research Projects Agency), Lockheed Martin, CSD/UTC, Thiokol, Rocketdyne, Allied Signal Corporation and Environmental Aeroscience.

2.2 State of the art

The *AMROC* intellectual property was acquired in 1999 by *SpaceDev*. The latter realized the most recent advance in hybrid rockets in the Fall of 2004 when *SpaceShipOne* carried a pilot to over 100 km of altitude to win the Ansari X-prize [1]. This privately funded, sub-orbital flight ushered in a new era in space access.

SpaceShipOne was an experimental air-launched rocket-powered aircraft

Figure 2.2: A 312 kN Hybrid rocket motor tested by *AMROC*.

with suborbital flight capability that used a hybrid rocket motor. The propulsion system thought for this project used a four port motor fueled by HTPB with nitrous oxide (N_2O) as the oxidizer. The mission scheduled a preliminary transportation to a 15 km altitude performed by a mothership called *White knight*(Figure 2.3), followed by an autonomous boost phase to reach an altitude of 100 km, with subsequent return to the atmosphere in gliding flight.

The *SpaceShipTwo* (Figure 2.4), successor of *SpaceShipOne*, is currently under development by a joint venture between Scaled Composites and the Virgin Group. The Virgin Galactic, a company within Virgin Group, plans to operate a fleet of five SpaceShipTwo spaceplanes in a private passenger carrying service, starting in 2013 [43].

The theoretical advantages of hybrid systems would make it useful as substitutes for solid rocket boosters used in modern heavy launchers. In fact the employment of hybrid technology would result in a considerable increase of the payload as well as in the safety of these systems, as shown in Figure 2.5 which shows a study for the heavy launcher Ariane 5 [12]. For the same total impulse, the hybrid propellant booster would be lighter than the solid one, with a minimum disadvantage due to the increase of the cross section (drag increase) since the volumetric filling efficiency for a hybrid is lower than for a solid, because of the lower average density of the fuel.

Nevertheless, the hybrid is still not competitive in the field of boosters

Figure 2.3: *SpaceShipOne* (up) and its mothership, *White knight* (down) [44].

Figure 2.4: *SpaceShipTwo* during a flight test [43].

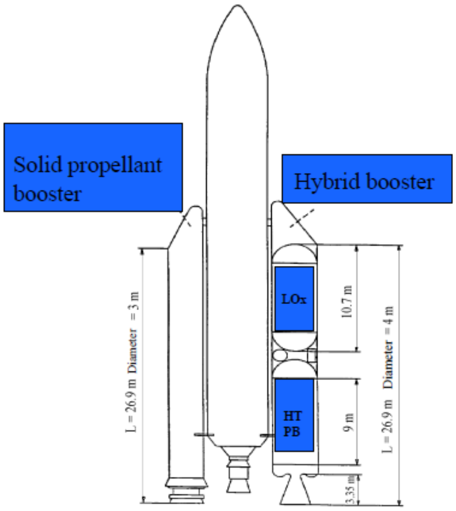

Solid-propellant booster	hybrid booster
Solid propellant : 237.0 t	HTPB : 65.1 t Oxidizer : 144.9 t Other : 9.0 t
Structure : 19.5 t	Structure : 18.0 t
Insulation : 4.7 t	Insulation : 1.0 t
Nozzle : 6.1 t	Nozzle : 6.1 t
Igniter : 0.3 t	Turbopump : 0.5 t
Structural mass : 30.6 t **Total mass : 267.6 t**	**Structural mass : 25.6 t** **Total mass : 244.6 t**

Figure 2.5: Comparison between solid and hybrid rocket booster for the Ariane 5 heavy launcher [12].

or upper stages for large space launchers, mainly because of the low regression rate which impedes to reach high values of thrust with simple grain geometry (single port perforation).

Several research groups are active in the hybrid field, with the main purpose to overcome the limitation of the low regression rate, important results have been achieved at Stanford University with the use of a class of liquefying fuels, including paraffins, that are subjected to a phenomenon called entrainment [27].

The study of fundamental mechanisms of combustion and refinement of theoretical models are being researched by K. K. Kuo and colleagues at the Pennsylvania State University. In Europe there are several active programs with the aim to study and implement hybrid systems, notably the ORPHEE (Operational Research Project on Hybrid Engine in Europe) program, funded by the European Union.

2.3 Parameters of hybrid rocket propulsion

Being systems in which the propellants are stored both in a solid and in a liquid state of matter, hybrid rockets present many important parameters in common with both these systems, like the regression rate of the solid grain r_f and the propellant mass flux G.

The regression rate is defined as the velocity with which the combustion surface of the solid grain (A_b) regresses during combustion. In the case of multi-port grain this surface is divided into multiple surfaces that characterize multiple perforation grains. These surfaces are exposed to the oxidizer flow and, after ignition, become home of the combustion.

Despite the vaporization of solid grain occurs in a complex manner in a three-dimensional domain, for its analysis, conventionally, it is assumed a linear regression rate in terms of thickness of material burned per time unit in the perpendicular direction to the surface of combustion.

At the moment no theoretical model can predict with sufficient accuracy the regression rate of a given propellant, so it can be determined only experimentally. In hybrid systems regression rate depends mainly on chemical composition of fuel and oxidizer, oxidizer mass flux and, weakly, on pressure [1].

Achieving a high regression rate is important because an increase in r_f contributes to increase the propellant flow rate leaving the nozzle $\dot{m}$, and, thus the thrust T (see Equations 2.1 and 2.2):

$$\dot{m} = \dot{m}_{Ox} + \dot{m}_f = \dot{m}_{Ox} + \rho_f r_f A_b \tag{2.1}$$

$$T = \dot{m} u_{ex} + (p_{ex} - p_a) A_{ex} \tag{2.2}$$

where $\dot{m}_{Ox}$ and $\dot{m}_f$ are the oxidizer and fuel flow rate, u_{ex}, A_{ex} and p_{ex} the velocity, the cross section and the pressure in the exhaust section of the nozzle, p_a the ambient pressure.

Another important rocket parameter is the specific impulse, it represents the thrust that a motor provides for burned propellant mass flow rate unit (Equation 2.3), in the case of adapted nozzle (that is $p_{ex} = p_a$) specific impulse is equal to the ratio between effective exhaust velocity and gravity acceleration (Equation 2.4).

$$I_{sp} = \frac{T}{\dot{m} g_0} \tag{2.3}$$

$$I_{sp} = \frac{u_{ex}}{g_0} \tag{2.4}$$

So specific impulse depends primarily on the effective exhaust velocity, which depends on regression rate through the chamber pressure p_c and on the type of propellants through γ, M and T_c, respectively the ratio between the specific heats of the exhaust gases, the mean molecular weight of the exhaust gases and the chamber temperature:

$$I_{sp} = \frac{1}{g_0}\sqrt{2\,\frac{\gamma}{\gamma-1}\,\frac{R}{M}\,T_c\left[1-\left(\frac{p_{ex}}{p_c}\right)^{\frac{\gamma-1}{\gamma}}\right]} \tag{2.5}$$

in response to an increase in the regression rate, mass flow rate increases and so chamber pressure, thus an augmented exhaust velocity, an higher thrust and specific impulse are achieved.

2.4 Internal ballistics of hybrid rockets

Combustion in hybrids systems differs considerably from that in solid and liquid motors, this comes from the fact that in hybrids, fuel and oxidizer propellants are in two different states of matter. As mentioned in Section 2.1 the first theoretical model for hybrid combustion dates back to 1946, other studies were undertaken in the 60s in Germany, France, Sweden and United States Where Marxman and colleagues developed the current reference model for solid fuel burning with gaseous oxygen. Currently theoretical studies are conducted in several universities such as Pennsylvania State University and Stanford University.

2.4.1 The Marxman model

The model developed by Marxman and colleagues [9] [10] considers that the combustion process in a hybrid system is that of a turbulent diffusion flame contained within a fluid-dynamic boundary layer, in the zone in which the stoichiometric ratio between gasified fuel and injected oxidizer is achieved.

The flame transfers energy to the surface of the solid grain, for both convection and radiation mechanisms, allowing the gasification of newly fuel mass, which, reacting with the oxidizer, supports the combustion. The convective flow transports the products of combustion downstream, this products results mixed with the oxidizer above the flame and with the fuel below. Flame divides the boundary layer in two regions. The first one extends from the regressing surface to the flame, the second from the flame to the boundary layer limits. The first region is thus rich in fuel, contrary to the oxidizer rich upper second region. Theoretically the flame is assumed to be an infinitesimal thickness layer, a line of discontinuity for temperature and composition gradients, as is shown in Figure 2.6. Actually the flame has a finite thickness and the gradients are continuous.

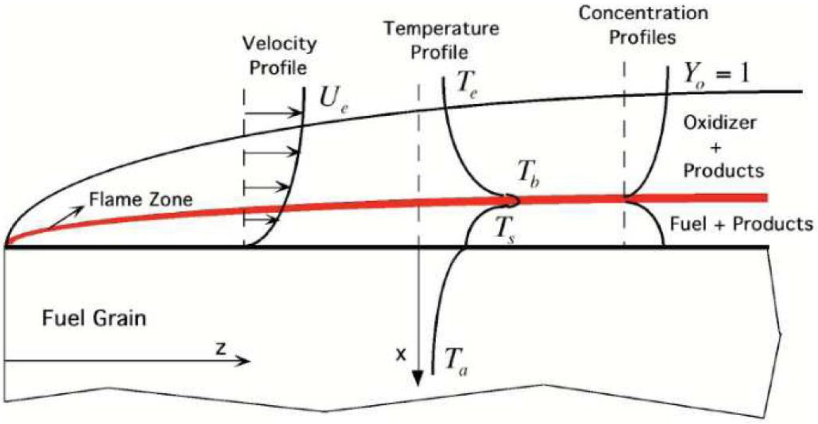

Figure 2.6: Diffusive flame structure in hybrid rocket systems: temperature, composition and velocity profiles.

The flame divides the boundary layer into two parts: in the part between the surface of the grain and the surface of the flame, the velocity and temperature gradients have a concordant trend, in the upper part, instead, the quantities have discordant trend. The speed, indeed, follows the typical trend of a boundary layer: increases monotonically from the null value at the wall, to the value of the free stream u_e. The temperature instead, grows up to a maximum in correspondence of the flame zone. Then it decreases down to the free stream value T_e.

It is possible to achieve an expression of regression rate of the solid grain, writing an energy conservation balance in terms of heat fluxes at regressing surface. Assuming hypothetically that the heat flux exchanged by conduction and radiation in the deepest parts of the solid grain are negligible (so it is assumed that the heat exchange between the flame and fuel takes place purely by convection), the following equation can be written:

$$\dot{q}_s = \rho_f \, r_f \, h_v \tag{2.6}$$

in which $\dot{q}_s$ is the wall heat flux, h_v and ρ_f the enthalpy of vaporization and the density of the solid grain respectively. The term h_v comprises different enthalpies, in the case of classical polymeric propellants it includes:

- heat needed to rise the solid grain temperature, $c_{pf}(T_w - T_i)$;
- heat needed for the depolymerization process, Δh_1;
- latent heat needed for the gasification of the monomers, Δh_2.

Where c_{pf} is the specific heat, T_w and T_i are the surface and initial temperature of the solid fuel grain. Thus the enthalpy of vaporization is given by:

$$h_v = c_{pf}(T_w - T_i) + \Delta h_1 + \Delta h_2 \tag{2.7}$$

The Heat flux of Equation 2.6 results equal to the heat flux evaluated in the boundary layer at the gas side:

$$\dot{q}_s = k_g \left.\frac{\partial T}{\partial y}\right|_{y=0} \tag{2.8}$$

Where k_g is the gas thermal conductivity and $\partial T/\partial y$ is the temperature gradient in the direction normal to the surface of the fuel. Applying the Reynolds analogy, which asserts that the transfer mechanism of turbulent enthalpy and momentum are similar (Prandtl and Lewis numbers equal to unity), the same heat flux can be rewritten in terms of Stanton number, C_h:

$$\dot{q}_s = C_h \, \rho_e \, u_e \, \Delta h \tag{2.9}$$

Δh is the enthalpy absorbed in the combustion process, equal to the enthalpy difference between the flame zone and the surface of the grain. Stanton number represents the ratio between the convective heat flux and the fluid heat capacity, and is defined as:

$$C_h = \frac{Nu_x}{Pr \; Re_x} \tag{2.10}$$

Where Nu_x, Pr and Re_x are the Nusselt, Prandtl and Reynolds numbers and x is the position along the grain perforation. Assuming the hypothesis of boundary layer on a flat plate, Stanton number can be written in terms of surface friction coefficient, C_f, and Prandtl number, Pr according to Equation 2.11:

$$C_h = \frac{C_f}{2} Pr^{-2/3} \tag{2.11}$$

substituting this expression in Equation 2.9 and equalizing Equation 2.9 to Equation 2.6 an expression of the grain regression rate can be derived:

$$r_f = \frac{C_f}{2} \frac{\Delta h}{h_v} \frac{\rho_e u_e}{\rho_f} Pr^{-2/3} \tag{2.12}$$

in which, as mentioned before, $Pr \cong 1$. The particular type of boundary layer, however, is a boundary layer with blowing, that is addition of

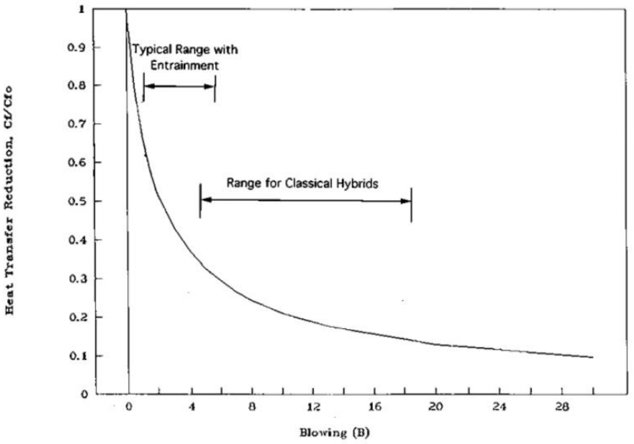

Figure 2.7: Blocking effect dependence on the blowing parameter B [3].

mass from the solid surface caused by the gasification of the fuel. The phenomenon induces a "blocking effect", causing a reduction of the convective heat exchange and a consequent decrease of regression rate. In order to take into account this effect the coefficients for friction and heat transfer must be rescaled appropriately. The relationship between the friction coefficient under blowing conditions (C_f) and without blowing (C_{f0}) has been experimentally derived by Marxman:

$$\frac{C_f}{C_{f0}} = \left[\frac{ln(1+B)}{B}\right]^{0.8} \left[\frac{1+1.3B+0.364B^2}{(1+B/2)^2\,(1+B)}\right]^{0.2} \tag{2.13}$$

where B is the nondimensional blowing parameter, that evaluates the importance of the transversal injected mass flux in the boundary layer compared to the axial free stream flux, and is defined according to Equation 2.14:

$$B = \frac{1}{C_f/2}\frac{\rho_s u_s}{\rho_e u_e} = \frac{1}{C_f/2}\frac{\dot{m}_f}{G} \tag{2.14}$$

in which $\dot{m}_f$ represents the fuel mass flow rate and G is the total mass flux, sum of oxidizer and fuel mass fluxes (G_{Ox} and $G_f(x)$). So the blowing causes a reduction of the surface friction coefficient which may be correlated to the blowing parameter as shown in Figure 2.7.

In the case of classical hybrid fuels (non liquefying fuels) the blowing parameter lies in the range $5 \leq B \leq 100$, in this range Equation 2.13 can be approximated to:

$$\frac{C_f}{C_{f0}} = 1.27B^{-0.77} \tag{2.15}$$

in a turbulent boundary layer without radiation, the blowing parameter is equal to the ratio between Δh and h_v and the zero-blowing friction coefficient C_{f0} depends on Reynolds number [1]:

$$B = \frac{\Delta h}{h_v} \tag{2.16}$$

$$\frac{C_{f0}}{2} = 0.029Re_x^{-0.2} \tag{2.17}$$

thus the regression rate equation in a pure convective model can be rewritten with these parameters:

$$r_f = 0.036\,\frac{G^{0.8}}{\rho_f}\left(\frac{\mu}{x}\right)^{0.2} B^{0.23} \tag{2.18}$$

Where μ is the oxidizer dynamic viscosity and the numerical coefficient 0.036 comes from Imperial units. From the equation it can be seen the strong dependence of regression rate on the total mass flux G, typical of hybrid systems. Furthermore no explicit dependency on the pressure results, and the fuel thermo chemical properties influence the regression rate only through the blowing parameter B.

In practical applications, the expression of regression rate is usually replaced by a more compact form, in which the coefficients are obtained experimentally:

$$r_f = a\,G^n\,x^m = a\,[G_{Ox} + G_f(x)]^n\,x^m \tag{2.19}$$

Regression rate could vary along the grain perforation length, because of the dependence of the fuel mass flux $G_f(x)$ on the coordinate x. On the other hand, the exponential coefficient relating to the boundary layer thickness growth, x^m, counteracts this effect due to its value, generally equal to -0.2. So it can be said that the regression rate is uniform along the perforation. This behavior is confirmed by experimental trials, thus a more simple regression rate law can be used:

$$< r_f(x) >= a\,L^m < G >^n \tag{2.20}$$

where $< G >$ is the mean total mass flux, evaluated as the ratio between the total mass and the mean perforation area, and L is the grain perforation lenght. It must be noted that all these relations are of an implicit type: regression rate depends on itself through the fuel mass flux $G_f(x) = G_f(r_f(x))$.

In order to bypass this shortcoming, in assigned length hybrid motors, a simpler relation can be used, linking regression rate only with measurable input parameters:

$$r_f = a_r \, G_{Ox}^{n_r} \tag{2.21}$$

in which the constant coefficients a_r and n_r have to be evaluated experimentally through a series of combustion tests, typical values for n_r range from 0.4 to 0.8. Relation 2.21 is the one used in many experimental works, including this thesis.

2.4.2 Radiation effect

Marxman's pure convective model does not consider the radiative heat transfer, however in some propellant formulations such as those based on metalized fuels, this contribution is important and not negligible. The radiation presence modifies Equation 2.22 [1]:

$$\dot{q}_s + \dot{q}_r = \rho_f \, r_f \, h_v \tag{2.22}$$

with $\dot{q}_r$ the radiation flux that comes from the flame and that hits the solid surface:

$$\dot{q}_r = \sigma \varepsilon_s (\varepsilon_g \, T_f^4 - T_s^4) \tag{2.23}$$

Where σ is the Stefan-Boltzmann constant, ε_s and T_s are respectively the emissivity coefficient and the temperature of the solid grain, T_f is the flame temperature and ε_g the emissivity coefficient of the gas phase. The presence of radiative heating enhances the regression of the solid grain, but this surplus heating increases the blocking effect leading to a decrease of convective heat transfer (blocking effect augmented). In order to take into account this effect Marxman and colleagues suggested the following correction to the blowing effect:

$$\frac{B_{rad}}{B} = 1 + \frac{\dot{q}_{rad}}{\dot{q}_{conv}} \left(\frac{B_{rad}}{B} \right)^{0.77} \tag{2.24}$$

Now a new expression to evaluate regression rate in combined convective-radiative case can be written:

$$\frac{r_f}{r_{f,conv}} = e^{\left(-0.75 \frac{\dot{q}_{rad}}{\dot{q}_{conv}}\right)} + \frac{\dot{q}_{rad}}{\dot{q}_{conv}} \tag{2.25}$$

in which $r_{f,conv}$ and $\dot{q}_{conv}$ are the values evaluated under exclusive convective heat transfer. So an increase in the energy transmitted by radiation has a contrasting effect: it corresponds to a reduction of the convective term, due to the increased blowing effect. Thus the benefit of the radiant heat flux is damped, contributing to the difficulty of obtaining high regression rates. When the radiation contribution is comparable with the convective, an enhancement in regression rate is achieved, but when the contribution of radiation is small, the increase of the radiative term and the reduction of the convective term are almost equal. For this reason the classical Marxman's theory without radiation effect remains valid if the radiative effect is quite smaller than the convective one [1].

2.4.3 Pressure effect

In the typical operating conditions of most practical applications, the regression rate is generally regarded as independent from the pressure. In the 60s Smoot and Price, shown that, at low pressure, regression rate exhibits a dependence on pressure that increases for the increasing mass fluxes [32]. This behavior is shown in Figure 2.8 in which three regions can be identified:

- low mass flux: regression rate is independent on pressure, showing a power dependence on flux with an exponential coefficient of 0.8, predicted by Marxman's model;
- high mass flux: regression rate is subjected to a strong influence by pressure and the dependence on mass flux results greatly reduced;
- Intermediate mass flux: regression rate is influenced both from pressure and from mass flux, following the relation:

$$r_f = \frac{a\,G^{0.8}\,b\,p_c^n}{a\,G^{0.8} + b\,p_c^n} \tag{2.26}$$

Where again a and n are experimentally found. Marxman and co-workers have explained this trend [11], valid for intermediate and high mass fluxes:

- at low pressure, the reaction rate is low and the process of combustion tends to that of a turbulent premixed flame, in that case the characteristic time of reaction becomes greater than the characteristic time of the turbulent transport. Thus the first becomes the limiting factor of the regression rate;

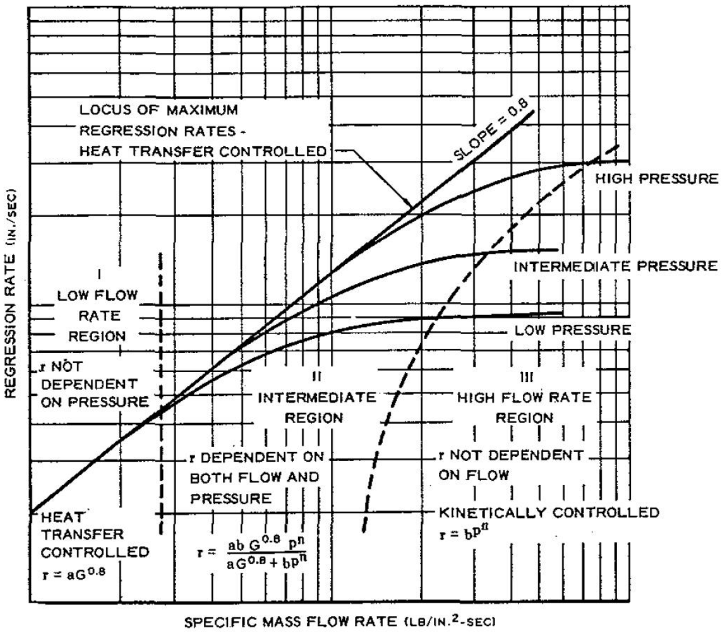

Figure 2.8: Pressure and mass flux dependence of typical nonmetalized hybrid systems [32]

- at higher pressures the reaction rate is higher because of the faster chemical kinetics, so the characteristic time of reaction is lower than the turbulent transport one, leading to higher regression rates as pressure is increased;

Looking for a relationship between the regression rate and the ratio between the two characteristic times, Marxman reached a new expression that takes into account the pressure effect:

$$r_f = a_0 \, G_{Ox}^n \, p_c^l \tag{2.27}$$

With $l = 0.5$ and $n = 0.4$. This experimental coefficients, therefore, shows that, in the regime dominated by chemical kinetics, regression rate depends on the mass flow more weakly than that is expected from Equation 2.21 and also depends on pressure.

The effects mentioned above disappear at very low mass fluxes, at these values the radiation contribution may become important in relative terms, as reported in Equation 2.25. In conclusion pressure influence to regression rate can be summarized as is shown in Figure 2.9.

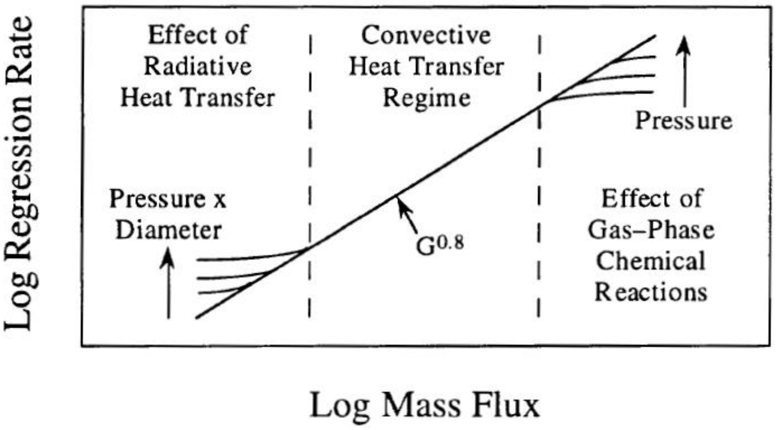

Figure 2.9: Pressure effect on hybrid combustion process [33].

2.4.4 Entrainment

Marxman's model is the classical hybrid theory for conventional polymeric fuels as HTPB. In recent years, a new class of fuels has been studied for hybrid propulsion, due to the possible regression rate enhancement that they could enable: liquefying fuels.

Conventional hybrid fuel combustion results to have a low regression rate (compared to conventional solid rockets), mainly due to the nature of the diffusion flame that characterizes this systems. In fact the physical phenomenon of heat and mass transfer from the relatively remote flame zone to the fuel surface limits the rate of vaporization of the solid grain, leading to low regression rate, low fuel mass flux and thus low thrust (with simple grain geometry).

Various methods for increasing fuel regression rates have been suggested. An effective method is to use fuels that form a low viscosity and low surface tension melt layer at the combustion surface [27]. In addition to the classical gasification, these liquefying fuels exhibit additional mass transfer mechanism resulting in the entrainment of liquid droplets from the melt layer surface (see Figure 2.10). Droplet formation is caused by liquid layer instabilities, which result from the high shear stress produced by the oxidizer flow in the port [28]. Thus, entrainment phenomenon is favored by low viscosity and low surface tension of the surface melt layer.

Usually the fuels that develop entrainment are nonpolymeric propellants that liquefy easily on heating. Representative of this class of fuels are the solid cryogenic hybrids, fuels at fluid state under ambient condition that are frozen to form solid grains. Part of this category are substances that

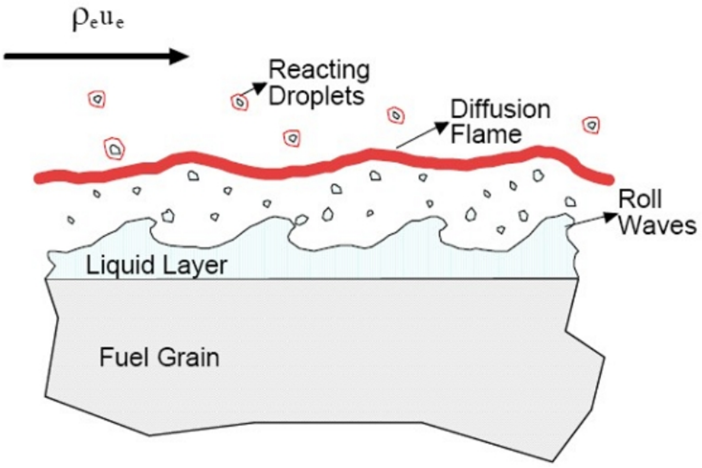

Figure 2.10: Entrainment of droplets from the melt liquid layer in a typical liquefying propellant.

range from hydrogen to low carbon number hydrocarbons, like methane and pentane. Nevertheless the use of this fuels offers remarkable complications in hybrid rocket design, because of the need of cryogenic systems that lead to an increase in structural/inert mass of the propulsive system and a loss of performances.

So the research focused on materials that are solids at standard conditions but that can experience the same formation of a low viscosity melt layer on the regressing surface. The main types of fuel of these category are the members of the homologous series of n-alkanes C_nH_{2n+2}. Studies demonstrates that compounds of this type with a carbon number in the range 16–50, corresponding to paraffins and polyethylene waxes, generates high rates of entrainment of liquid droplets into the gas stream.

Entrainment Model

Karabeyoglu and colleagues have developed a mathematical formulation of the entrainment phenomenon [27] [28]. The formulation is conceived to be an extension of the classical theory presented in Section 2.4.1.

The model consider the liquid layer thickness formed on a burning solid fuel surface under the combined action of convective and radiant heating. This thickness depends on the energy transfer balances both in the solid and in the liquid phases, as shown in Figure 2.11.

The film thickness is considered constant because the velocity of the liquid-gas interface and of the solid-liquid interface are assumed to be equal and constant, so a steady-state regression of the fuel is achieved.

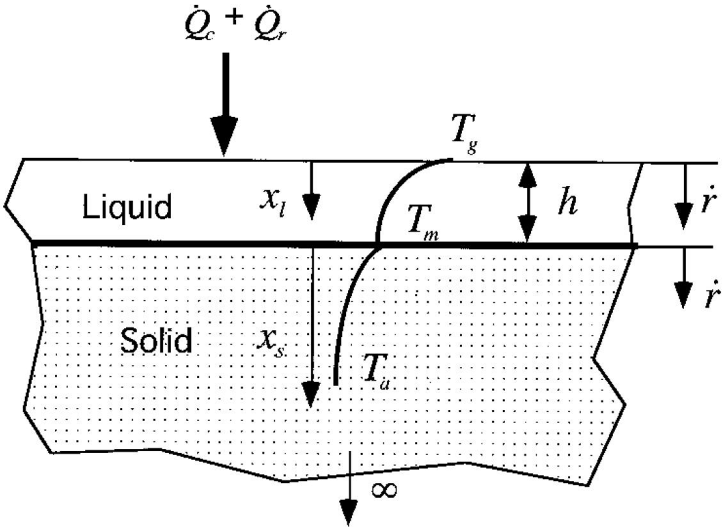

Figure 2.11: Schematic of the thermal model used in Karabeyoglu mathematical formulation of entrainment [27].

In the analysis the penetration of the thermal radiation into the solid is considered, both the liquid and the solid material are assumed to behave like gray bodies (absorption coefficient is independent on the frequency of the impinging radiation). Under these hypothesis the radiative energy fluxes in the liquid and solid phases are:

$$\dot{q}_{rad}\left(x_l\right) = \dot{Q}_{rad} e^{-\alpha_l x_l} \tag{2.28}$$

$$\dot{q}_{rad}\left(x_s\right) = \dot{q}_{rad}\left(h\right) e^{-\alpha_s x_s} = \dot{Q}_{rad} e^{-\alpha_l h} e^{-\alpha_s x_s} \tag{2.29}$$

$\dot{Q}_{rad}$ is the total collimated radiative flux impinging on the surface, while α_l and α_s are the absorption coefficient of liquid and solid phases respectively. The radiative heating of material at any position can be expressed as the divergence of the radiative flux $-\nabla \cdot \mathrm{q}_{rad}$, so the radiative heatings in the solid and in the liquid phases can be written according to the following equations:

$$-\frac{dq_{rad}}{dx_s} = \alpha_s \dot{Q}_{rad} e^{-\alpha_l h} e^{-\alpha_s x_s} \tag{2.30}$$

$$-\frac{dq_{rad}}{dx_l} = \alpha_l \dot{Q}_{rad} e^{-\alpha_l x_l} \tag{2.31}$$

It can be shown that the total heating of the fuel by radiation is equal to the radiative heat input:

$$\int_0^h \alpha_l \dot{Q}_{rad} e^{-\alpha_l x_l} \mathrm{d}x_l + \int_0^\infty \alpha_s \dot{Q}_{rad} e^{-\alpha_l h} e^{-\alpha_s x_s} \mathrm{d}x_s = \dot{Q}_{rad} \tag{2.32}$$

In order to write the energy balance equations in the liquid and in the solid phases, two characteristic thermal thicknesses have to be defined: the characteristic thermal thickness in the liquid phase δ_l and the characteristic thermal thickness for the solid phase, δ_s defined as:

$$\delta_l = \frac{\kappa_l \rho_l}{r_f \rho_s} \tag{2.33}$$

$$\delta_s = \frac{\kappa_s}{r_f} \tag{2.34}$$

In which κ_l, κ_s, ρ_l and ρ_s are the thermal diffusivities and densities of the liquid and solid. So energy balance equations in the liquid and in the solid phases result to be respectively:

$$\frac{\mathrm{d}^2 T}{\mathrm{d}x_l^2} + \frac{1}{\delta_l}\frac{\mathrm{d}T}{\mathrm{d}x_l} = -\frac{\alpha_l \dot{Q}_{rad}}{\kappa_l \rho_l c_{pl}} e^{-\alpha_l x_l} \tag{2.35}$$

$$\frac{\mathrm{d}^2 T}{\mathrm{d}x_s^2} + \frac{1}{\delta_s}\frac{\mathrm{d}T}{\mathrm{d}x_s} = -\frac{\alpha_s \dot{Q}_{rad}}{\kappa_s \rho_s c_{ps}} e^{-\alpha_s x_s} \tag{2.36}$$

in which c_{pl} and c_{ps} are the specific heats of the two phases respectively. The general solutions for these linear ordinary differential equations, $T(x_l)$ and $T(x_s)$, can be found with the boundary conditions discernible from Figure 2.11. For Equation 2.35, $T(0) = T_v$ and $T(h) = T_m$, while for Equation 2.36, $T(0) = T_m$ and $T(h) = T_\infty$. Thus the temperature profiles and their derivatives in the two phases can be evaluated.

The energy transfer from the liquid to the interface must be equal to the heat conducted into the solid from the interface and the energy required for the phase transformation. Thus the energy balance at the liquid-solid interface can be expressed as:

$$-k_l \left(\frac{dT}{dx_l}\right)_{x_l=h} + k_s \left(\frac{dT}{dx_s}\right)_{x_s=0} - h_m \rho_s r_f = 0 \tag{2.37}$$

where h_m is the latent heat of melting. An analogous energy balance can be written for the gas-liquid interface, where the convective heat transfer from the gas to the interface must be equal to the sum of conductive heat transfer into the liquid and the heat required for the phase transformation:

$$\dot{Q}_{conv} + \kappa_l \left(\frac{dT}{dx_l} \right)_{x_l=0} - h_v \rho_s r_v = 0 \tag{2.38}$$

in which h_v is the latent heat of vaporization and r_v the regression rate due to vaporization. In this formula (Equation 2.38) the possibility of entrainment mass transfer from the liquid surface is considered other than the mass transfer by vaporization. Combining Equations 2.38 and 2.37 results that the total energy transferred to the wall, $\dot{Q}_w$, must be equal to the total energy absorbed in the grain, which is composed of the energy required to heat the liquid and solid and the heat required for the phase transformations:

$$\dot{Q}_w = \dot{Q}_{rad} + \dot{Q}_{conv} = h_{m,v} \rho_s r_f + h_v \rho_s \tag{2.39}$$

$h_{m,v}$ results to be the sum of the heat of melting and the heat needed to reach vaporization temperature. So the enthalpy of vaporization presented in Equation 2.7 becomes, for liquefying propellants:

$$h_v = \frac{\dot{Q}_w}{\rho_s r_f} = c_{pl} \Delta T_{m,v} + c_{ps} \Delta T_{m,i} + h_m + h_v \frac{r_v}{r_f} \tag{2.40}$$

The form of Equation 2.40 is different than the typical expressions reported in the literature, because the heat required to vaporize the fuel transported by means of entrainment is zero.

Subsequently, inserting the known temperature derivatives into Equation 2.37 it is possible to write:

$$\Phi = \frac{h_m \left(R_l - 1 \right) + h_v \frac{\dot{Q}_{rad}}{\dot{Q}_w} \Phi^{R_l}}{h_{m,v} \left(R_l - 1 \right) + h_v \frac{\dot{Q}_{rad}}{\dot{Q}_w}} \tag{2.41}$$

where $\Phi = e^{\delta_{melted\,layer}/\delta_l}$ and $R_l = \alpha_l \delta_l$. The liquid layer thickness can be evaluated but an explicit solution for the algebraic nonlinear Equation 2.41 can not be achieved. So it is preferable to focus on the following two limit cases of interest:

- $R_l >> 1$. In this case the absorption of the radiation in the liquid layer is very high. The thickness of the liquid layer, $\delta_{melted\,layer}$, can be solved explicitly as:

$$\delta_{melted\,layer} = \delta_l \ln \left(1 + \frac{c_{pl} \Delta T_{m,v}}{h_m} \right) \tag{2.42}$$

- $R_l << 1$. In this second case the absorption of the radiation in the liquid phase is small, all the radiation is absorbed by the solid. The melted layer thickness results:

$$\delta_{melted\,layer} = \delta_l \ln\left(1 + \frac{c_{pl}\Delta T_{m,v}}{h_m - h_v \frac{\dot{Q}_{rad}}{\dot{Q}_w}}\right) \tag{2.43}$$

An important common property of the two thickness expressions of Equations 2.42 and 2.43 is that the melt layer thickness is proportional to the characteristic thermal length of the liquid, and thus inversely proportional to the regression rate: $\delta_{melted\,layer} \propto 1/r_f$.

Stability of the Liquid Layer

The liquid layer due to fuel melting can be unstable due to the effect of many parameters. Karabeyoglu has approached this problem developing some empirical relations for the entrainment with the use of some experimental data [27].

The main result of this approach is the fact that the entrainment mass transfer per unit area $\dot{m}_{ent}$ is proportional to the mass flow rate per unit width of the liquid $\dot{m}_l$ by this way:

$$\dot{m}_{ent} = 13.3e_0\left(X_e\right)\dot{m}_l \tag{2.44}$$

in the latter equation e_0 is an empirical dimensional proportionality function containing dynamic pressure of the gas P_d, surface tension σ, and a temperature ratio through the parameter X_e:

$$e_0 = 1 - e\left[-1.06 \cdot 10^{-4}\left(X_e - 2109\right)\right] \tag{2.45}$$

$$X_e = P_d^{0.5}/\sigma\left(\frac{T_g}{T_w}\right)^{0.25} \tag{2.46}$$

taking into account the experimental results and the results of the theory, Karabeyoglu and colleagues have suggested the following empirical expression for the entrainment rate of liquid droplets in terms of the most relevant properties of the hybrid motor:

$$\dot{m}_{ent} \propto \frac{P_d^a \delta_{melted\,layer}^b}{\mu_l^c \sigma^d} \tag{2.47}$$

where a, b, c, d experimental parameters. This latter expression (Equation 2.47) demonstrates that the entrainment phenomenon is mainly favored by low values of surface tension and viscosity.

Complete model

In the light of the mentioned elaborations, the classic hybrid theory requires three modifications in order to include entrainment phenomenon:

- The entrainment of melted fuel droplets modifies the ratio between the enthalpy difference between the flame zone and the surface of the grain and the enthalpy of vaporization($\Delta h/h_v$) that appears in the thermal blowing parameter (Equation 2.16). The effective heat of gasification is reduced because the evaporation energy required for the fuel mass transfer from the surface is partly avoided by the mechanical entrainment of the liquid, while the enthalpy difference between the flame and the surface is also reduced because some of the reactants are now in liquid phase.
- The blocking factor C_h/C_{h0} is also altered as a result of the presence of the two-phase flow. the blocking factor can be expressed as a function of evaporation blowing parameter B_v:

$$\frac{C_h}{C_{h0}} = f\left(B_v\right). \tag{2.48}$$

- The ripples formed on the liquid layer surface increase the surface roughness and the heat transfer from the flame front to the surface.

These show that the total regression rate of a hybrid motor can be expressed as the sum of two terms (Figure 2.12): the evaporation regression rate that is generated by the vaporization of the liquid into the gas stream, r_v, and the entrainment regression rate that is related to the mass transfer from the liquid surface caused by the interaction between the fuel melted layer and the oxidizer flow, r_{ent}:

$$r_f = r_v + r_{ent} \tag{2.49}$$

the additional entrainment term provides a notable enhancement in total regression rate, which can reach values from three to four times higher than that reached by conventional polymeric fuels (Figure 2.13).

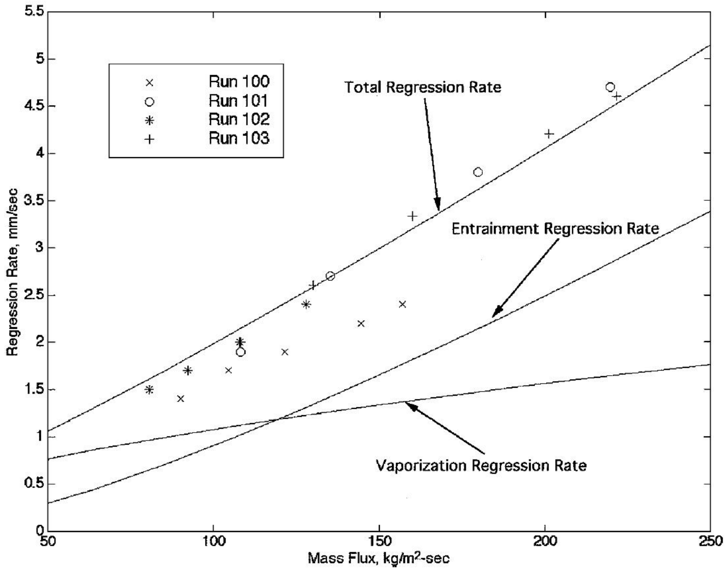

Figure 2.12: Pentane burning under GOX: experimental regression rate compared to the predictions provided by the entrainment theory, sum of vaporization and entrainment regression rate [27].

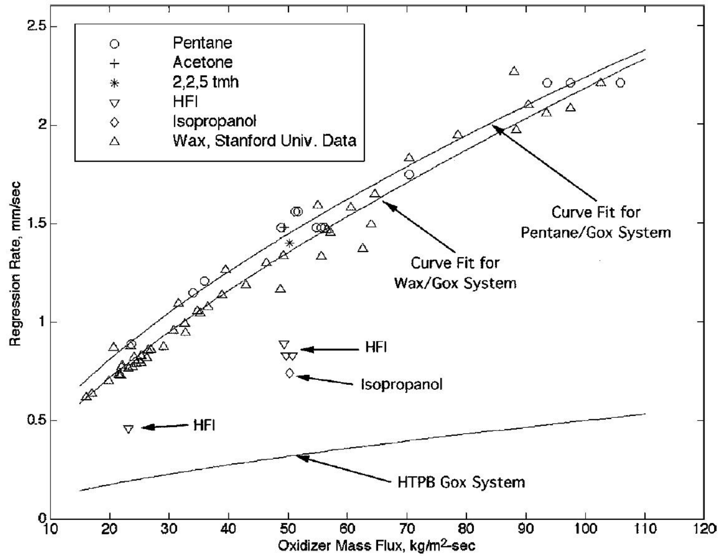

Figure 2.13: Regression rates versus oxidizer mass fluxes for various liquefying materials and HTPB burning under GOX. Thanks to entrainment effect higher regression rate are achieved by liquefying fuels [27].

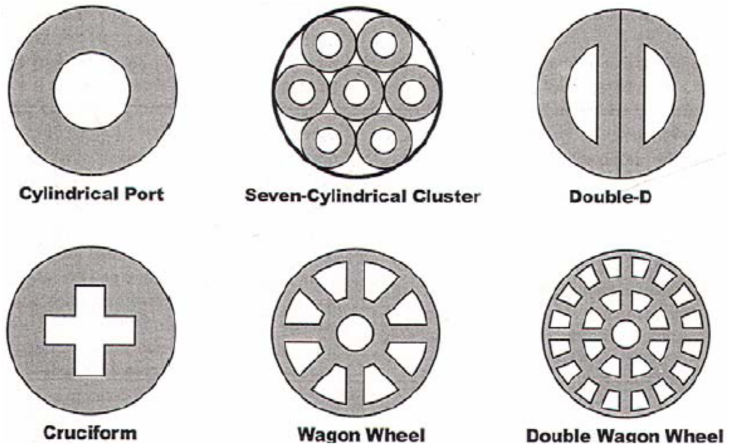

Figure 2.14: Different fuel port perforation configurations [3].

2.5 Thrust enhancements

Other than the use of liquefying propellants, different techniques has been considered in order to increase regression rate and thrust that are still under investigation. The main techniques are the use of special grain geometries, the use of fluid dynamic methods and the addition of additives.

2.5.1 Multi-perforated grains

One of the most used methods for increasing thrust is the use of a multi-port grain design, an example of possible multi-port grain configuration is reported in Figure 2.14. This technique enhances thrust through the increased fuel mass flow due to the augmented overall regression surface and has been used in the *SpaceShipOne* project.

The greatest problem with this grain layout is that the amount of fuel that can be loaded into a given volume is reduced leading to an increase in the system diameter for a given total fuel mass. Moreover the grain must be produced in segments and each segment must be supported by a dedicated structure adding weight and complexity.

Another drawback of this technique is the lower combustion efficiency and the anisotropy due to the difficulty to obtain an identical regression rate in each port. This anisotropy of the combustion leads to larger combustion residuals and compromised grain integrity.

Paraffin and other liquefying propellants have the advantage of not having the need of multi-perforated grains thanks to their intrinsic high regression rate [27].

2.5.2 Fluid dynamic methods

Other methods considered fluid-dynamic devices that can provide an higher level of turbulence in order to rise the local convective heat transfer coefficient. Webs of metallic wires can be put into the grain so that during combustion this elements promotes turbulence [1]. Another way is to generate vortexes thanks to a tangential injection of the oxidizer that realizes a swirl motion of the gas.

Also helicoidal grain perforations can increase turbulence, but present complications in the manufacture and an increase of combustion residuals.

2.5.3 Energetic additives

Like in solid rocket propulsion, the solid fuel grain, often HTPB-based, can be doped with metals (Al, B, Fe, Mg) or with the respective hydrides (in particular AlH_3, MgH_2, BeH_2) in order to increase the enthalpy produced during the combustion. Typical regression rate enhancement that this technique can provide are shown in Fugures 2.15 and 2.16. This technique can be subjected to problems like the development of a two phase flow during the expansion in the nozzle, ignition resistance and possible incomplete oxidation reactions due to the slowness of the heterogeneous reactions that take place between metal and gaseous oxidizer.

Another possibility is to add a solid oxidizing agent to the grain such as ammonium perchlorate (AP) in various percentages, nevertheless in this approach the advantage of the intrinsic safety of the hybrid systems can be lost because of the missed separation between fuel and oxidizer.

As is possible to see in Equation 2.5, the use of energetic additives directly influences the performances of hybrid systems, an enhancement in performances is achieved adding substances that:

- rise the flame temperature;
- lower the mean molecular weight.

The introduction of metals tends to increase the average molecular weight of combustion products, so, in order to reach a benefit, it is necessary that the ratio T_c/M grows up. From this approach comes the use of metal hydrides, that can lower the molecular weight with their relatively high hydrogen content and have additional energy release thanks to the hydrogen combustion.

All these reasons lead to the use of energetic additives also for the paraffin-based fuels tested in this work. Use of lithium aluminum hydride in a paraffin-based propellant has been studied in [34], in which paraffin wax was mixed with 7-24% $LiAlH_4$ by weight, leading to a notable enhancement in burning rate of a factor of ≈ 14. The same authors investigated also the use of higher $LiAlH_4$ contents (above 30%) in paraffin wax [35] in order to perform hypergolic ignition with nitric acid and other strong acids as oxidizers. In these studies $LiAlH_4$ was found to be a suitable potential additive for hypergolic ignition of samples.

Also aluminum hydride, AlH_3, promises to be a useful additive, it gives a combination of high energy from the metal oxidation and low molecular weight from the hydrogen content [7]. Its effects have been investigated at *SPLab* in HTPB-based fuels where AlH_3 has been identified as a very promising high-energy material for specific impulse increase [37].

Aluminum, the most used metal additive, has been used in a paraffin fuel for a practical application in a 3″ diameter rocket [36]. The rocket utilized paraffin-based fuel containing 40% of aluminum powder by mass, the authors noted an increase in flame temperature and regression rate. The presence of aluminum have also decreased the optimal oxidizer to fuel ratio, making possible to reduce the volume of the oxidizer tank.

Boron is another metal suitable for hybrid fuel doping, thanks to its high volumetric heat of oxidation, its use is problematic due to the fact that its ignition and boiling temperatures are extremely high, which can cause difficult ignition [38]. In order to make easier the ignition, coatings containing polymers and/or other reactive materials has been studied, like the magnesium coating reported in section 3.6.1.

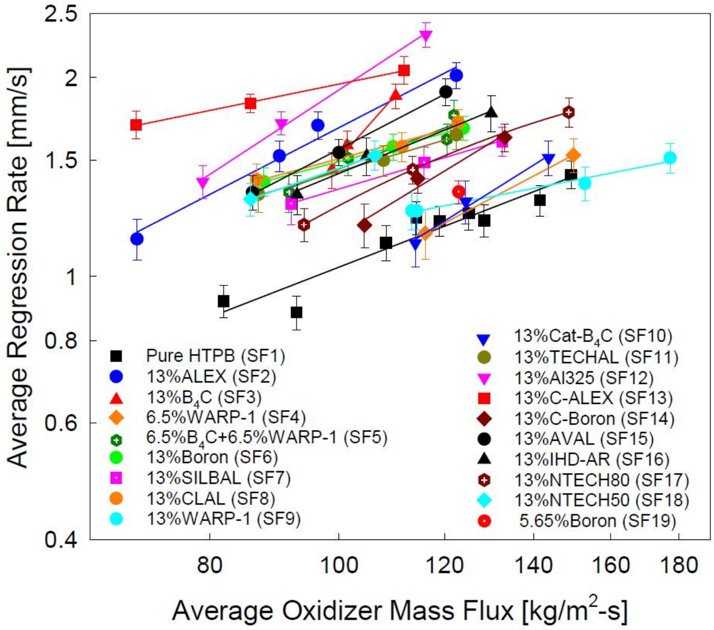

Figure 2.15: Comparison of regression rate evolution versus oxidizer mass flux for various HTPB-based solid fuel formulations [38].

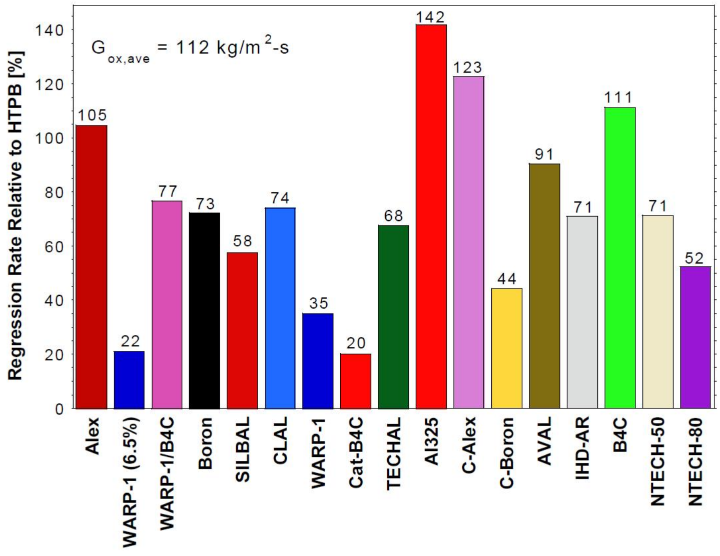

Figure 2.16: Percentage increase in regression rate of several doped HTPB-based solid fuel formulations compared to HTPB baseline [38].

CHAPTER

3

FUELS COMPOSITION AND PROPERTIES

In this chapter paraffin wax formulation (SW) is discussed in detail and characteristics of solid fuel ingredients are described.

3.1 Tested paraffin-based fuels

An *SPLab* reference paraffin wax formulation (SW) was defined in previous works [15] [22]. These early works led to a mixture of solid paraffin wax with small amounts of stearic acid and graphite, exact percentage by weight of each ingredient is shown in Table 3.1.

Table 3.1: SW reference fuel ingredients.

Ingredient	Nominal percentage [%]	Density $[kg/m^3]$
Paraffin Wax	88	890
Stearic Acid	10	845
Graphite	2	2250

This fuel has become the reference paraffin fuel for the laboratory. All the investigated fuels have been based upon this reference formulation, at which various metal based additives have been added. All the details about the composition of each formulation can be seen in Appendix B. Tested fuel formulations with their shorthand notation were:

- SW, paraffin wax with stearic acid and graphite;
- SW w/o SA, paraffin wax with graphite;
- SW w MgB, paraffin wax with stearic acid, graphite and magnesium-boron;
- SW w nFe, paraffin wax with stearic acid, graphite and nano-iron;
- SW w AlH_3 , paraffin wax with stearic acid, graphite and aluminum hydride;
- SW w MgH_2 , paraffin wax with stearic acid, graphite and magnesium hydride;
- SW w LAH, paraffin wax with graphite and lithium aluminum hydride;
- SW w 3LAH, paraffin wax with graphite and lithium aluminum exahydride;
- SW w μAl, paraffin wax with stearic acid, graphite and uncoated micron-sized aluminum;
- SW w μAl Flaked, paraffin wax with stearic acid, graphite and flaked micron-sized aluminum coated with paraffin;

3.2 Paraffin wax

The term paraffin wax (or simply *"paraffin"*) refers to a mixture of normal alkanes with the general formula C_nH_{2n+2} that falls within the range $20 \leq n \leq 40$ and are found in the solid state at room temperature [26]. The amount of normal alkanes in a paraffin wax usually exceeds 75% and may reach almost 100%. Paraffin wax is found as a white, odorless, tasteless, waxy solid, with a melting point between about 46 and 68 °C, and having a density of around 0.9 g/cm^3. It is insoluble in water, but soluble in ether, benzene, and certain esters. Paraffin is unaffected by most common chemical reagents but burns readily. Paraffin has been the main component of the fuels tested, it has performed three different tasks, to be the main burning material, to assure the mechanical properties of the grain during transportation and manipulation and to provide a solid matrix to contain additives.

Table 3.2: Properties of tested paraffin.

Physical state at T_{amb}	White solid
Molecular weight [g/mol]	394 [26]
Density at solid state [g/cm^3]	0.890
Melting point [K]	$331 \div 335$
Melting heat [kJ/kg]	254 [26]

3.3 Stearic acid

Stearic acid is a carbossilic acid of formula $CH_3(CH_2)_{16}CO_2H$, it is the saturated fatty acid with 18 carbon chain and has the IUPAC name of octadecanoic acid. Stearic acid is noteworthy as the most common saturated fatty acid. It is added to paraffin to improve the mechanical properties of the mixture.

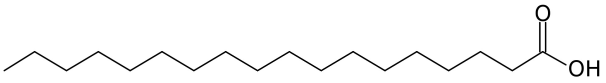

Figure 3.1: Chemical structure of stearic acid.

Table 3.3: Properties of tested stearic acid.

Physical state at T_{amb}	White solid in grains
Molecular weight [g/mol]	284.5
Density at solid state [g/cm^3]	0.845
Melting point [K]	340
Auto ignition temperature [K]	668

3.4 Graphite

Graphite is one of the allotropes of carbon, it is the most stable form of carbon under standard conditions. Graphite has a layered, planar structure

(Figure 3.2). In each layer, carbon atoms are arranged in a hexagonal lattice. It is added to paraffin in order to decrease the amount of radiant energy transmitted from the flame to the grain surface, lessening the decay of the mechanical properties of the grain.

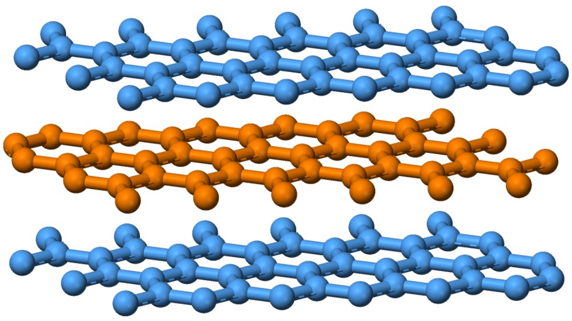

Figure 3.2: Graphite layers.

Table 3.4: Properties of tested graphite.

Physical state at T_{amb}	Black powder
Molecular weight [g/mol]	12.01
Density at solid state [g/cm^3]	2.250
Melting point [K]	3500

3.5 Hydrides

Hydrides are compounds containing metal or metalloid bonds to hydrogen. Hydrides are reducing agents and react rapidly and dangerously with oxygen and with other oxidizing agents, even weak ones. Hydrides are incompatible with acids, alcohols, amines, and aldehydes. The hydrogen storage in solid form as metal hydrides or complex metal hydrides is a promising alternative to hydrogen storage in high pressure cylinders and cryogenic tanks. In fact the use of hydrides is a safer, denser and more convenient method than pressurized gas or cryogenic systems [13]. During combustion hydrides release hydrogen that can undergo oxidation, also the metal is oxidized forming metal oxides, both these reactions are highly exothermic, contributing to raise the flame temperature with benefit for the propulsion system performances. Moreover hydrides can lower the combustion product molecular weight with their hydrogen content as mentioned in Section 2.5.3.

3.5.1 Aluminum hydride

Also known as *Alane*, AlH_3 is a colorless solid that is pyrophoric. *Alane* exists in more than one crystal structure of which α-Alane is the most thermally stable (Figure 3.3). Aluminum hydride has been discussed for storing hydrogen in hydrogen-fueled vehicles because of its high hydrogen content, up to 10% hydrogen by weight, corresponding to 148 g/L, twice the density of liquid H_2 [13]. Due to its attractive performance in increasing specific impulse [37], *Alane* is a potential additive to hybrid fuel. Aluminium hydride is not spontaneously flammable, but it is highly reactive. Aluminium hydride decomposes in air and water, violent reactions occur with both.

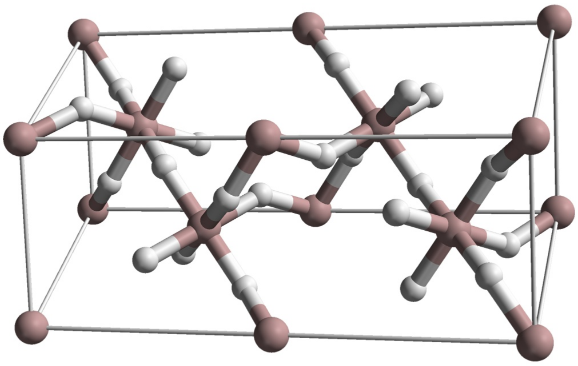

Figure 3.3: α-Alane unit cell.

Table 3.5: Properties of tested aluminum hydride.

Physical state at T_{amb}	Grey powder
Molecular weight [g/mol]	29.99
Density at solid state [g/cm^3]	1.486
Melting point [K]	423
Hydrogen content [%]	10.00
Formation heat [kJ/mol]	-11.4 [13]
Dehydrogenation temperature [K]	$433 \div 483$ [21]

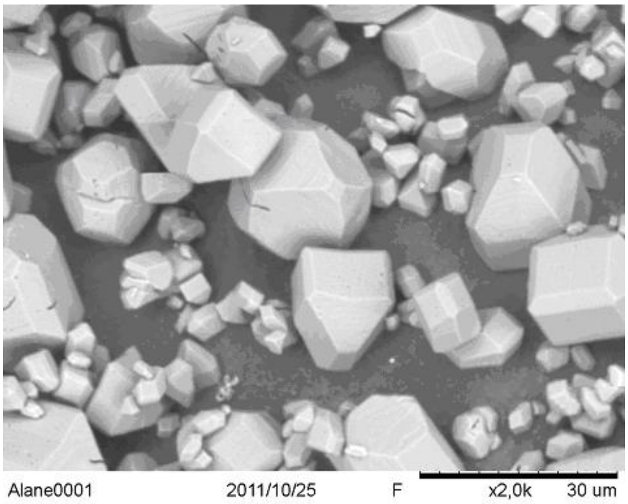

Figure 3.4: SEM of tested alane. Visibile crystals exhibits high regularity of shape, a characteristic of stable α-Alane. Crystals dimensions range from 5 μm to 50 μm [21].

3.5.2 Lithium aluminum hydride

Supplied by *Chemetall GmBH*, Lithium aluminum hydride is an inorganic compound with the chemical formula $LiAlH_4$ commonly abbreviated to *LAH*. It is a versatile reducing agent for organic chemical and pharmaceutical industry, it is dangerously reactive with water, releasing gaseous hydrogen (H_2). *LAH* undergoes thermal decomposition. When heated *LAH* decomposes in a three-step reaction mechanism:

$$3\,\mathrm{LiAlH_4} \longrightarrow \mathrm{Li_3AlH_6} + 2\,\mathrm{Al} + 3\,\mathrm{H_2}$$

$$2\,\mathrm{Li_3AlH_6} \longrightarrow 6\,\mathrm{LiH} + 2\,\mathrm{Al} + 3\,\mathrm{H_2}$$

$$2\,\mathrm{LiH} + 2\,\mathrm{Al} \longrightarrow 2\,\mathrm{LiAl} + \mathrm{H_2}$$

"LAH" is highly reactive and has a relatively high hydrogen content, nevertheless, it requires special attention due to its poor compatibility with HTPB-binder matrix. For this reason recently it has been considered as a possible candidate for paraffin-based fuels doping [21].

Table 3.6: Properties of tested lithium aluminum hydride.

Physical state at T_{amb}	Grey powder
Molecular weight [g/mol]	37.95
Density at solid state [g/cm^3]	0.92
Melting point [K]	423
Hydrogen content [%]	10.62
Formation heat [kJ/mol]	-113.4 [13]
Dehydrogenation temperature [K]	398 [41]

3.5.3 Lithium aluminum exahydride

As mentioned before, lithium aluminum exahydride, Li_3AlH_6, is one of the product of decomposition of lithium aluminum hydride. It is another promising candidate for an hydrogen storage material.

Table 3.7: Properties of tested lithium aluminum exahydride.

Physical state at T_{amb}	Grey powder
Molecular weight [g/mol]	53.80
Density at solid state [g/cm^3]	0.99
Hydrogen content [%]	11.15
Formation heat [kJ/mol]	-310.9 [13]
Dehydrogenation temperature [K]	$463 \div 483$ [21]

3.5.4 Magnesium hydride

Magnesium hydride is a white crystalline solid of formula MgH_2. It is highly flammable and pyrophoric, it ignites spontaneously in air forming magnesium oxide and water. It reacts with water to form caustic solution of magnesium hydroxide and hydrogen gas (H_2) and heat sufficient to ignite the evolved hydrogen.

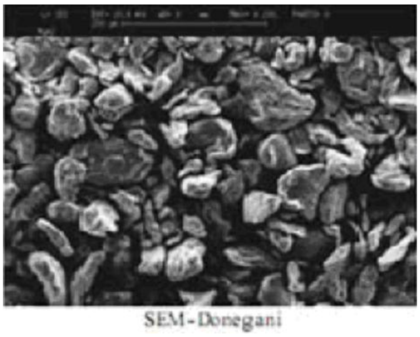

Figure 3.5: SEM image of tested magnesium hydride. Particles exhibit irregular shape [21].

Table 3.8: Properties of tested magnesium hydride.

Physical state at T_{amb}	Grey powder
Molecular weight [g/mol]	26.32
Density at solid state [g/cm^3]	1.45
Melting point [K]	600
Hydrogen content [%]	7.66
Formation heat [kJ/mol]	-74.5 [13]
Dehydrogenation temperature [K]	553 [7]

3.6 Metals

Light metals are excellent fuels due to their high developed enthalpy of combustion per unit mass, on the other hand their use can be problematic since the ignition of the metals could be difficult, their combustion can be incomplete and they lead to a two-phase flux due to the presence of condensed combustion products [4].

3.6.1 Magnesium-boron

Magnesium-boron, MgB is an energetic fuel developed by *MACH I*, King of Prussia, Pennsylvania, USA [42]. Boron could provide higher performances than aluminum as energetic additive since its volumetric heat of oxidation is higher than that of aluminum. Nevertheless boron hard ignition and poor combustion efficiency have hindered these possibilities. This fuel has been studied in order to lessening or eliminating the boron characteristic drawbacks [25]. In this study a magnesium-boron powder with a boron purity of 90-92% and with a 20% magnesium content has been used, due to this characteristics this powder has been named $MgB90(20\%Mg)$.

Table 3.9: Properties of tested magnesium-boron.

Physical state at T_{amb}	Grey powder
Density at solid state [g/cm^3]	2.19
BET surface area [m^2/g]	3.5 [25]

3.6.2 Nano-iron

Furnished by *Advanced Powder Technology LLC (APT)*, Tomsk, Russia [40], this nano-powder was prepared by electric explosion of a metallic wire in argon, then it was wet by hexane and packaged in glass bottles under inert atmosphere. Nano–sized iron powder is considered as a possible candidate for solid fuel loading due to iron high density that can yield to significant mass burning rate enhancement.

Table 3.10: Properties of tested nano-iron.

Physical state at T_{amb}	Dark gray to black suspension or paste
Molecular weight [g/mol]	55.85
Density at solid state [g/cm^3]	3.7 [40]
Melting point [K]	1811
Average particle size [nm]	$50 \div 110$ [40]
BET surface area [m^2/g]	7.7 [40]

3.6.3 Uncoated micron-sized aluminum

Aluminum is the most used metallic additive in chemical propulsion, due to its good performance and relative low cost. Aluminum can be introduced in a variety of granulometries typically at nano and micron-size. The main parameters that characterize aluminum powders are the specific surface, measured with *BET* technique, and the surface coating, that can be natural (aluminum oxide) or artificial [4].

Conventional micron-sized powders can produce mass burning rate enhancement due to the increase in fuel density: being less reactive than their nano-sized counterpart (lower specific surface, higher ignition temperature), their contribution to regression rate increase is mainly due to higher contribution of radiation from soot and CCPs from the flame zone toward the solid fuel grain [21]. An uncoated micron-sized aluminum powder has been tested in this work, named ASD-6 (Aluminum Spherical Dispersed) [31].

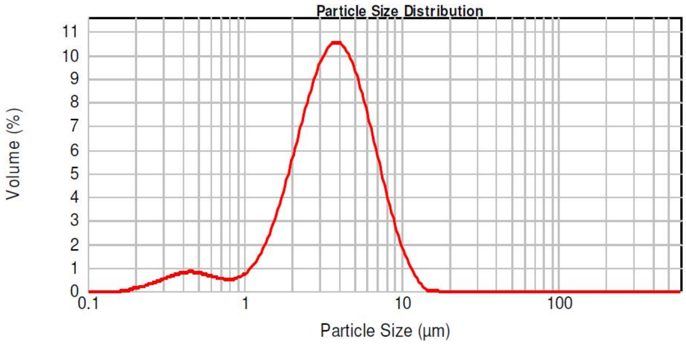

Figure 3.6: Particle size distribution of tested uncoated micron-aluminum, average of three performed tests [Reina, 2012].

Table 3.11: Properties of tested uncoated micron-aluminum.

Physical state at T_{amb}	Grey powder
Molecular weight [g/mol]	26.98
Density at solid state [g/cm^3]	2.27
Average particle size [μm]	3.987 [Reina, 2012]
BET surface area [m^2/g]	2.62 [Reina, 2012]

3.6.4 “Flaked” micron-aluminum coated with paraffin

This is the second type of aluminum powder tested, named PAP-2, also known as “Pigment aluminum powder” [30]. It is a micron-sized aluminum powder with a flaked particle shape shown in Figure 3.7.

It is widely used in light-reflecting, anti-corrosion, heat-resistant, decorative and other kinds of paints, enamels, varnishes and coatings. Aluminum particles in flaky powder have lamellar shape and are covered with thin oxide and fatty paraffin film.

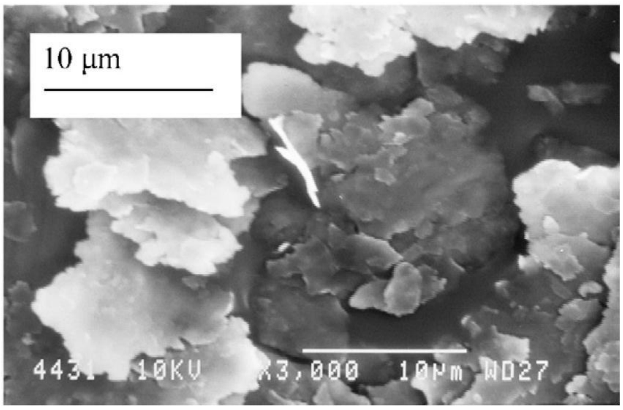

Figure 3.7: SEM image of tested "Flaked" micron-aluminum coated with paraffin. Particles exhibit flake shape [30].

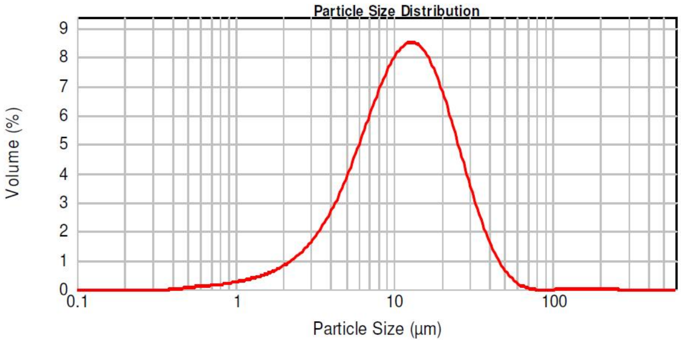

Figure 3.8: Particle size distribution of tested "Flaked" micron-aluminum coated with paraffin, average of four performed tests [Reina, 2012].

Table 3.12: Properties of tested "flaked" micron-aluminum coated with paraffin.

Physical state at T_{amb}	Silver-grey powder
Molecular weight [g/mol]	26.98
Density at solid state [g/cm^3]	2.27
Average particle size [μm]	14.066 [Reina, 2012]
BET surface area [m^2/g]	0.79 [Reina, 2012]

3.7 Oxidizer

The oxidizing agent used in all the burning tests was pure gaseous oxygen (100% O_2) fournished by Sapio s.r.l. in high pressure cylinders.

Table 3.13: Properties of oxygen.

Physical state at T_{amb}	colorless gas
Molecular weight [g/mol]	32.00
Density at T_{amb} e p_{amb} [kg/m^3]	1.43
Melting point [K]	54.36

3.8 Ignition temperature

In order to achieve a relative grading of investigated additives reactivity, ignition temperature was evaluated by means of a conductive–heating technique. Experimental setup for additives characterization and experimental procedure are described in detail in [23]. Ignition tests have been performed in a quiescent air atmosphere, with chamber pressure of 1 bar. Results achieved are reported in Table 3.14.

Table 3.14: Ignition temperatures of used additives, confidence interval of 95%, five tests performed for each additive [23].

Ingredient	T_{ign} [K]
AlH_3	614 ± 35
MgH_2	835 ± 40
$LiAlH_4$	398 ± 31
Li_3AlH_6	451 ± 9
MgB90 (20% Mg)	927 ± 57
nFe	NA
μAl	NA
μAl Flaked	NA

CHAPTER

4

PREPARATION OF FUELS

In this chapter the preparation procedure of tested fuels will be explained. All fuels used during the experimental campaigns were paraffin-based and differed only for the addition of energetic materials. For each formulation a set of 6-8 samples was prepared, a number superior to the strictly necessary in order to face the possible loss of some samples during the burning phase due to early mechanical collapse or departure of the sample from its placing.

The single sample was formed by a steel cylinder 30 mm long with internal diameter of 18 mm, the port was obtained with a cylindric central steel bone with 4 mm of diameter. The union of cylinder and bone formed the mould for the casting as shown in Figure 4.1 and 4.2.

4.1 Manufacture

The paraffin-based fuel with stearic acid and graphite is the standard paraffin wax formulation of the laboratory, used as a reference baseline for the subsequent paraffin-based additivated formulations. The preparation steps are presented in this section:

1. Desired quantities of paraffin, stearic acid and graphite are weighed with a precision balance;

2. the ingredients are introduced in a Pirex *beaker*;
3. the *beaker* is put on a hotplate set to reach a temperature above 60°C, the paraffin melting point;
4. the mixture take several minutes to melt, during the melting it is necessary to mix the ingredients with a steel spoon or a stick;
5. when the mixture results totally melted and assumes a homogeneous aspect, the hotplate can be set to a lower temperature, at around 60°C;
6. the mixture is poured in the moulds rapidly and constantly, preferably with a single move. With these tricks paraffin can solidify in a few minutes avoiding the formation of bubbles imprisoned in the grain, and avoiding also the precipitation of graphite or additives;
7. the samples take few minutes to cooling;
8. after cooling and solidification completed the bones are extracted;
9. the adherence of the paraffin-based grain to the inside wall of the steel cylinders is low, so, in order to increase it, a small amount of a Cyanoacrylic glue is applied along the perimeter of both the top and the bottom ends of each sample. After these operations the samples are ready for the burning tests.

Preparation of the additivated paraffin-based fuels was identical with the exception for hydrides, due to their tendency to dehydrogenate and decompose above a certain temperature, it was necessary to remain below this limit, checking the mixture temperature with a thermometer.

4.2 Density measurements

During the fuel preparation a small quantity of product was retained with the aim of make a density measurement, this result, if compared with the theoretical fuel density calculated knowing density and mass of the single components, has led to an indication of the quality of the preparation process.

Measured fuel density was derived as the ratio between mass and volume of the density sample, the mass was measured with the precision balance, the volume was obtained from Archimedes' principle: the same sample was suspended under the balance and immersed in a container with alcohol of known density, 0.8097 g/cm^3, in this condition the balance

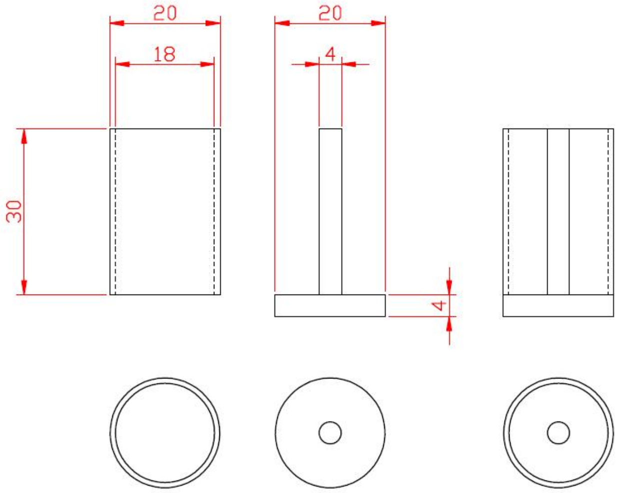

Figure 4.1: From left to right: the steel cylinder, the central bone, the complete mould.

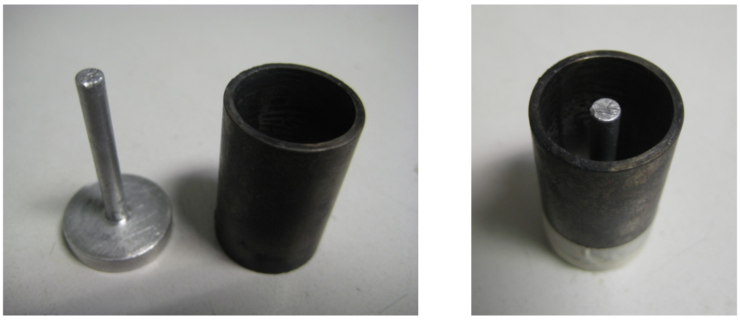

Figure 4.2: Central bone and cylinder (left), mould ready for the casting (right).

could measure the buoyancy caused by the alcohol. So using the following proportion:

$$\frac{\rho_{fuel}}{\rho_{alcohol}} = \frac{Fuel\,sample\,weight}{Buoyancy} \tag{4.1}$$

The final fuel density can be calculated as:

$$\rho_{fuel} = \frac{Fuel\,sample\,weight}{Buoyancy}\,\rho_{alcohol} \tag{4.2}$$

The collected densities of each fuel, both measured and theoretical, are shown in Table 4.1, where also the value of the fuel porosity is reported, defined as difference between measured and theoretical density evaluated as percentage with respect to the theoretical. The porosity, a maximum of 3.1%, can be considered acceptable. Note that for the *Alane* and nFe additivated formulation the density test has not been performed, due to shortage of the material.

Table 4.1: Produced fuels density.

Fuel	Theoretical density [kg/m^3]	Measured density [kg/m^3]	Difference [%]
SW	896	921	+2.7
SW w/o SA	901	909	+1.0
SW w MgB	912	931	+2.0
SW w nFe	938	NA	NA
SW w AlH_3	939	NA	NA
SW w MgH_2	932	950	+2.0
SW w LAH	903	875	-3.1
SW w 3LAH	906	887	-2.1
SW w μAl	955	986	+3.1
SW w μAl Flaked	955	980	+2.6

CHAPTER

5

EXPERIMENTAL SETUP

A 2D-radial micro-burner has been developed during the years at the space propulsion laboratory, SPLab of Politecnico di Milano. The aim was to characterize hybrid fuels ballistics, in this chapter the experimental setup is presented as well as the test procedure.

5.1 General layout

Experimental Setup has been designed and developed starting with the work of Eng. Maggiolini and Eng. Monferini [16], later the line has been modified by Eng. Frangi [17], Eng. Bosisio [18] and Eng. Raina [19], in order to reach the current configuration [15]. The experimental line is constituted by different items:

- test chamber;
- injection system;
- pneumatic line;
- electrical circuit;
- laser ignition system;

- video capturing system.

This setup allows the operator to carry out the burning of the samples with safety and reliability, setting all the parameters of the burning test: chamber pressure, type of fuel, oxidizer composition and flow. The line is shown in Figure 5.2, while in Figure 5.1 it can be possible to see a schematic representation.

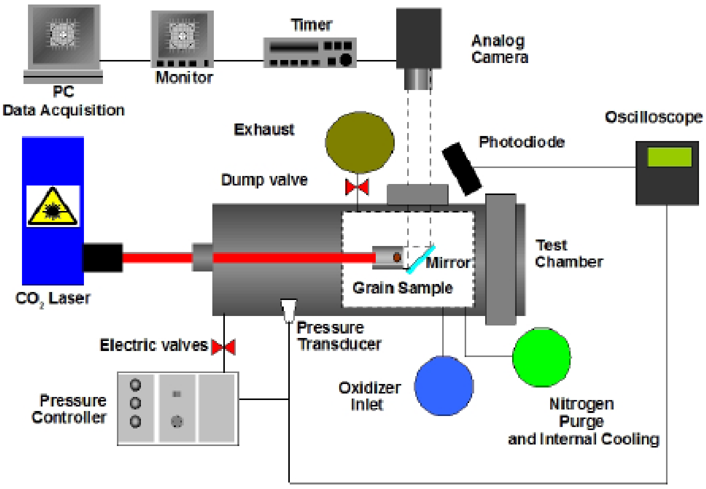

Figure 5.1: Experimental Setup, schema [15].

5.1.1 Test chamber

Test chamber is formed by two stainless steel (*AISI 316*) cylinders, one shorter and fixed, and one longer and movable (Figure 5.3). These two parts are connected by a threaded flange that allow to lock the cylinders in order to ensure the seal of the chamber. The oxidizer pipeline, a pressure transducer and the nitrogen inlet are connected to the fixed cylinder, while the movable one presents two exhaust pipelines for the exhaust gases.

The latter cylinder has three optical access, including two lateral rectangular quartz windows, 12 mm thick, that allow to place a camera to observe the test. The third window is a circular one, a Zinc Selenide lens ($ZnSe$) 6 mm thick, placed to the end of a brass cylinder named *"telescope"*. Through this lens the laser beam used for ignition can enter the chamber reaching the pyrotechnic charge.

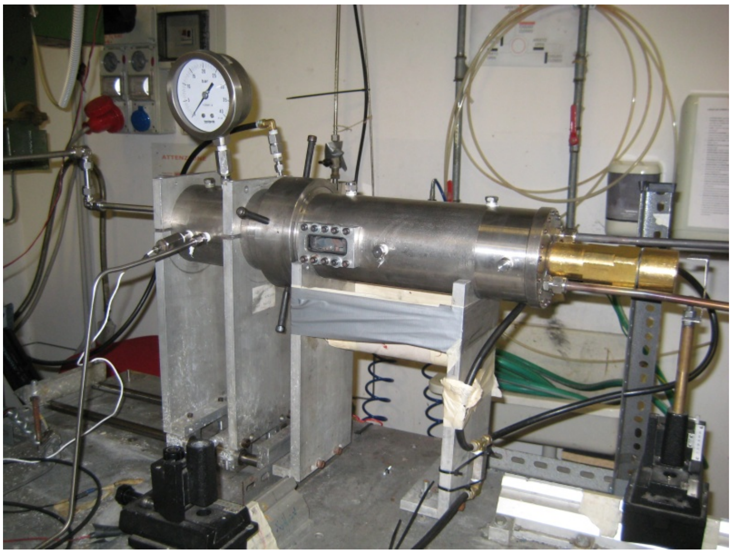

Figure 5.2: Experimental Setup, general view.

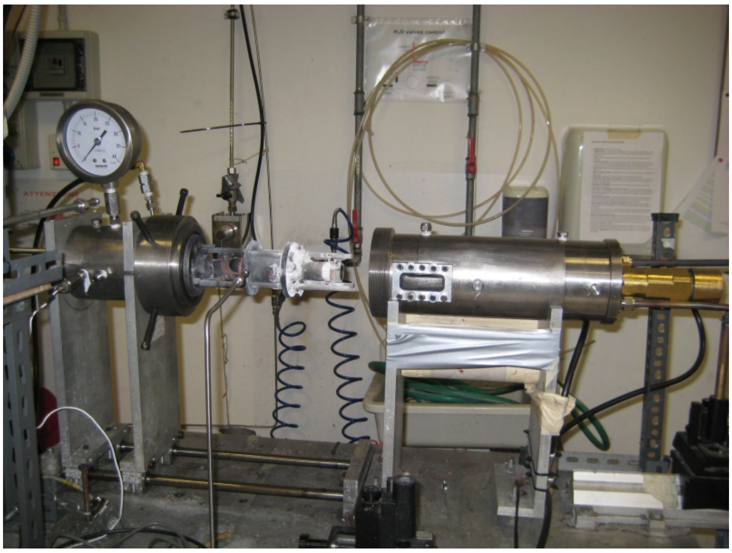

Figure 5.3: The test chamber opened: movable cylinder (left), with injector and inlets, fixed cylinder (right), with "telescope" and exhausts.

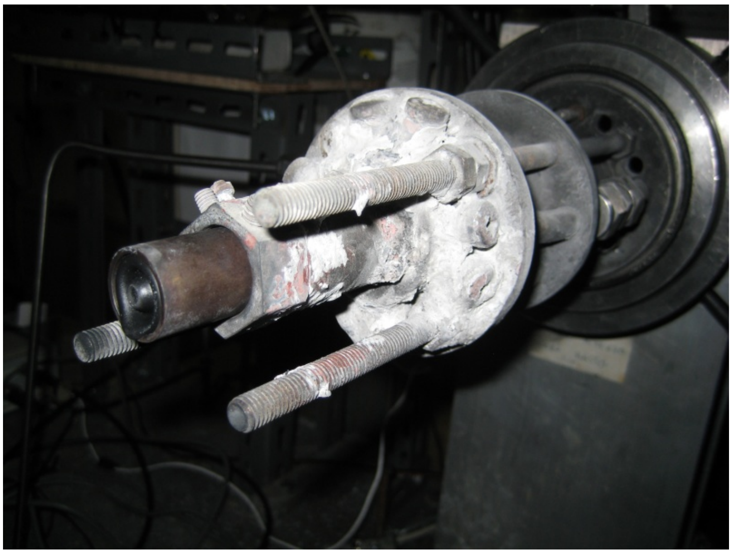

Figure 5.4: The injector with the adjustable pinholes and a sample in its housing.

5.1.2 Injection system

The injection system allow to satisfy three needs: to supply the required oxidizer flow, to provide internal cooling to the chamber and the injector itself, to maintain the optical path cleared of the fumes produced by combustion. These tasks are performed by two feeding lines, the oxidizer one (primary line) and the nitrogen one (secondary line).

Primary line is fed by an oxygen high pressure cylinder that assures the desired oxygen flow, this flow flows before in a pre-mixing chamber, then in a pre-combustion one after passing in the actual injector. This element is constituted by a circle of adjustable pinholes that can provide a *swirl* motion to the fluid (Figure 5.4), with this device the flame results stabilized and the combustion more homogeneous. Finally, after the injector, the flow pass through the sample central port perforation sustaining the combustion.

Secondary line is fed by two parallel connected nitrogen high pressure cylinders, this nitrogen flow wash the internal chamber walls and the sample cylinder external surface during the burning, in order to cool and to sweep away the exhaust fumes.

5.1.3 Laser ignition system

The ignition of the sample has been initially provided by the use of a pyrotechnic charge placed in the end of the central port on the side of the injector, the charge was an HTPB-based aluminized solid propellant.

After some early tests, too large initial port diameters has been noted, this fact was due to the low mechanical properties of paraffin-based fuels that during the ignition shock were inclined to yield. In order to have smaller and less brutal port openings a new type of pyrotechnic charge was introduced. The new charge was formed by a thinner ordinary pyrotechnic charge, 2 mm thick, and a layer of kerosene gel produced in the laboratory, this final layout is shown in Figure 5.5.

The energy needed for the ignition of the charge was provided by a collimated laser beam generated by a CO_2 laser shown in Figure 5.6. Thanks to the laser the charge realized the grain ignition, allowing, at the same time, the oxygen flow going through the central channel. This ignition system offered great simplicity, reliability and low intrusiveness.

5.1.4 Pneumatic line

The pneumatic line is constituted by all the elements that allow to introduce and to expel the gases, regulating their pressure and flux:

- feeding lines, primary (oxygen) and secondary (nitrogen);
- compressed air line;
- pressure control system (composed by pressure transducer, pressure controller, electrovalves);
- exhaust pipelines.

The two feeding lines are adjustable both in pressure and in flow. Pressure is regulated with a pressure regulator on each tank, on the other hand the flow is adjusted by pin valves. Besides these main pneumatic lines a compressed air one is used with the aim of cooling the chamber after each combustion test and for the sealing check of the plant before the test.

The oxidizer flow is measured with a digital flow meter (Figure 5.7) controlled by a connected pc. Flow meter technical data are reported in Table 5.1.

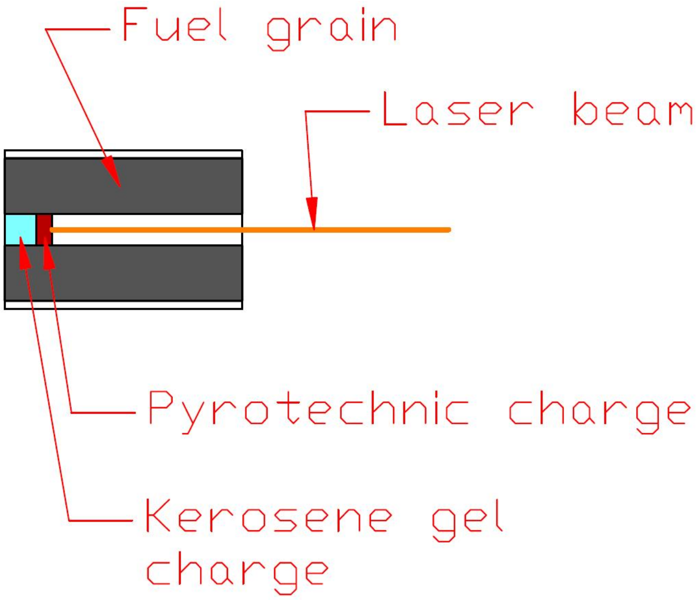

Figure 5.5: Sample with pyrotechnic charge.

Figure 5.6: Laser control panel.

Figure 5.7: Oxidizer flow meter.

Table 5.1: Flow meter technical data

Pressure rating [bar]	400
Flow range [Nlpm]	$0 \div 250$
Accuracy [% of FS]	± 1

Pressure chamber is maintained by a pressure controller that compares the pressure transducer signal (Table 5.2) with a set point value set manually. When the measured chamber pressure exceeds the set point pressure, the pressure controller readily opens the electrovalves allowing the draining of the exceeding flow, leading to a drop in pressure.

The pressure transducer signal is also sent to an oscilloscope connected to a personal computer that allow to visualize and save the pressure signal.

Table 5.2: Pressure transducer technical data.

Model	Kulite XTL-190 (M)
Type	differential piezoresistive
Pressure full scale [bar]	70
Maximum pressure [bar]	210
Sensitivity [mV/bar SG]	1.456
Zero pressure output [%fs]	±5
Maximum output [mV]	100
Temperature range [°C]	-55 – +175
Supply [VCC]	10-12
Input Impedance [Ω]	1000
Output Impedance [Ω]	1000

The plant has two exhaust pipelines that collects the exhaust gases, after passing in a water tank for cooling, these pipelines are intercepted by a set of five electrovalves. These valves are commanded by the pressure controller and act as actuators of the pressure control system. The number of these valves has been chosen after considerations about the flow and the reliability of the plant.

Table 5.3: Electrovalves technical data.

Model	79K9DGM
Maximum pressure drop [bar]	35
Central orifice diameter [in]	5/32
Connection type	1/4 NPT
Supply [VCC]	24
Absorbed power [W]	16
Material	Stainless steel AISI 316

The pneumatic system is also equipped with a safety valve, installed on the test chamber, in order to prevent damages due to too high values of pressure in case of any malfunction of the line.

5.1.5 Electrical circuit

An electrical circuit provides power supply to the plant, it supplies the electrovalves, the pressure controller, the laser, the fume hood, the camera, the oscilloscope and the personal computers.

5.1.6 Video capturing system

In order to estimate the grain regression rate, an optical technique is used. This technique allow a non-intrusive type of measurement, it consists in a video recording of the combustion tests and in a later analysis of the captured videos.

Two camera types are available in the laboratory, a *Xybion* analogic camera and a *Photron* digital camera (Table 5.4).

Table 5.4: Cameras technical data.

Camera	Xybion	Photron
Type	Analogic	Digital
Frames per second [fps]	25	$50 \div 10000$
Shutter setting [1/s]	Manual	$1/50 \div 1/10000$

The camera is placed at the side of the combustion chamber, aimed at one of the lateral windows. The sample image reach the camera thanks to a 45° angled mirror positioned behind the pre-mixing chamber. The camera is also connected to a personal computer where the combustion test can be seen live and where the video can be acquired and saved.

5.2 Combustion test procedure

The single test is articulated in a series of steps that allow the preparation and the optimization of the plant. These steps can be summarized as:

- regulation and calibration of the video capturing system;
- fuel sample preparation;
- laser alignment;
- test chamber preparation and sample combustion;
- cleaning and maintenance of the plant.

5.2.1 Regulation of the video capturing system

The first step is the centering of the camera on the chamber window to allow the correct and complete framing of the entire sample head end. Then, a short calibration video is filmed with the aim of obtaining a calibration video that allow to fix an equivalence between video pixels and actual sample diameter in millimeters, as reported in Section 6.2.1.

This video is realized using an empty steel cylinder with the same dimensions than the fuel sample's one, this cylinder is equipped with a small piece of graph paper placed on one end of the cylinder itself. This calibration cylinder is placed in the sample housing and a short video is filmed and saved after having regulated shutter and focus settings.

Other adjustments are necessary with the fuel sample placed in the housing, the shutter and focus settings are adjusted so as to have a clear and focused image.

5.2.2 Fuel sample preparation

As mentioned in Section 5.1.3, a pyrotechnic charge is inserted in the central port perforation of the fuel sample (Figure 5.8), so the sample can be placed in its housing in front of the injector with the charge side on the side of the injector. Finally the sample is fastened with two screws and the test chamber is closed.

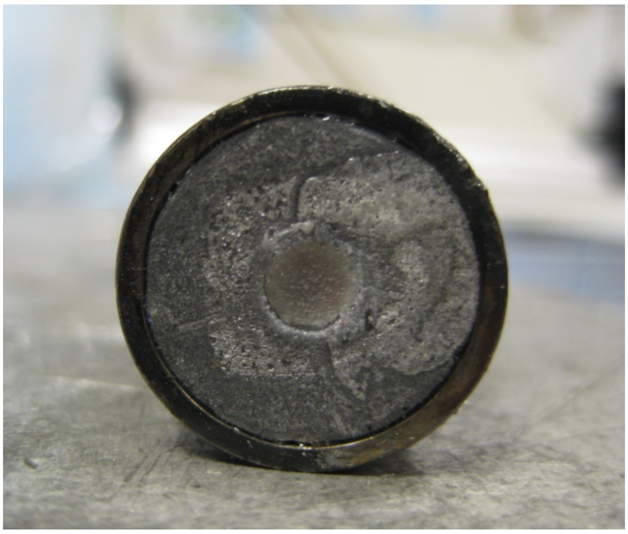

Figure 5.8: Paraffin-based magnesium hydride doped sample with pyrotechnic charge inserted.

5.2.3 Laser alignment

The laser beam must be perfectly aligned in order to enter in the chamber from the zinc selenide lens and reach the charge in the sample. Thus a series of alignment tests are performed switching on the laser and hitting with the laser beam a small piece of thermal paper placed on the Zinc selenide lens and on the sample end (without the pyrotechnic charge). In this way it is possible to see the actual path of the laser beam and adjustments can be performed using the external mirrors that aim the beam into the chamber.

5.2.4 Test chamber preparation and sample combustion

With the chamber closed all the inlet and exhaust ducts must be connected, then the exhaust valve is closed. The sealing of the plant is checked with the low pressure compressed air.

Then the nitrogen is opened and the chamber pressure starts to rise until the pressure set point value is not reached, at this point the electrovalves begin their work. With the personal computer the flowmeter is commanded and the oxidizer flow is opened.

With pressure and oxidizer flow conditions stabilized, the video and pressure signal capture are started. Now all the adjustments are done and the combustion can be started switching on the laser. In a few instants the laser beam ignites the charge and so the fuel sample, immediately the laser can be switched off and the combustion continues self sustained.

After the complete burning of the sample the oxygen flow is closed, so the combustion ceases. The exhaust valve must be opened in order to drop the pressure of the plant and to expel the hot exhaust gases. Then the nitrogen is closed and the compressed air opened for washing.

5.2.5 Cleaning and maintenance of the plant

The compressed air allows the cooling and the cleaning of the chamber, after a period of 10-15 minutes the chamber is enough cold to be opened and the empty sample cylinder to be removed.

The brass cylinder is removed and cleaned and the gaskets between this and the chamber are checked and changed, if necessary. Also the zinc selenide lens needs cleaning, so the laser beam has no difficulties entering the chamber in the next test. After these routine maintenance operations a new test can be performed.

More rarely, after 5 or 6 tests, the chamber needs a deeper cleaning to remove the paraffin residuals that accumulates on the bottom of the chamber. Another intervention is needed after a greater number of tests, the cleaning of the electrovalves from residuals that tend to obstruct the valves.

CHAPTER

6

COMBUSTION TEST ANALYSIS

In this chapter the single test analysis is explained, in particular all the measurements and calculation steps intended to obtain final time-resolved diameter and fuel regression rate are presented.

6.1 Preliminary evaluations

After the data acquisition termination, some preliminary evaluations about the quality of the recorded video and pressure trace can be made. The saved video is closely observed to verify its quality in terms of clearness and focus adjusting, fuel combustion is initially evaluated in terms of regularity, uniformity, duration and completeness.

A video editing could be required to have a better image quality and clarity. The software *VirtualDub*® is used to modify video contrast, brightness, sharpness and to rotate the recorded video.

The pressure signal is observed with the aim of checking the right pressure progress during the test. A typical pressure signal is reported in Figure 6.1, strand ignition is visible at trace start as a low pressure peak. After that, pressure trace presents a quasi-steady behavior during the combustion, note that oxidizer mass flow rate remains constant.

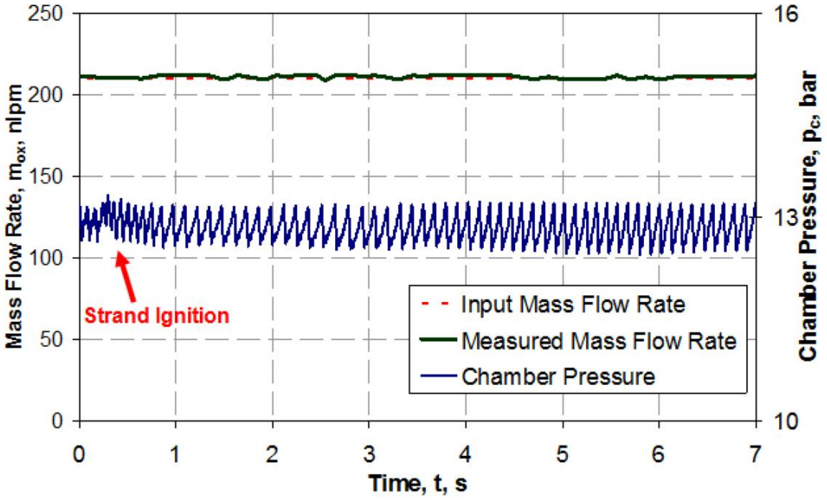

Figure 6.1: Typical combustion test pressure trace: quasi–steady value of chamber pressure is achieved.

6.2 Time-resolved regression rate

Regression rate of tested samples is evaluated from recorded video. In particular, central port diameter evaluation in time is defined starting from an optical analysis of the recorded video. In order to perform this measurement a calibration video is recorded at the beginning of each experimental session.

6.2.1 Calibration

Calibration recorded video enables to define an equivalence ratio between measured distance in pixels and real distance in millimeters. Calibration video is opened using the *Redlake Imaging MotionScope Camera*® software (Figure 6.2). The software allows to display the video frame by frame and to measure video pixel distances. The pixel coordinates of some points placed on a known distance (normally 10 mm) on the graph paper are collected, so the mean distance in pixels between these points is calculated and by this way an equivalence ratio pixels-real distance can be found.

6.2.2 Port diameter measurement

After the calibration the combustion test video is opened and the measurement process can begin. The first step is the determination of the first

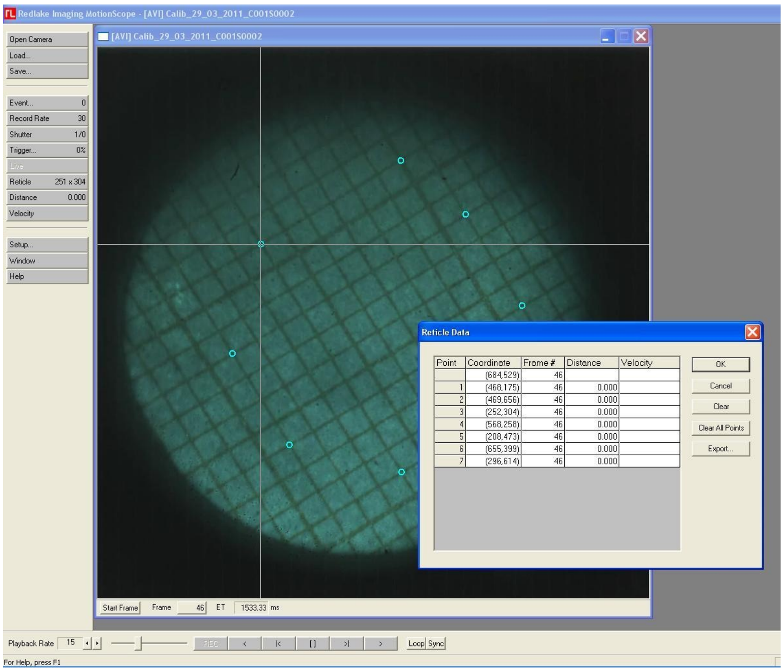

Redlake Imaging MotionScope - [AVI] Calib_29_03_2011_C001S0002

[AVI] Calib_29_03_2011_C001S0002

Event... 0
Record Rate 30
Shutter 1/0
Trigger... 0%
Reticle 251 x 304
Distance 0.000
Velocity

Reticle Data

Point	Coordinate	Frame #	Distance	Velocity
	(684,529)	46		
1	(468,175)	46	0.000	
2	(469,656)	46	0.000	
3	(252,304)	46	0.000	
4	(568,258)	46	0.000	
5	(208,473)	46	0.000	
6	(655,399)	46	0.000	
7	(296,614)	46	0.000	

Frame 46 ET 1533.33 ms

Playback Rate 15

For Help, press F1

Figure 6.2: Collecting the calibration points on calibration recorded video.

flame frame and the ignition frame. The first flame frame is the video frame at witch the flame of the pyrotechnic primer charge reaches the foreground of the image (head-end side of the sample) as shown in Figure 6.3. Instead ignition frame is the frame at which the charge results as completely burnt and the complete central port perforation appears for the first time (Figure 6.4).

This last frame can be considered as the first measurement frame, it marks the start of the actual fuel sample combustion, thus, starting at this point, the diameter measurements can be executed. Two measured times corresponds to this two frames: t_{ff} and t_{ign} respectively.

The diameter measurement is done manually, for each measurement frame central port diameter is sampled along different radial directions. Each diameter is measured selecting two points (one in front of the other) and annotating the pixel coordinates of these points. Due to the possible anisotropy of the combustion, the port perforation don't maintain a perfect circular perimeter, so, to take into account this behavior, the diameter measure is repeated in a ± 5 pixels high band, collecting a total of six pairs of pixel coordinates for each diameter.

The procedure is replicated in total for four radial directions. After these measurements it is possible to advance to the next measurement frame, normally a sampling frequency of 5 mean diameters per second

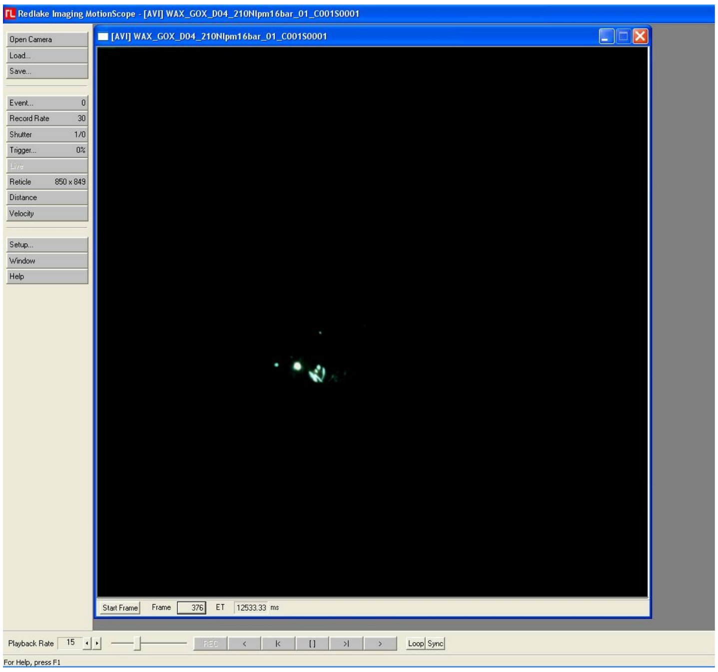

Redlake Imaging MotionScope - [AVI] WAX_GOX_D04_210Nlpm16bar_01_C001S0001

[AVI] WAX_GOX_D04_210Nlpm16bar_01_C001S0001

Event... 0
Record Rate 30
Shutter 1/0
Trigger... 0%
Reticle 850 x 849

Frame 376
ET 12533.33 ms

Playback Rate 15

For Help, press F1

Figure 6.3: Identification of first flame frame.

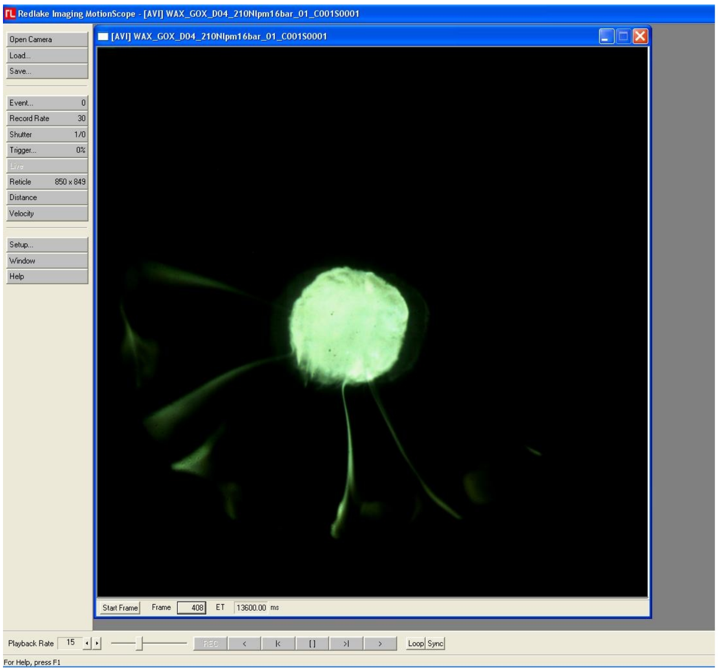

Redlake Imaging MotionScope - [AVI] WAX_GOX_D04_210Nlpm16bar_01_C001S0001

[AVI] WAX_GOX_D04_210Nlpm16bar_01_C001S0001

Event... 0
Record Rate 30
Shutter 1/0
Trigger... 0%
Reticle 850 x 849

Frame 408
ET 13600.00 ms

Playback Rate 15

For Help, press F1

Figure 6.4: Identification of ignition frame.

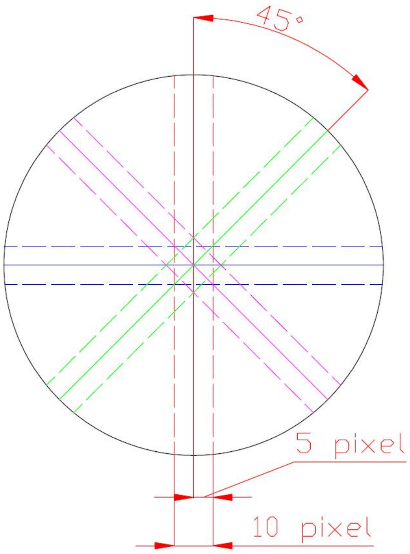

Figure 6.5: Central port perforation diameter measurement: diameters sampled along different radial directions (different color) and 5 pixels wide band.

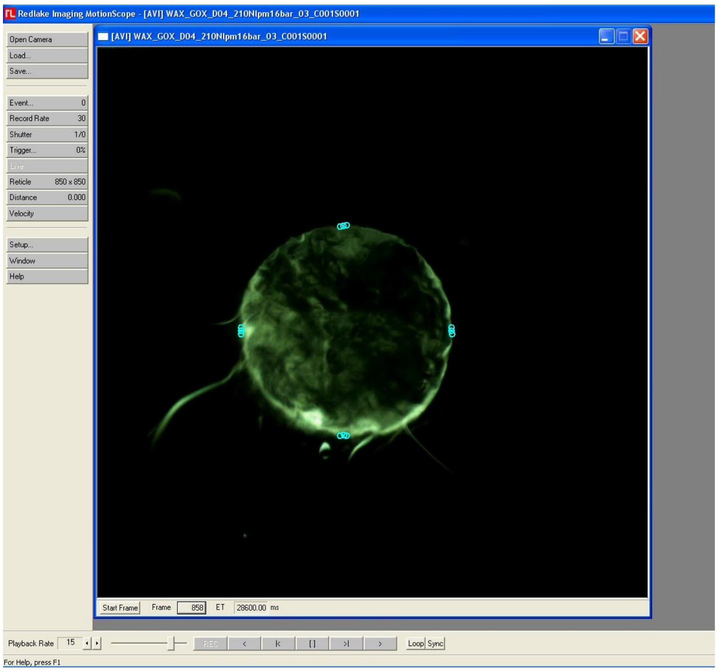
Redlake Imaging MotionScope - [AVI] WAX_GOX_D04_210Nlpm16bar_03_C001S0001

[AVI] WAX_GOX_D04_210Nlpm16bar_03_C001S0001

Event... 0
Record Rate 30
Shutter 1/0
Trigger... 0%
Reticle 850 x 850
Distance 0.000

Frame 858
ET 28600.00 ms

Playback Rate 15

For Help, press F1

Figure 6.6: Central port perforation diameter measurement: collected points.

(one diameter every 0.02 s) is considered enough in order to have a good representation of the combustion evolution in time. Eventually a total of 24 points equivalent to 12 diameters per frame is collected (Figure 6.5), leading to a single mean diameter per frame.

6.3 Regression rate calculation

With the measured diameters, an averaged diameter per frame, $\overline{D}_i$ (Equation 6.1), can be calculated as mathematical mean between the four mean diameters collected: the horizontal, D_{h_i}, the vertical, D_{v_i}, the horizontal of the 45° rotated video, D_{h45_i}, and the vertical of the 45° rotated video, D_{v45_i}.

$$\overline{D}_i = \frac{D_{h_i} + D_{v_i} + D_{h45_i} + D_{v45_i}}{4} \tag{6.1}$$

Starting from this sampled space-averaged diameter in time two different types of calculation can be performed to obtain the fuel regression rate: a *Thickness Over Time* (TOT) method and a *Analytical* method.

6.3.1 Thickness Over Time method

With this method the mean regression rate for the time interval $t_{i+1} - t_i$, $\overline{r}_{f_{i+\frac{1}{2}}}$, is calculated as the ratio between the diameter increment and the time increment, thus realizing a finite differences calculation:

$$\overline{r}_{f_{i+\frac{1}{2}}} = \frac{1}{2}\frac{\overline{D}_{i+1} - \overline{D}_i}{t_{i+1} - t_i} \tag{6.2}$$

despite the fact that this method is simple and commonly used in literature, it has some limitations. It suffers from intrinsic high errors and it only gives the regression rate trend in the form of a discrete function of time. In fact only *n-1* regression rate values can be calculated starting from the *n* mean diameters collected. The calculation of the other instantaneous parameters of interest (oxidizer mass flux, fuel mass flow rate, oxidizer to fuel ratio) can be performed from this TOT regression rate, but the results presents oscillations and peaks due to the nature of the method.

6.3.2 Analytical method

A better data reduction method has been developed and validated in *SPLab* [20], named *Analytical*. This method leads to a time-resolved regression rate in the form of a continuous function of time. It is based on a preliminary interpolation of the sampled space-averaged diameters in time. More precisely the diameter change in time with respect to initial nominal diameter value D_0 (4 mm) is fitted in time as a power function:

$$\overline{D}(t) - D_0 = a_D \, (t - t_0)^{n_D} \qquad t \geq t_{ign} > t_0 \tag{6.3}$$

this power law fitting has been chosen based on work done by Houser and Peck [24], and it shows a good agreement with the experimental data. To avoid the hassle of the ignition transient, the function describing the diameter evolution in time (Equation 6.3) is valid only starting from a t_{ign} ad-hoc defined, calculated as the one maximizing the data fitting (R^2) of Equation 6.3 when associated to the first sampled diameter of the considered sequence of sampled data. This optimal time value has been calculated after switching to a logarithmic representation of the problem as shown in Equation 6.4.

Eventually the method assures interpolations with R^2 values very close to the unit.

$$\ln[D(t) - D_0] = \ln a_D + n_D \ln t \tag{6.4}$$

The instantaneous time-resolved regression rate is defined as the time derivative of the diameters, so the quasi-steady regression rate results to be:

$$r_f(t) = \frac{d}{dt}\left(\frac{\overline{D}(t) - D_0}{2}\right) = \frac{1}{2}\, a_D \, n_D \, (t - t_0)^{n_D - 1} \qquad t \geq t_{ign} > t_0 \tag{6.5}$$

Where for $n < 1$, the regression rate results to be a monotonically decreasing function of time in accordance with the physics of the problem. Starting from this analytical continuous function, all the other ballistic parameters of interest can be calculated, in order: the oxidizer mass flux G_{Ox}, the fuel mass flow rate $\dot{m}_f$, and the oxidizer to fuel ratio O/F:

$$G_{Ox}(t) = \frac{\dot{m}_{Ox}}{\pi \dfrac{\overline{D}^2}{4}} = \frac{\dot{m}_{Ox}}{\pi \dfrac{[D_0 + a_D \, (t - t_0)^{n_D}]^2}{4}} \qquad t \geq t_{ign} > t_0 \tag{6.6}$$

$$\begin{aligned} \dot{m}_f(t) &= \rho_f \, A_f \, r_f = \rho_f \, \pi \, \overline{D} \, L_p \, r_f = \\ &= \frac{1}{2}\, \rho_f \, \pi \, L_p \, [D_0 + a_D \, (t - t_0)^{n_D}] \, a_D \, n_D \, (t - t_0)^{n_D - 1} \qquad t \geq t_{ign} > t_0 \end{aligned} \tag{6.7}$$

$$
\begin{aligned}
O/F(t) &= \frac{\dot{m}_{Ox}}{\dot{m}_f} = \frac{\dot{m}_{Ox}}{\rho_f\, \pi\, \overline{D}\, L_p\, r_f} = \\
&= \frac{\dot{m}_{Ox}}{\frac{1}{2}\, \rho_f\, \pi\, L_p\, [D_0 + a_D\, (t-t_0)^{n_D}]\, a_D\, n_D\, (t-t_0)^{n_D-1}} \qquad t \geq t_{ign} > t_0
\end{aligned}
\tag{6.8}
$$

Where $\dot{m}_{Ox}$ is the constant value of the oxidizer mass flow rate (210 Nlpm), ρ_f the fuel density, L_p the length of the fuel grain, A_f the combustion surface. The achieved regression rate versus oxidizer mass flux trend can be approximated accordingly to the following power law:

$$
r_f(G_{Ox}) = a_r\, G_{Ox}^{n_r} \tag{6.9}
$$

The results obtained with the *Analytical* method are shown in Figures 6.7 and 6.8 for a typical single test analysis, note the high R^2 values.

Every single test has been treated with the presented procedure, leading to a set of curves for each formulation tested. These curves can be condensed in a single one, providing an ensemble average of the single tests. In this manner is possible to have a single diameter evolution in time (Figure 6.9) and a single regression rate evolution versus oxidizer mass flux (Figure 6.10) that characterizes the investigated formulation.

As a convenient example, power law coefficients of Equation 6.3 and Equation 6.9 are presented in Tables 6.1 and 6.2 for SW formulation burning in GOX at chamber pressure of 16 bar, in which the achieved high data fitting can be noted.

Table 6.1: SW burning in GOX at 16 bar: interpolation of sampled diameter changes in time.

Test	a_D	n_D	R^2
Test no. 01	3.755 ± 0.044	0.660 ± 0.010	0.998
Test no. 02	3.350 ± 0.059	0.665 ± 0.012	0.996
Test no. 03	3.890 ± 0.026	0.611 ± 0.010	0.998
Ensemble	3.640 ± 0.051	0.666 ± 0.012	0.989

Results achieved by time-resolved analytical technique are checked by consistency with TOT data (see Equations 6.10, 6.11, 6.12) in order to gain information on consistency between different data reduction techniques. Checked results are collected in tables, see Table 6.3.

Table 6.2: SW burning in GOX at 16 bar: approximation of the regression rate versus the oxidizer mass flux.

Test	a_r	n_r	R^2
Test no. 01	0.025 ± .0002	0.835 ± .0019	0.949
Test no. 02	0.020 ± .0002	0.848 ± .0022	0.938
Test no. 03	0.046 ± .0002	0.708 ± .0007	0.989
Ensemble	0.028 ± .0003	0.805 ± .0021	0.939

$$r_f(t_{ign}) = \frac{1}{2}\, a_D\, n_D\, (t_{ign} - t_0)^{n_D - 1} =? \frac{n_D}{2} \frac{\overline{D}(t_{ign}) - D_0}{t_{ign} - t_0} \tag{6.10}$$

$$r_f(t_{final}) = \frac{1}{t_{final} - t_{ign}} \int_{t_{ign}}^{t_{final}} r_f(t)dt =? \frac{n}{2} \frac{\overline{D}(t_{final}) - \overline{D}(t_{ign})}{t_{final} - t_{ign}} \tag{6.11}$$

$$G_{Ox}(t_{final}) = \frac{1}{t_{final} - t_{ign}} \int_{t_{ign}}^{t_{final}} G_{Ox}(t)dt =? \frac{\dot{m}_{Ox}}{\frac{\pi}{4}[(\overline{D}(t_{ign}) - \overline{D}(t_{final}))/2]^2} \tag{6.12}$$

Table 6.3: Consistency checks for single tests by TOT.

Test	Equation 6.10	Equation 6.11	Equation 6.12
Test no. 01	+0.3%	-6.0%	+3.5%
Test no. 02	-3.1%	+2.6%	-2.6%
Test no. 03	-0.1%	-1.2%	-0.4%

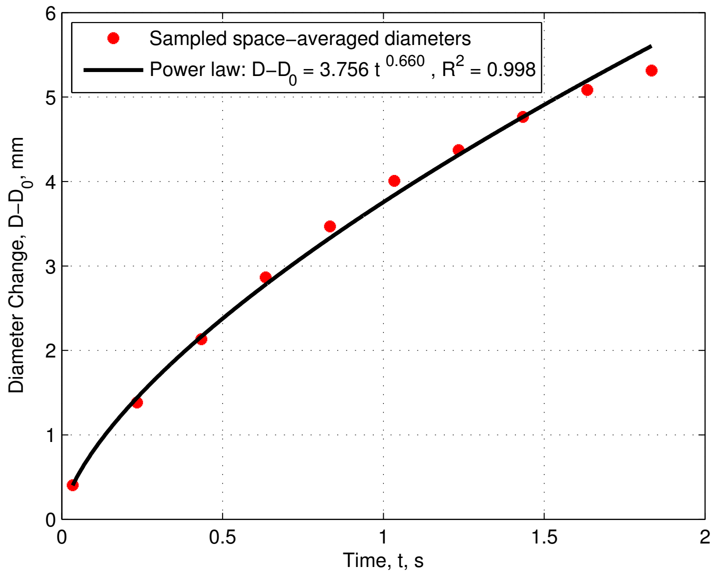

Figure 6.7: SW burning in GOX at 16 bar, Test no. 1: space-averaged diameter evolution in time and power-law approximation from Equation 6.3. Error bars not reported for better readability.

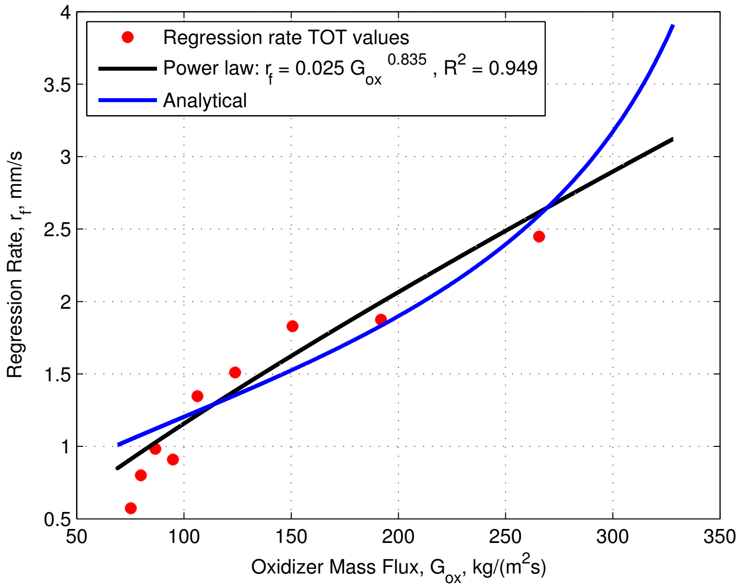

Figure 6.8: SW burning in GOX at 16 bar, Test no. 1: regression rate evolution versus oxidizer mass flux, power-law approximation from Equation 6.9 and analytical evaluation from Equations 6.5 and 6.6. Error bars not reported for better readability.

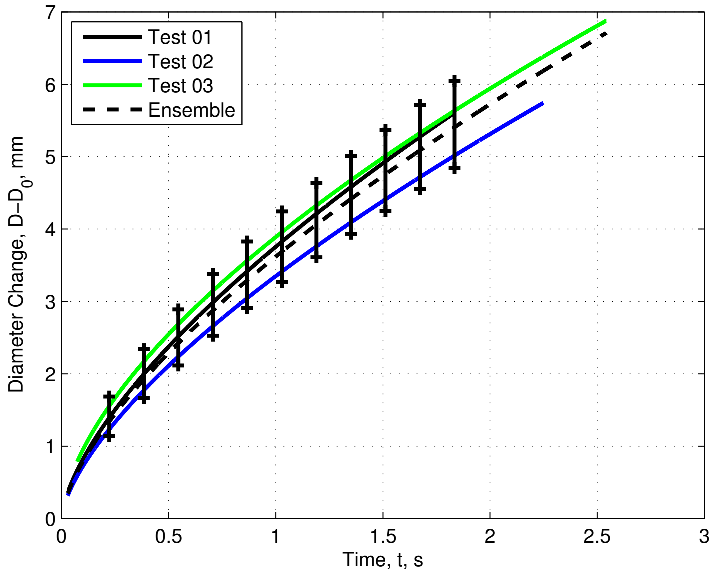

Figure 6.9: SW burning in GOX at 16 bar: mean diameter evolution in time and ensemble of the three single tests performed, power-law approximation.

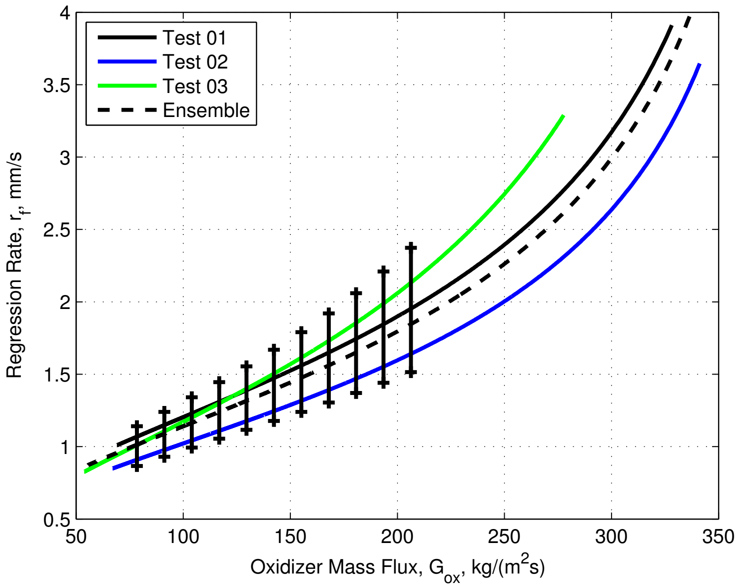

Figure 6.10: SW burning in GOX at 16 bar: singles and ensemble curves of the regression rate evolution versus oxidizer mass flux of the three single tests performed.

CHAPTER

7

EXPERIMENTAL RESULTS

This work aimed at:

- providing a relative ballistic grading of paraffin-based fuels with respect to HTPB under different operating conditions;
- relative ballistic grading of a series of different paraffin-based fuels loaded with different energetic additives (metals and hydrides);

All the tests were executed on cylindrical solid fuel samples with single central port perforation, as discussed in Chapter 4. Aim of the work was comparing the performances of different formulations or of the same formulation at different operating conditions. An overview of the performed tests is reported in Table 7.1, oxidizer flow rate and pressure were maintained constant during the combustion, thus granting quasi-steady operating conditions.

The data were processed following the steps defined in Chapter 6. Single tests data were condensed in an ensemble curve that was defined starting from single test diameter evolution in time (Equation 6.3) that are interpolated by an overall power law fitting. Regression rate and other ballistic parameters of each formulation were calculated from this ensemble, in particular, for single tests as well as for ensemble average data, the following operating steps were followed:

- diameter change in time was defined by interpolation with power law;
- time-resolved regression rate evolution was defined by time derivative of diameter change in time;
- oxidizer and fuel mass fluxes and oxidizer to fuel ratio evolution in time were evaluated;
- ballistics curve of regression rate versus oxidizer mass flux was determined, and a power law approximation of r_f versus G_{Ox} was calculated (see Equation 2.21);

Qualitative behavior of this parameters can be described as follows: as a result of the central port diameter increase in time, the oxidizer mass flux exhibits a monotone decrease during the test (see Equation 6.6), thus regression rate decreases in time too. Combustion surface along the grain increases as diameter increases, thus fuel mass flux given by Equation 6.7 is subjected to two contrasting effects: a r_f decrease and a A_f increase, the first is predominant: the fuel mass flux decreases in time while the oxidizer to fuel ratio O/F increases. The typical trends of the mentioned ballistic parameters are shown in Figures 7.1 and 7.2.

The ensemble curves referring to regression rate versus oxidizer mass flux are associated with a number of error bars displayed in each graphic.

Table 7.1: Performed tests summary, all the tests were performed under GOX and with an initial nominal oxidizer mass flux of $\approx 390 kg/m^2 s$.

Fuel	Number of tests performed	Oxidizer flow $[Nlpm]$	Pressure $[bar]$
SW	3	210	16
SW	4	210	13
SW	3	210	7
SW w/o SA	3	210	16
SW w MgB	3	210	16
SW w nFe	3	210	10
SW w AlH_3	3	210	16
SW w MgH_2	3	210	16
SW w LAH	3	210	16
SW w 3LAH	3	210	16
SW w μAl	3	210	16
SW w μAl Flaked	3	210	16

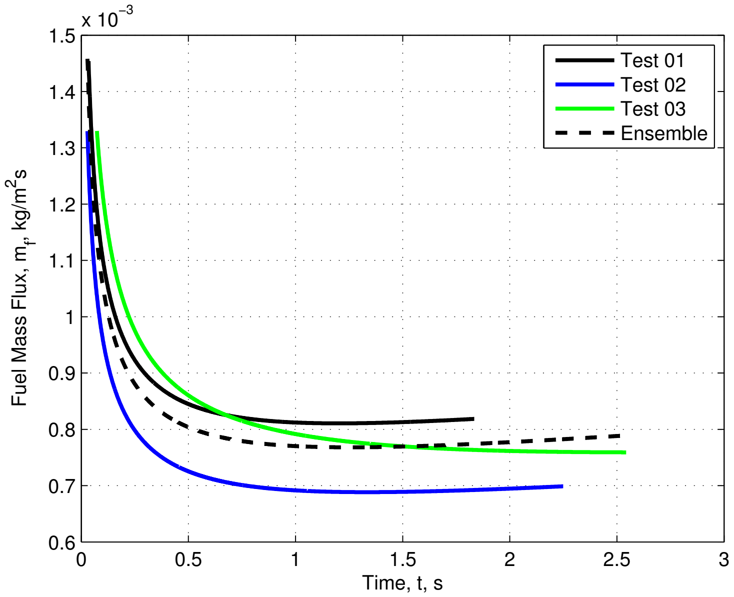

Figure 7.1: SW burning in GOX at 16 bar: fuel mass flux evolution in time and ensemble of the three single tests performed.

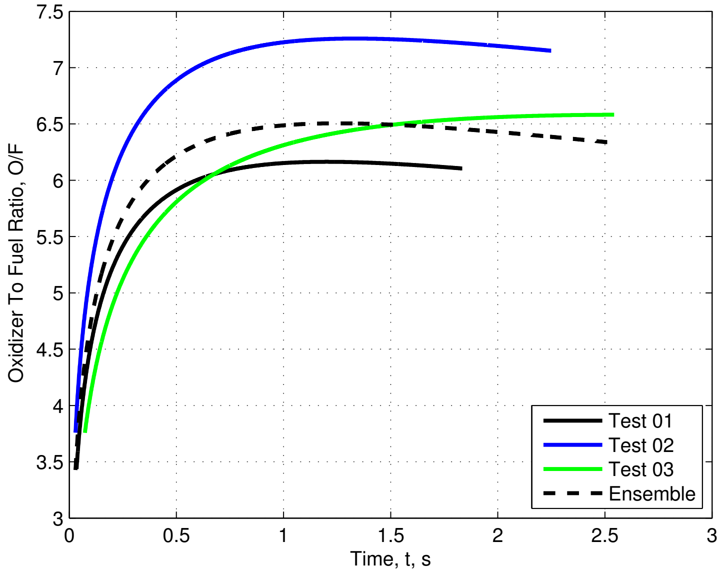

Figure 7.2: SW burning in GOX at 16 bar: oxidizer to fuel ratio evolution in time and ensemble of the three single tests performed.

These error bars are a concise indication of the dispersion of the single tests around the corresponding ensemble. Proper error bars were defined in t and G_{Ox} domains, respectively for Equation 6.3 and Equation 6.9. In order to evaluate the error bars for a given ensemble, a proper time or G_{Ox} range is evaluated considering the limits where the curves of all performed single tests are defined. Over this latter interval, error bars are evaluated by confidence intervals centered on the average value resulting from single test diameters at a given time (for Equation 6.3) or regression rates at a given Gox (for Equation 6.9). Confidence intervals were evaluated by 95% accuracy.

7.1 Ballistic analysis

In the following subsections the results of the relative ballistic grading of the investigated formulations are presented and discussed. Moreover, for each fuel formulation, instantaneous regression rate versus oxidizer mass flux is compared to the one of HTPB burning under similar operating conditions (same geometry, pressure, oxidizer type and flow) and considered as baseline. In this way it was possible to evaluate the regression rate enhancement realized by paraffin-based fuels with respect to HTPB.

7.1.1 SW at different pressures

The reference paraffin wax formulation, SW, a mixture of paraffin with amounts of Stearic acid (10%), and graphite (2%), (see Appendix B for details), was tested at different chamber pressures. The aim was to evaluate a possible influence of this parameter on SW ballistics.

A typical diameter evolution in time realized by paraffin-based fuels is shown in Figure 7.3, in which is possible to esteem the good quality of combustion in terms of regularity of the circular central port perforation, that is absence of anisotropies due to irregular burning along different radial directions.

Figures 7.7, 7.6 and 7.5 show a comparison between regression rates versus oxidizer flux for SW formulation and HTPB baseline, at 7, 13 and 16 bar. The first observation that is possible to do is that SW fuel produces a regression rate enhancement with respect to HTPB over all the investigated G_{Ox} range and for all the investigated pressures.

Note also that for SW fuel, in contrast to HTPB, a significant r_f difference subsists at high G_{Ox} between time-resolved r_f and power law approximating function. This difference is especially appreciable in high r_f formulations as SW burning at a chamber pressure of 7 bar (Figure 7.5).

Table 7.3 shows the percentage increases of SW fuel r_f with respect to HTPB r_f burning under similar conditions. Paraffin-based formulations show an increasing r_f enhancement for decreasing pressure. Under the investigated conditions, considering a G_{Ox} of 200 kg/m^2s, r_f enhancement with respect to baseline is of 293% at 7 bar, 231% at 13 bar and 187% at 16 bar. Table 7.3 shows also the average increment values $Av.$ and the corresponding standard deviation $St.D.$ values calculated considering the average of all the percentage increments reported. A high value of standard deviation with respect to the average corresponds to a higher r_f sensitivity to G_{Ox}. SW burning at 7 bar exhibits the higher sensitivity, as the power of the interpolation shown in Table 7.2 confirms. The resulting power law approximations of SW are collected in Table 7.2, they were found quite close to the available literature data [27].

Overall pressure effect in the pressure range from 7 to 16 bar can be noted in Figure 7.8. The data suggest a slight negative dependence of regression rate on pressure. The chamber pressure effect on r_f for SW fuel under the tested operating conditions was expressed by the following power law interpolation performed considering G_{Ox} and p_c as free parameters:

$$r_f\left(G_{Ox}, p_c\right) = (0.062 \pm 0.018)\, G_{Ox}^{(0.879\pm0.045)} p_c^{(-0.415\pm0.069)} \qquad R^2 = 0.908 \tag{7.1}$$

conversely, chamber pressure exhibits a no definite influence on HTPB fuel behavior [25], as is shown by the respective power law interpolation:

$$r_f\left(G_{Ox}, p_c\right) = (0.033 \pm 0.006)\, G_{Ox}^{(0.601\pm0.031)} p_c^{(-0.048\pm0.052)} \qquad R^2 = 0.857 \tag{7.2}$$

These approximations show how SW regression rate has a stronger p_c dependence than HTPB r_f (higher exponential interpolation coefficient). It is possible that changes in chamber pressure alter solid fuel melting and entrainment phenomena, hence pressure dependence could be related to the changes in the interaction between oxidizer flow and melted fuel for different chamber pressures: higher values of p_c promotes stability of liquid layer and thus lowers entrainment levels and r_f values.

Another behavior is that SW fuel presents higher data scattering of single tests at low pressures, that is larger error bars with respect to HTPB. Again, this effect could be due to the higher instabilities that the liquid layer on the combustion surface exhibits at low pressures. High data scattering for SW–fuels is also related to the poor mechanical properties of the paraffin grain. Due to low melting temperature and overall poor mechanical characteristics, SW can exhibit scattered ignition diameters affecting the first steps of the combustion process. These poor mechanical properties cause also frequent collapses during the combustion of paraffin-based fuels, this was the main reason why normally only three successful tests for formulation was performed. The low number of single tests per formulation in turn causes larger error bars due to higher Student's t values.

7.1.2 SW loaded with hydrides

The reference paraffin wax formulation, SW, was doped with metal hydrides (see appendix B for exact composition). Hydrides mass fraction into SW fuel was defined in order to provide metal content equi-molar with the aluminum content of a 11.2% aluminum hydride loaded SW fuel. The latter was considered as the reference for loaded fuel formulations tested in this work. All the hydrides loaded SW fuels was tested at the reference pressure of 16 bar.

Regression rate of this doped formulations was compared to SW regression rate at the same operating condition (16 bar) with the aim of investigating the achieved enhancement. As is shown in Figure 7.4 combustion in hydrides doped fuels maintains good quality, with no visible anisotropies. The typical behavior, especially with lithium containing hydrides, is the release of supposed spherical CCP detaching from regressing surface and then transported downstream by the core flow.

Two formulations with single metal hydrides were tested, one with AlH_3 and one with MgH_2. As can be seen in Figure 7.9, both formulations have given an increase in regression rate in respect to SW, but MgH_2 was slightly more effective than AlH_3. This could be explained considering the relative ease and effective ignition of MgH_2 with respect to AlH_3. During the combustion process the former, due to a easier ignition, could be more effective in delivering energy (by combustion and radiation) towards the solid fuel grain.

The lower performances of AlH_3 doped SW fuel burning under these operating conditions can be explained also considering the high average particle size of *Alane*. Both hydrides burn following a similar mechanism: during heating the hydride suffers a loss of hydrogen (dehydrogenation), then the metal reacts with oxygen, but aluminum particles reacts slowly being of larger size than magnesium ones. Slower chemical reaction means slower energy release towards the grain leading to lower r_f.

The two formulations containing lithium aluminum hydride and exahydride were prepared without stearic acid (SA), in order to avoid dangerous exothermic reactions between the hydrides and the acid during the manufacturing process that can lead to a loss of gaseous hydrogen. For this reason a SW formulation without stearic acid was prepared for comparison purposes. Lithium aluminum hydrides doped formulations are shown in Figure 7.10, compared to SW and SW without SA fuels.

Table 7.5 shows the percentage r_f increases of hydrides doped SW in respect to HTPB fuel under the investigated conditions. It can be noted that *LAH* doped fuel exhibits the highest enhancements with respect to all other hydrides doped fuels due to *LAH* high reactivity (low dehydrogenation temperature). For a G_{Ox} of 200 kg/m^2s, the fuels show increases of 267% (AlH_3 doped), 304% (MgH_2 doped), 448% (*LAH* doped) and 314% (*3LAH* doped). As predictable, the most effective additive in the investigated range of fluxes resulted to be *LAH*.

Sensitivity of AlH_3 doped SW fuel to G_{Ox} seems to be quite similar to what SW fuel exhibits (see St.D. in Table 7.5), while all the other hydrides exhibits a higher sensitivity than SW. Therefore, in general, doped SW fuel formulations show a notable dependence on G_{Ox}, with MgH_2, *LAH* and *3LAH* doped fuels having a higher power in the interpolation law (see Table 7.4).

Noteworthy, paraffin without stearic acid exhibits higher regression rates with a significant increase with respect to SW fuel under similar conditions: at a G_{Ox} value of 200 kg/m^2s SW w/o SA realizes 278% in respect to HTPB, higher than SW increment at the same flux (see Table 7.3). SA was added into SW fuel is order to achieve mechanical properties enhancement. Removal of this ingredient probably leads to a faster combustion due to higher fuel melting with respect to standard SW formulation.

7.1.3 SW loaded with metals

The standard paraffin wax formulation, SW, was doped also with metal powders, in particular three micron-sized powders and one nano-sized were tested. Tested micron-sized particles included MgB90 (20% Mg) and two types of μAl powders, of which one was uncoated and with spherical shape, while the second was in a “flaked” shape and was coated with paraffin. The only nano-sized powder tested was a nFe powder (see appendix B for exact composition).

Magnesium-boron doped fuel was tested at a chamber pressure of 13 bar while aluminum doped fuels were tested at 16 bar and nano-iron doped at 10 bar.

MgB loaded SW (Figure 7.11) exhibits a marginal regression rate increase with respect to SW, and only at high oxidizer fluxes. Between the metal powders doped fuels tested, MgB doped fuel proved to be the most sensitive to G_{Ox} under the operating conditions, as shown in the corresponding St.D. value reported in Table 7.7. The behavior was probably due to the high magnesium reactivity. Ballistics of MgB doped fuel is thus characterized by a strong dependence from oxidizer mass flux (see power in Table 7.6).

Aluminum doped fuel realizes higher enhancements especially the uncoated type. As is shown in Table 7.7, at a G_{Ox} value of 200 kg/m^2s, MgB doped fuel have a 251% increase in respect to HTPB fuel, μAl and μAl Flaked doped fuels 273% and 223% respectively, while nFe doped fuel 308%, demonstrating to be probably the most effective metal additive tested. However this latter result is affected by very large dispersion of the single tests (large error bars). μAl, μAlF and nFe doped fuels exhibits a sensitivity to G_{Ox} stronger than SW fuel burning under similar conditions (see Table 7.7).

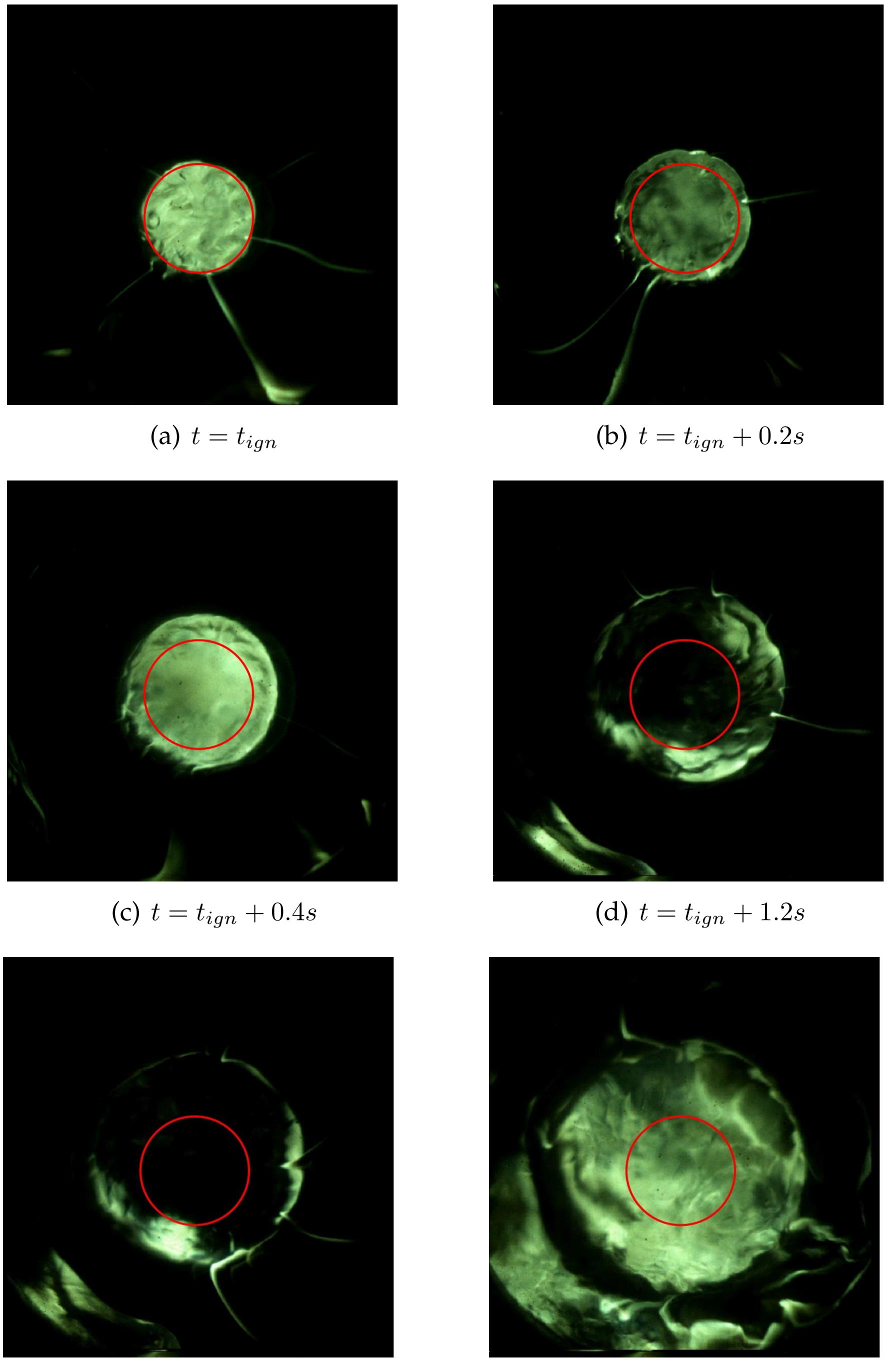

(a) $t = t_{ign}$

(b) $t = t_{ign} + 0.2s$

(c) $t = t_{ign} + 0.4s$

(d) $t = t_{ign} + 1.2s$

(e) $t = t_{ign} + 1.6s$

(f) $t = t_{ign} + 2.2s$

Figure 7.3: SW burning in GOX at 16 bar, Test no. 2: regression surface evolution in time (red circle marks initial nominal central port diameter, 4mm), video capturing rate is 250 fps.

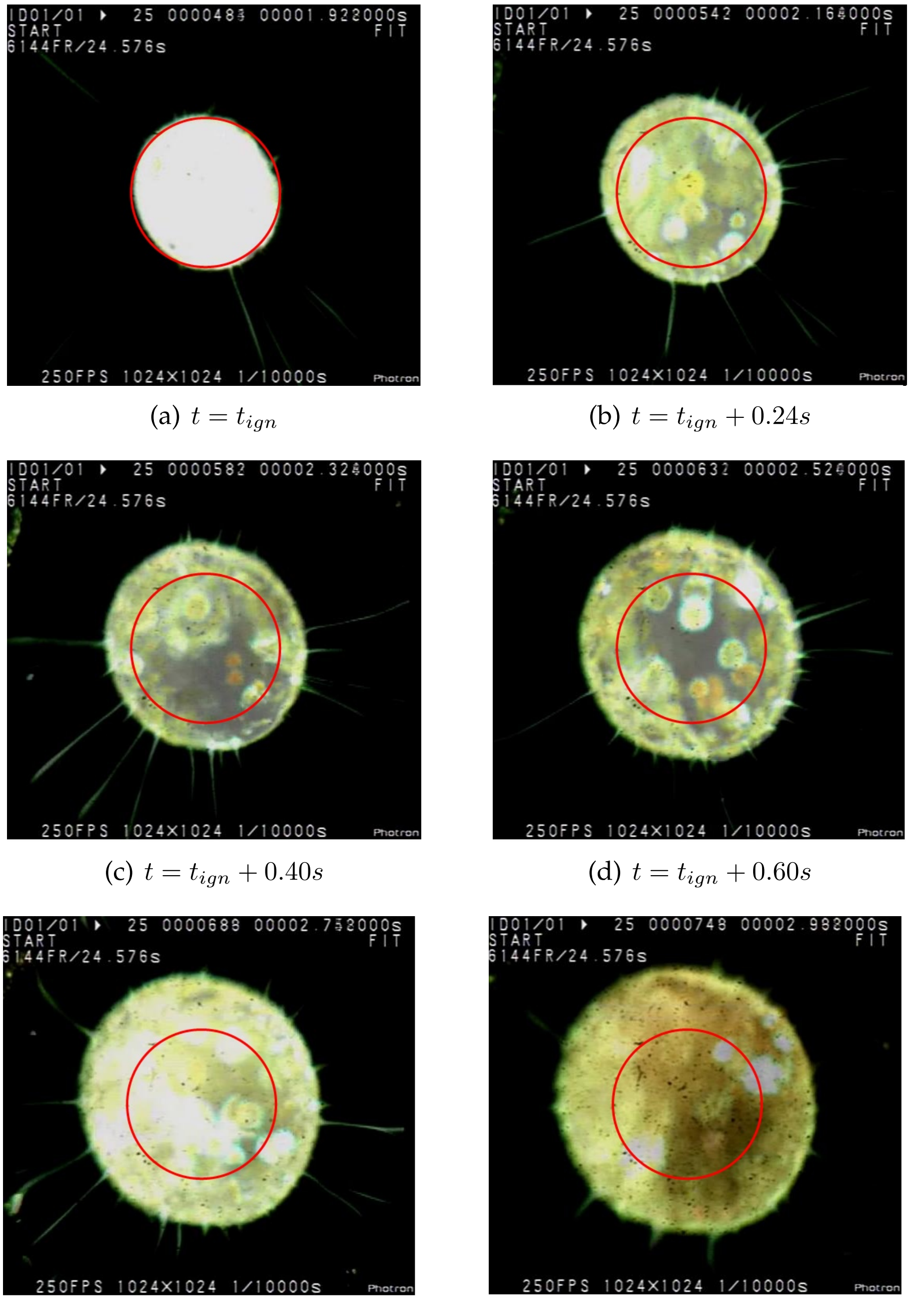

(a) $t = t_{ign}$

(b) $t = t_{ign} + 0.24s$

(c) $t = t_{ign} + 0.40s$

(d) $t = t_{ign} + 0.60s$

(e) $t = t_{ign} + 0.82s$

(f) $t = t_{ign} + 1.06s$

Figure 7.4: SW w 3LAH burning in GOX at 16 bar, Test no. 1: regression surface evolution in time (red circle marks initial nominal central port diameter, 4mm), video capturing rate is 250 fps.

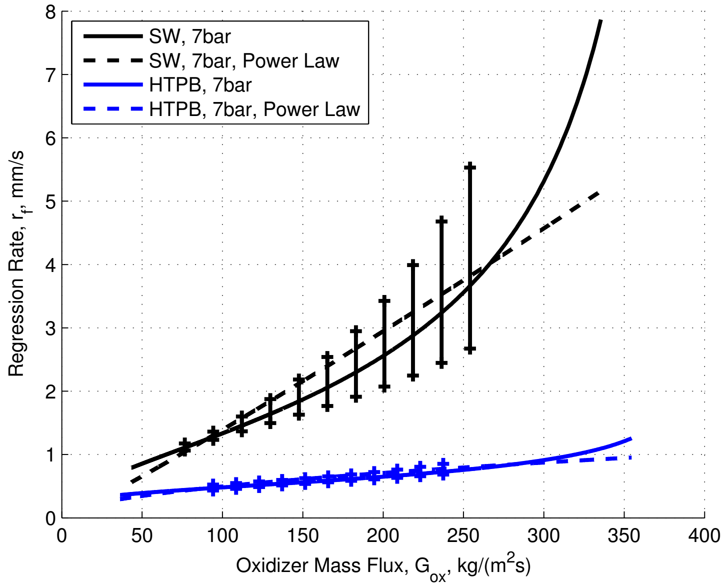

Figure 7.5: SW and HTPB burning in GOX at 7 bar: regression rate versus oxidizer mass flux, ensemble curves. Note very high r_f enhancement with respect to baseline over the whole G_{Ox} range.

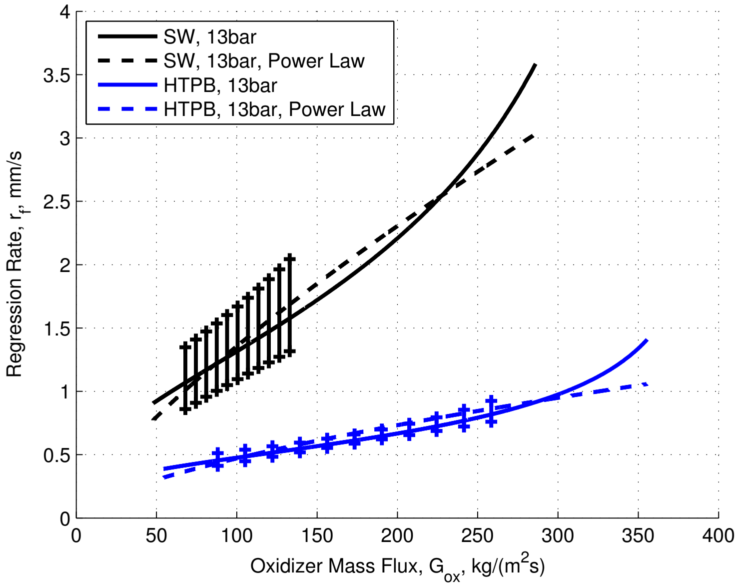

Figure 7.6: SW and HTPB burning in GOX at 13 bar: regression rate versus oxidizer mass flux, ensemble curves. Note significant r_f enhancement with respect to baseline over the whole G_{Ox} range.

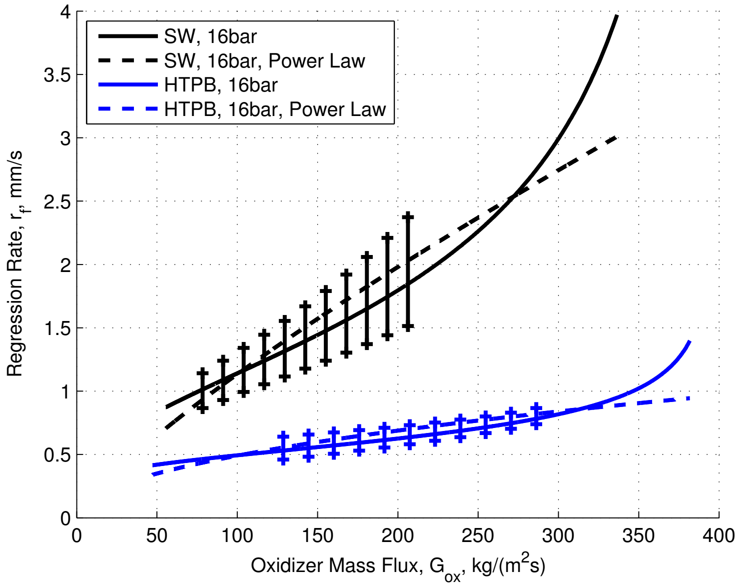

Figure 7.7: SW and HTPB burning in GOX at 16 bar: regression rate versus oxidizer mass flux, ensemble curves. Note significant r_f enhancement with respect to baseline over the whole G_{Ox} range.

Table 7.2: SW fuel burning in GOX under different chamber pressures: power law approximation of regression rate versus oxidizer mass flux of ensemble curves.

Fuel	a_r	n_r	R^2
SW, 7 bar	0.001 ± .0001	1.083 ± .0028	0.936
SW, 13 bar	0.040 ± .0003	0.765 ± .0014	0.966
SW, 16 bar	0.028 ± .0003	0.805 ± .0021	0.939

Table 7.3: SW fuel burning in GOX under different chamber pressures: percentage variations of r_f with respect to HTPB burning under similar conditions.

	G_{Ox} $[kg/m^2s]$							
Fuel [%]	100	150	200	250	300	350	Av.	St.D.
SW, 7 bar	178	233	293	370	483	/	311	120
SW, 13 bar	176	203	231	263	/	/	218	37
SW, 16 bar	131	158	187	220	266	/	193	53

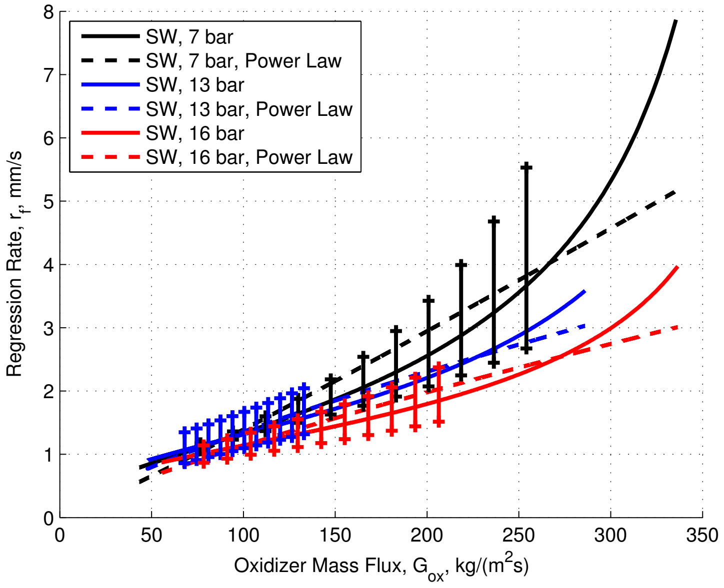

Figure 7.8: SW burning in GOX at 7, 13, 16 bar: regression rate versus oxidizer mass flux, ensemble curves. In spite of data scattering due to poor mechanical properties of the solid fuel grain, a decreasing trend of r_f for increasing p_c is achieved under the investigated conditions, as shown in Equation 7.1.

Table 7.4: Hydrides doped SW fuels burning in GOX at 16 bar: power law approximation of regression rate versus oxidizer mass flux of ensemble curves.

Fuel	a_r	n_r	R^2
SW w/o SA	0.054 ± .0003	0.718 ± .0011	0.977
SW w 11.2% AlH_3	0.036 ± .0003	0.791 ± .0014	0.970
SW w 9.8% MgH_2	0.023 ± .0002	0.900 ± .0018	0.961
SW w 7.1% LAH	0.021 ± .0001	0.957 ± .0011	0.988
SW w 5% 3LAH	0.012 ± .0002	1.053 ± .0033	0.909

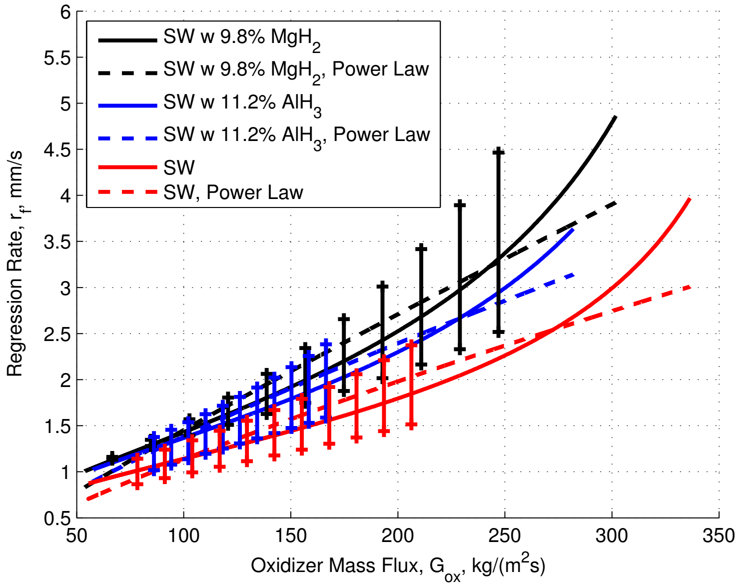

Figure 7.9: SW, SW w AlH_3 and SW w MgH_2 burning in GOX at 16 bar: regression rate versus oxidizer mass flux, ensemble curves. Higher enhancement is achieved with MgH_2 doped SW.

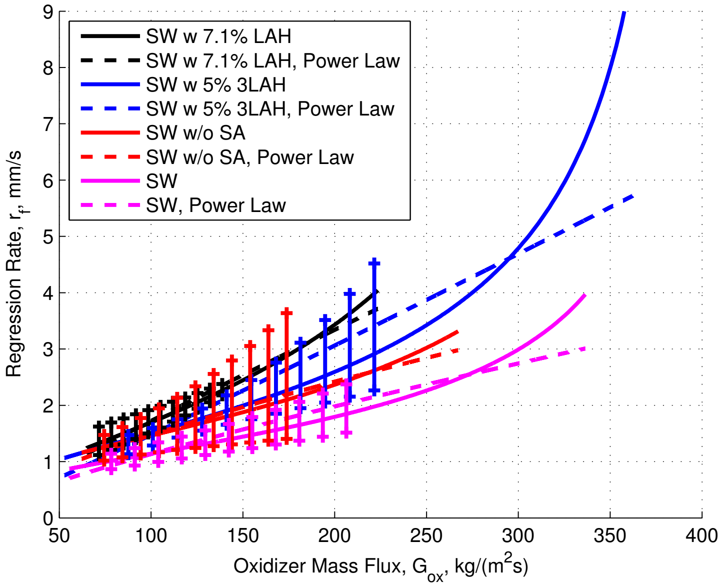

Figure 7.10: SW, SW w LAH and SW w 3LAH burning in GOX at 16 bar: regression rate versus oxidizer mass flux, ensemble curves. Note high r_f enhancement achieved by LAH doped SW fuel, even at low G_{Ox} values.

Table 7.5: Hydrides doped SW fuels burning in GOX at 16 bar: percentage variations of r_f with respect to HTPB burning under similar conditions.

	G_{Ox} $[kg/m^2s]$							
Fuel [%]	100	150	200	250	300	350	Av.	St.D.
SW w/o SA	196	236	278	328	/	/	260	56
SW w 11.2% AlH_3	177	221	267	324	/	/	247	63
SW w 9.8% MgH_2	190	244	304	377	486	/	320	116
SW w 7.1% LAH	244	338	448	/	/	/	343	102
SW w 5% 3LAH	205	257	314	384	486	683	388	174

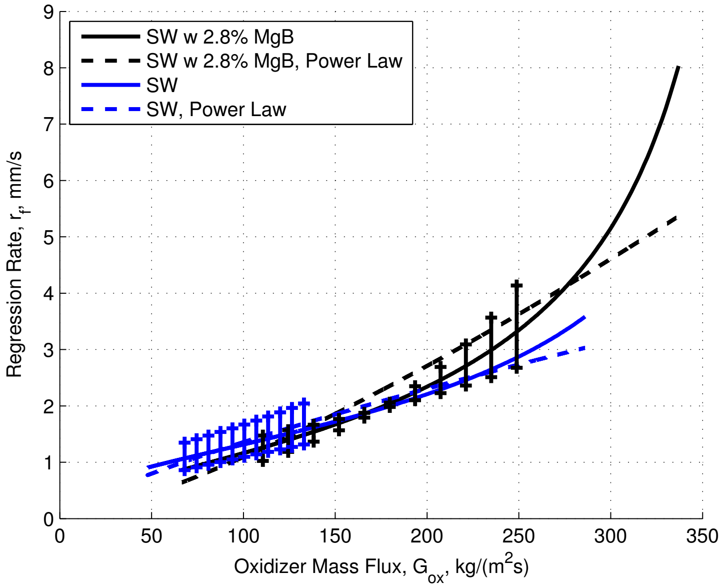

Figure 7.11: SW and SW w MgB burning in GOX at 13 bar: regression rate versus oxidizer mass flux, ensemble curves.

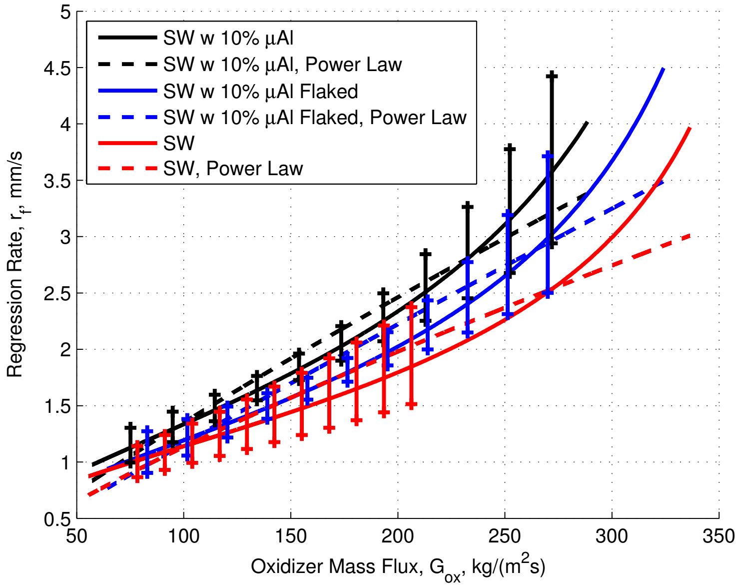

Figure 7.12: SW, SW w μAl and SW w μAl Flaked burning in GOX at 16 bar: regression rate versus oxidizer mass flux, ensemble curves.

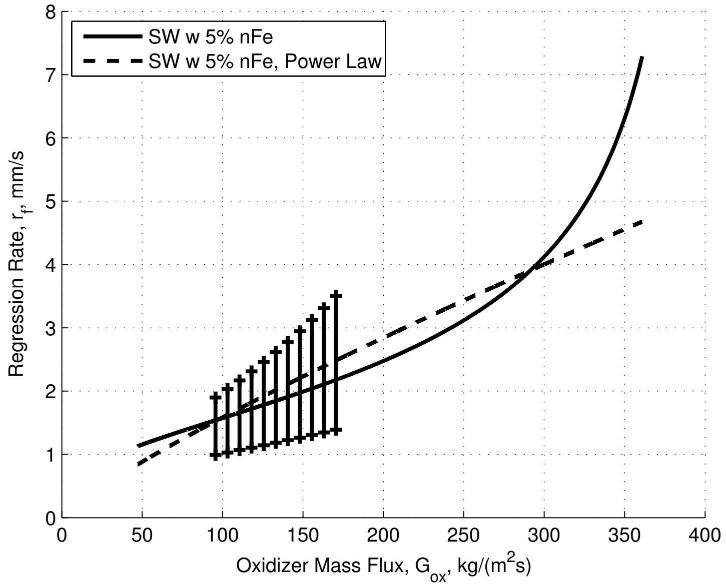

Figure 7.13: SW w nFe burning in GOX at 10 bar: regression rate versus oxidizer mass flux, ensemble curves.

Table 7.6: Metal doped SW fuels burning in GOX: power law approximation of regression rate versus oxidizer mass flux of ensemble curves.

Fuel	a_r	n_r	R^2
SW w 2.8% MgB	0.003 ± .0000	1.310 ± .0033	0.942
SW w 10% μAl	0.025 ± .0002	0.867 ± .0016	0.968
SW w 10% μAl Flaked	0.016 ± .0002	0.936 ± .0021	0.951
SW w 5% nFe	0.033 ± .0005	0.844 ± .0027	0.909

Table 7.7: Metal doped SW fuels burning in GOX: percentage variations of r_f with respect to HTPB burning under similar conditions.

	G_{Ox} $[kg/m^2s]$							
Fuel [%]	100	150	200	250	300	350	Av.	St.D.
SW w 2.8% MgB	144	195	251	322	428	/	268	111
SW w 10% μAl	170	220	273	340	/	/	251	73
SW w 10% μAl Flaked	142	181	223	275	349	/	234	81
SW w 5% nFe	247	278	308	343	390	471	340	81

CHAPTER

8

CONCLUSIONS

Ballistics of paraffin-based fuel (SW) was investigated in a 2D-radial laboratory-scale burner under GOX. All regression rate and other data were obtained by an optical time-resolved technique and verified by the corresponding TOT measurements. Pure HTPB was taken as the reference baseline for relative ballistic grading.

8.1 Ballistics results

The use of liquefying propellants such as paraffin permitted to overcome the main shortcoming of hybrid propulsion: the low regression rate of the solid grain. All the tested paraffin-based fuels exhibited higher regression rates than traditional HTPB-based fuels, in addition, the inclusion of additives to paraffin fuel has provided a further regression rate enhancement, especially at high oxidizer mass fluxes. In this respect, hydrides doped fuels have performed a higher enhancement than the metal doped, with magnesium hydride and lithium aluminum hydrides particularly effective even at low oxidizer fluxes. This behaviors were possibly due to the ease of ignition of magnesium and to the low dehydrogenation temperature of *LAH*.

SW fuel showed also a not negligible dependence from chamber pressure in the range 7-16 bar and, at the same time, an augmented single tests dispersion at the pressure reduction. This trend was probably due to the stabilizing effect on liquid layer stability of increasing chamber pressure.

8.2 Future developments

The work undertaken has also highlighted some possible future developments about the future work on paraffin-based fuels in *SPLab*:

- enlarge the investigation pressure range with the aim to confirm the emerged chamber pressure dependence trend, and to find the possible pressure limit values of this trend;
- further investigate the reasons behind high data scattering of paraffin-based fuel for decreasing pressure;
- investigation of additives capable of improving the poor mechanical properties of paraffin-based fuel without hampering the onset of the entrainment phenomenon, even at the expense of a slight decrease of regression rate;
- improve adherence between paraffin-based fuel sample and steel cylinder, in order to avoid the frequent detachment of the sample during the combustion tests due to the high flows. A possible solution could be an helical rifling of the cylinder's internal surface;
- study an effective entrainment visualization technique, in order to increase the spatial and temporal resolution, allowing to identify with more certainty the burning fuel droplets in the port, thus confirming further the existence of the entrainment phenomenon.

APPENDIX

A

OTHER RESULTS

A.1 SW fuel at chamber pressure of 4 bar

SW fuel has been tested also at 4 bar, regression rate trend obtained has diverged greatly from expectations, showing an opposite trend with respect to the one shown in Equation 7.1. As shown in Figure A.1, SW burning at 4 bar exhibits a lower regression rate than SW fuel tested at 7 bar starting from a G_{Ox} of 150 kg/m^2s. Moreover, under this operating conditions, paraffin-based fuel shows a lower sensitivity to oxidizer mass flux, as testified by the low slope of the curve.

Very high data scattering of single tests are achieved, with large error bars. This confirms the large dispersion of the single tests operating under very low pressure. The behavior further proves that combustion of paraffin at these low pressure values leads to higher instabilities of the fuel liquid layer that can cause data scattering.

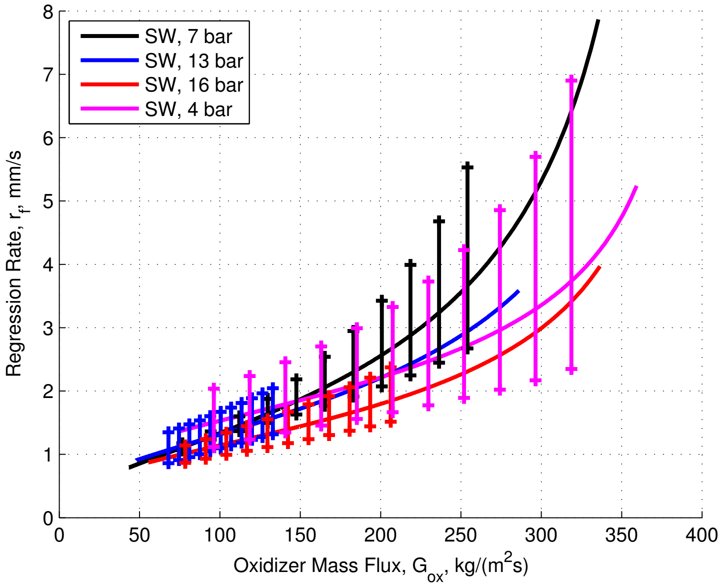

Figure A.1: SW burning in GOX at 4, 7, 13, 16 bar: regression rate versus oxidizer mass flux, ensemble curves. SW burning at chamber pressure of 4 bar exhibits very high data scattering and a opposite behavior than that expected.

Table A.1: SW fuel burning in GOX at 4, 7, 13, 16 bar: power law approximation of regression rate versus oxidizer mass flux of ensemble curves.

Fuel	a_r	n_r	R^2
SW, 4 bar	0.038 ± .0005	0.784 ± .0023	0.920
SW, 7 bar	0.001 ± .0001	1.083 ± .0028	0.936
SW, 13 bar	0.040 ± .0003	0.765 ± .0014	0.966
SW, 16 bar	0.028 ± .0003	0.805 ± .0021	0.939

A.2 Scale effects in hybrid motors

As explained in chapter 2.4.1, hybrid rocket motors have a complex combustion process with some unique features which differ considerably from those of other rocket engines. This characteristic makes difficult to define the scaling rules needed to compare different laboratory-scale tests or to determine the appropriate conditions under which a laboratory-scale hybrid rocket motor should be tested in order to predict the behavior of a full scale motor.

In order to identify the prevailing scale factors numerous studies have been done using similarity analysis. These analysis allow a greater understanding of the involved phenomena, saving time and money in the development of hybrid propulsion systems.

As reported in [39], in order to correctly interpret experimental results and extrapolate them to different scale systems, some main operating conditions have to be preserved: geometric similarity, same fuel and oxidizer combination, and scaling the oxidizer flow rate in proportion to the length scale.

A.2.1 Geometry

The first similarity requirement is the geometric similarity, it requires that a constant ratio between dimensions in different motors have to be maintained, typically length L and motor diameter D or initial port perforation diameter D_0. So it has to result:

$$L \propto D_0 \tag{A.1}$$

A.2.2 Transport phenomena

Transport phenomena have a fundamental importance in the overall combustion process of hybrid rocket motors, they affect the boundary layer, the heat transfer mechanism, and all the flame parameters such as diffusion and mixing of oxidizer, fuel and combustion products. because of the turbulent internal flow, the most significant parameter is the Reynolds number, Re. The similarity of the transport phenomena is thus achieved when the Reynolds number are the same:

$$Re = \frac{\rho u D}{\mu} = const \tag{A.2}$$

In regard to heating regime, the similarity is achieved by keeping constant the ratio between the heat transfer to the wall and the overall heat generated. Given the turbulent nature of the flow, heat exchange in hybrid motors is dominated by convection, and only minimally influenced by radiation, so it is possible to obtain:

$$h\left(T_f - T_w\right) D^2 \propto \rho u D^2 c_p \left(T_c - T_i\right) \tag{A.3}$$

Where h, T_f, T_w, T_c, T_i are respectively the convective heat transfer coefficient and the flame, wall, final average and initial temperatures. If a similarity of temperature fields is maintained then Equation A.3 implies that Nusselt number is constant. In the hybrid combustion regime this requirement is fulfilled by the constancy of Reynolds and Prandtl numbers, since Nusselt results dependent on both, as saw in Equation 2.13.

A.2.3 Chemistry

Similarity of chemical kinetics requires the similarity of temperature and chemical species concentration fields. This can be achieved using the same oxidizer-fuel combination and the same ratio oxidizer to fuel ratio O/F. Also other additional requirements are needed, Characteristic chemical time of hydrocarbon fuels is inversely proportional to pressure $\tau_{ch} \propto 1/p$ while residence time can be approximated by $\tau_{res} \propto D/u$. Similarity of flameholding characteristics requires that τ_{ch}/τ_{res} leading to:

$$\frac{u}{pD} = const \tag{A.4}$$

If this similarity condition and Reynolds number conditions are satisfied the so called *"pD scaling"* equation is achieved:

$$pD = const \tag{A.5}$$

A.2.4 Compressibility

The similarity for compressibility effects is maintained operating at the same Mach number, M:

$$M = \frac{u}{\sqrt{\gamma R T}} \tag{A.6}$$

such requirement would be fulfilled for simultaneous existence of similar velocity and temperature fields.

A.2.5 Theoretical Model Predictions

The minimal and most important conditions that allow to reach the similarity requirements useful for scaling hybrid rocket motors are:

- Geometric similarity;
- Same fuel and oxidizer combination;
- Same Reynolds number;

The requirement of constancy of Reynolds number in systems under similarity conditions implies that flow rate should be proportional to the port diameter:

$$GD = const \qquad \frac{\dot{m}}{D} = const \qquad O/F = const \tag{A.7}$$

Maintaining the above mentioned three main operating conditions, the main hybrid system parameters result to be related in the following manner for different scale systems:

Fuel regression rate

Regression rate is related to the wall heat flux $\dot{q}_w = h\left(T_f - T_w\right)$ and the heat of vaporization h_v:

$$r_f = \dot{q}_w / \left(\rho h_v\right) \tag{A.8}$$

where, introducing an appropriate correlation between Nusselt and Reynolds number, it is possible to obtain:

$$r_f = aG^n D^{n-1} \tag{A.9}$$

when operating under similarity conditions, it is not necessary to assume the most appropriate value of n, regression rate anyway results to satisfy:

$$r_f D = const \tag{A.10}$$

Thrust and specific impulse

For equal O/F the theoretical characteristic velocity does not change, $c^* = const$, so also the theoretical specific impulse results to be constant:

$$I_{sp} = \frac{C_T c^*}{g_0} = const \tag{A.11}$$

in which $C_T = T/\left(pA_t\right)$ and $c^* = pA_t/\dot{m}$, while thrust would roughly scale with motor size:

$$T = C_T c^* \dot{m} \propto D \tag{A.12}$$

APPENDIX

B

FUEL FORMULATIONS AND SINGLE TEST RESULTS

This appendix reports various tables for each produced and investigated fuel. Informations about composition, ingredients' weight and percentage by mass, are shown. Other tables reports consistency checks, as explained in section 6.3.2, and power law approximation coefficients for each single test, for both diameter versus time and regression rate versus oxidizer mass flux evolution.

B.1 SW reference formulation

B.1.1 SW tested at 7 bar (manufacturing Nov. 2011)

	Nominal percentage [%]	Nominal weight [g]	Actual weight [g]	Actual percentage [%]
Paraffin Wax	88.00	55.056	55.056	87.984
Stearic Acid	10.00	6.256	6.267	10.015
Graphite	2.00	1.251	1.252	2.000

Test	Eq. 6.10	Eq. 6.11	Eq. 6.12
Test no. 01	+0.0%	-0.3%	+4.6%
Test no. 02	+0.3%	-1.1%	+5.4%
Test no. 03	-0.2%	-3.4%	-3.2%

Test	a_D	n_D	R^2
Test no. 01	4.593 ± 0.018	0.523 ± 0.003	1.000
Test no. 02	4.443 ± 0.022	0.576 ± 0.003	1.000
Test no. 03	4.144 ± 0.070	0.612 ± 0.010	0.998
Ensemble	4.415 ± 0.079	0.582 ± 0.012	0.989

Test	a_r	n_r	R^2
Test no. 01	0.006 ± .0001	1.174 ± .0016	0.980
Test no. 02	0.004 ± .0001	1.232 ± .0030	0.945
Test no. 03	0.016 ± .0002	0.964 ± .0027	0.929
Ensemble	0.001 ± .0001	1.083 ± .0028	0.936

B.1.2 SW tested at 13 bar (manufacturing Feb. 2011)

	Nominal percentage [%]	Nominal weight [g]	Actual weight [g]	Actual percentage [%]
Paraffin Wax	88.00	60.160	60.160	87.873
Stearic Acid	10.00	6.836	6.936	10.131
Graphite	2.00	1.367	1.367	1.996

Test	Eq. 6.10	Eq. 6.11	Eq. 6.12
Test no. 01	-0.2%	+1.6%	-2.5%
Test no. 02	+0.1%	-1.2%	+4.3%
Test no. 03	+0.1%	-1.4%	-0.7%
Test no. 04	+0.3%	-2.9%	-2.9%

Test	a_D	n_D	R^2
Test no. 01	5.019 $\pm$ 0.023	0.601 $\pm$ 0.008	0.999
Test no. 02	4.238 $\pm$ 0.031	0.534 $\pm$ 0.008	0.998
Test no. 03	3.868 $\pm$ 0.013	0.650 $\pm$ 0.007	0.999
Test no. 04	3.786 $\pm$ 0.016	0.685 $\pm$ 0.004	0.999
Ensemble	4.178 $\pm$ 0.077	0.616 $\pm$ 0.022	0.945

Test	a_r	n_r	R^2
Test no. 01	0.091 $\pm$ .0002	0.646 $\pm$ .0005	0.994
Test no. 02	0.010 $\pm$ .0001	1.050 $\pm$ .0015	0.983
Test no. 03	0.087 $\pm$ .0002	0.578 $\pm$ .0004	0.996
Test no. 04	0.069 $\pm$ .0005	0.635 $\pm$ .0013	0.958
Ensemble	0.040 $\pm$ .0003	0.765 $\pm$ .0014	0.966

B.1.3 SW tested at 16 bar (manufacturing Feb. 2011)

	Nominal percentage [%]	Nominal weight [g]	Actual weight [g]	Actual percentage [%]
Paraffin Wax	88.00	58.299	58.299	87.981
Stearic Acid	10.00	6.625	6.633	10.010
Graphite	2.00	1.325	1.331	2.009

Test	Eq. 6.10	Eq. 6.11	Eq. 6.12
Test no. 01	+0.3%	-6.0%	+3.5%
Test no. 02	-3.1%	+2.6%	-2.6%
Test no. 03	-0.1%	-1.2%	-0.4%

Test	a_D	n_D	R^2
Test no. 01	3.755 ± 0.044	0.660 ± 0.010	0.998
Test no. 02	3.350 ± 0.059	0.665 ± 0.012	0.996
Test no. 03	3.890 ± 0.026	0.611 ± 0.010	0.998
Ensemble	3.640 ± 0.051	0.666 ± 0.012	0.989

Test	a_r	n_r	R^2
Test no. 01	0.050 ± 0.003	0.692 ± 0.011	0.958
Test no. 02	0.045 ± 0.002	0.684 ± 0.010	0.950
Test no. 03	0.058 ± 0.001	0.657 ± 0.004	0.990
Ensemble	0.030 ± 0.000	0.805 ± 0.002	0.939

B.1.4 SW tested at 4 bar (manufacturing Nov. 2011)

	Nominal percentage [%]	Nominal weight [g]	Actual weight [g]	Actual percentage [%]
Paraffin Wax	88.00	45.146	45.246	88.068
Stearic Acid	10.00	5.096	5.101	9.929
Graphite	2.00	1.028	1.029	2.002

Test	Eq. 6.10	Eq. 6.11	Eq. 6.12
Test no. 01	-0.2%	-3.8%	+5.0%
Test no. 02	+0.0%	-0.6%	-0.7%
Test no. 03	+0.4%	-4.9%	-1.6%

Test	a_D	n_D	R^2
Test no. 01	4.552 ± 0.045	0.622 ± 0.005	0.998
Test no. 02	3.684 ± 0.011	0.717 ± 0.002	0.999
Test no. 03	4.678 ± 0.069	0.738 ± 0.010	0.996
Ensemble	4.276 ± 0.174	0.685 ± 0.025	0.973

Test	a_r	n_r	R^2
Test no. 01	0.010 ± .0001	1.074 ± .0027	0.941
Test no. 02	0.031 ± .0003	0.781 ± .0021	0.933
Test no. 03	0.115 ± .0009	0.595 ± .0015	0.937
Ensemble	0.038 ± .0005	0.784 ± .0023	0.920

B.2 SW w AlH_3 (manufacturing Oct. 2011)

	Nominal percentage [%]	Nominal weight [g]	Actual weight [g]	Actual percentage [%]
Paraffin Wax	76.80	55.236	55.236	76.800
Stearic Acid	10.00	7.192	7.192	10.000
Graphite	2.00	1.438	1.438	2.000
AlH_3	11.20	8.055	8.055	11.200

Test	Eq. 6.10	Eq. 6.11	Eq. 6.12
Test no. 01	+0.4%	-1.3%	-1.4%
Test no. 02	-0.3%	+0.6%	+1.9%
Test no. 03	+1.6%	-8.3%	+3.3%

Test	a_D	n_D	R^2
Test no. 01	4.040 ± 0.028	0.653 ± 0.008	0.999
Test no. 02	4.008 ± 0.067	0.587 ± 0.014	0.997
Test no. 03	4.521 ± 0.050	0.565 ± 0.018	0.992
Ensemble	4.213 ± 0.062	0.621 ± 0.0167	0.982

Test	a_r	n_r	R^2
Test no. 01	0.062 ± .0003	0.668 ± .0009	0.982
Test no. 02	0.009 ± .0001	1.042 ± .0015	0.978
Test no. 03	0.037 ± .0001	0.792 ± .0006	0.995
Ensemble	0.036 ± .0003	0.791 ± .0014	0.970

B.3 SW w MgH_2 (manufacturing Oct. 2011)

	Nominal percentage [%]	Nominal weight [g]	Actual weight [g]	Actual percentage [%]
Paraffin Wax	78.18	43.470	43.470	78.168
Stearic Acid	10.00	5.560	5.567	10.011
Graphite	2.00	1.112	1.112	2.000
MgH_2	9.82	5.460	5.462	9.822

Test	Eq. 6.10	Eq. 6.11	Eq. 6.12
Test no. 01	+0.1%	-0.2%	+2.8%
Test no. 02	+0.4%	-3.0%	+3.1%
Test no. 03	+0.7%	-5.2%	+1.0%

Test	a_D	n_D	R^2
Test no. 01	4.649 ± 0.016	0.576 ± 0.003	1.000
Test no. 02	4.468 ± 0.051	0.605 ± 0.010	0.996
Test no. 03	4.186 ± 0.040	0.655 ± 0.010	0.995
Ensemble	4.414 ± 0.061	0.602 ± 0.012	0.988

Test	a_r	n_r	R^2
Test no. 01	0.013 ± .0001	1.028 ± .0018	0.969
Test no. 02	0.021 ± .0002	0.918 ± .0018	0.965
Test no. 03	0.058 ± .0003	0.695 ± .0012	0.972
Ensemble	0.023 ± .0002	0.900 ± .0018	0.961

B.4 SW w/o SA (manufacturing Oct. 2011)

	Nominal percentage [%]	Nominal weight [g]	Actual weight [g]	Actual percentage [%]
Paraffin Wax	98.00	80.011	80.011	97.777
Graphite	2.00	1.818	1.819	2.001

Test	Eq. 6.10	Eq. 6.11	Eq. 6.12
Test no. 01	+0.7%	-3.4%	-1.0%
Test no. 02	+0.6%	-1.3%	-0.1%
Test no. 03	+0.0%	+0.2%	+1.7%

Test	a_D	n_D	R^2
Test no. 01	4.285 ± 0.046	0.678 ± 0.012	0.996
Test no. 02	3.917 ± 0.047	0.647 ± 0.012	0.997
Test no. 03	5.113 ± 0.024	0.517 ± 0.006	0.999
Ensemble	4.407 ± 0.139	0.634 ± 0.035	0.926

Test	a_r	n_r	R^2
Test no. 01	0.089 ± .0004	0.615 ± .0009	0.979
Test no. 02	0.037 ± .0002	0.764 ± .0012	0.975
Test no. 03	0.018 ± .0001	0.984 ± .0008	0.994
Ensemble	0.054 ± .0003	0.718 ± .0011	0.977

B.5 SW w LAH (manufacturing Oct. 2011)

	Nominal percentage [%]	Nominal weight [g]	Actual weight [g]	Actual percentage [%]
Paraffin Wax	90.90	52.132	52.217	90.937
Graphite	2.00	1.147	1.154	2.010
LAH	7.10	4.062	4.050	7.053

Test	Eq. 6.10	Eq. 6.11	Eq. 6.12
Test no. 01	-0.1%	-0.1%	+2.4%
Test no. 02	+1.1%	-3.9%	+1.1%
Test no. 03	+0.0%	+0.4%	-0.8%

Test	a_D	n_D	R^2
Test no. 01	5.063 ± 0.027	0.537 ± 0.005	0.999
Test no. 02	4.981 ± 0.079	0.539 ± 0.029	0.986
Test no. 03	5.150 ± 0.017	0.613 ± 0.004	1.000
Ensemble	5.043 ± 0.047	0.5561 ± 0.011	0.993

Test	a_r	n_r	R^2
Test no. 01	0.015 ± .0001	1.030 ± .0011	0.989
Test no. 02	0.031 ± .0001	0.861 ± .0004	0.998
Test no. 03	0.070 ± .0002	0.714 ± .0006	0.992
Ensemble	0.021 ± .0001	0.957 ± .0011	0.988

B.6 SW w 3LAH (manufacturing Oct. 2011)

	Nominal percentage [%]	Nominal weight [g]	Actual weight [g]	Actual percentage [%]
Paraffin Wax	93.00	53.490	53.160	92.833
Graphite	2.00	1.151	1.190	2.078
3LAH	5.00	2.908	2.914	5.089

Test	Eq. 6.10	Eq. 6.11	Eq. 6.12
Test no. 01	+0.1%	-2.6%	+3.8%
Test no. 02	+0.2%	+1.5%	+1.5%
Test no. 03	-0.5%	-6.3%	+4.3%

Test	a_D	n_D	R^2
Test no. 01	4.508 ± 0.042	0.525 ± 0.008	0.999
Test no. 02	4.759 ± 0.044	0.544 ± 0.009	0.998
Test no. 03	4.251 ± 0.055	0.657 ± 0.008	0.999
Ensemble	4.574 ± 0.114	0.6232 ± 0.018	0.980

Test	a_r	n_r	R^2
Test no. 01	0.006 ± .0001	1.158 ± .0011	0.990
Test no. 02	0.014 ± .0001	1.021 ± .0012	0.987
Test no. 03	0.019 ± .0003	0.935 ± .0032	0.897
Ensemble	0.012 ± .0002	1.053 ± .0033	0.909

B.7 SW w MgB (manufacturing Apr. 2011)

	Nominal percentage [%]	Nominal weight [g]	Actual weight [g]	Actual percentage [%]
Paraffin Wax	85.20	68.473	68.473	85.201
Stearic Acid	10.00	8.046	8.047	10.001
Graphite	2.00	1.609	1.608	1.998
MgB90(20%Mg)	2.80	2.333	2.333	2.800

Test	Eq. 6.10	Eq. 6.11	Eq. 6.12
Test no. 01	+0.1%	-1.1%	+8.2%
Test no. 02	+1.1%	-5.7%	+4.3%
Test no. 03	+0.5%	-1.7%	+4.1%

Test	a_D	n_D	R^2
Test no. 01	3.976 ± 0.029	0.492 ± 0.003	1.000
Test no. 02	4.076 ± 0.068	0.605 ± 0.016	0.994
Test no. 03	4.071 ± 0.052	0.566 ± 0.011	0.997
Ensemble	4.062 ± 0.068	0.541 ± 0.012	0.988

Test	a_r	n_r	R^2
Test no. 01	.0001 ± .0000	1.936 ± .0038	0.964
Test no. 02	0.021 ± .0002	0.893 ± .0015	0.974
Test no. 03	0.009 ± .0001	1.065 ± .0018	0.973
Ensemble	0.003 ± .0000	1.310 ± .0033	0.942

B.8 SW w μAl (manufacturing Jan. 2012)

	Nominal percentage [%]	Nominal weight [g]	Actual weight [g]	Actual percentage [%]
Paraffin Wax	78.00	79.741	79.741	78.000
Stearic Acid	10.00	10.223	10.227	10.000
Graphite	2.00	2.045	2.043	2.000
μAl	10.00	10.223	10.227	10.000

Test	Eq. 6.10	Eq. 6.11	Eq. 6.12
Test no. 01	+0.0%	+2.5%	-2.3%
Test no. 02	+0.7%	-3.8%	+2.3%
Test no. 03	+0.0%	-3.4%	+4.5%

Test	a_D	n_D	R^2
Test no. 01	4.284 ± 0.032	0.646 ± 0.006	0.998
Test no. 02	4.115 ± 0.046	0.624 ± 0.010	0.996
Test no. 03	4.291 ± 0.026	0.573 ± 0.006	0.997
Ensemble	4.211 ± 0.039	0.612 ± 0.008	0.995

Test	a_r	n_r	R^2
Test no. 01	0.035 ± .0003	0.801 ± .0014	0.970
Test no. 02	0.027 ± .0002	0.841 ± .0016	0.966
Test no. 03	0.014 ± .0001	0.980 ± .0016	0.974
Ensemble	0.025 ± .0002	0.867 ± .0016	0.968

B.9 SW w μAl Flaked (manufacturing Jan. 2012)

	Nominal percentage [%]	Nominal weight [g]	Actual weight [g]	Actual percentage [%]
Paraffin Wax	78.00	79.597	79.597	78.001
Stearic Acid	10.00	10.205	10.207	10.002
Graphite	2.00	2.041	2.040	1.999
μAl Flaked	10.00	10.205	10.202	9.997

Test	Eq. 6.10	Eq. 6.11	Eq. 6.12
Test no. 01	+0.1%	-1.7%	+3.5%
Test no. 02	-0.2%	+0.3%	+1.6%
Test no. 03	+0.2%	-3.2%	+1.0%

Test	a_D	n_D	R^2
Test no. 01	3.817 ± 0.028	0.603 ± 0.006	0.997
Test no. 02	3.970 ± 0.022	0.589 ± 0.005	0.999
Test no. 03	3.893 ± 0.033	0.680 ± 0.007	0.998
Ensemble	3.877 ± 0.044	0.624 ± 0.010	0.994

Test	a_r	n_r	R^2
Test no. 01	0.010 ± .0001	1.028 ± .0023	0.954
Test no. 02	0.013 ± .0001	0.967 ± .0015	0.978
Test no. 03	0.035 ± .0003	0.774 ± .0016	0.957
Ensemble	0.016 ± .0002	0.936 ± .0021	0.951

B.10 SW w nFe (manufacturing Oct. 2011)

	Nominal percentage [%]	Nominal weight [g]	Actual weight [g]	Actual percentage [%]
Paraffin Wax	83.00	52.142	52.142	83.000
Stearic Acid	10.00	6.282	6.282	10.000
Graphite	2.00	1.256	1.256	2.000
nFe	5.00	3.141	3.141	5.000

Test	Eq. 6.10	Eq. 6.11	Eq. 6.12
Test no. 01	+1.3%	-1.8%	-0.2%
Test no. 02	+0.2%	-1.7%	+4.2%
Test no. 03	+0.5%	-4.6%	+7.0%

Test	a_D	n_D	R^2
Test no. 01	4.743 ± 0.036	0.583 ± 0.011	0.997
Test no. 02	3.688 ± 0.039	0.638 ± 0.006	0.999
Test no. 03	4.915 ± 0.071	0.550 ± 0.012	0.991
Ensemble	4.567 ± 0.129	0.630 ± 0.022	0.965

Test	a_r	n_r	R^2
Test no. 01	0.055 ± .0002	0.735 ± .0007	0.992
Test no. 02	0.004 ± .0001	1.195 ± .0035	0.920
Test no. 03	0.013 ± .0001	1.060 ± .0019	0.967
Ensemble	0.033 ± .0005	0.844 ± .0027	0.909

NOMENCLATURE

Acronyms

$3LAH$ Lithium aluminum exahydride

$AMROC$ American rocket society

AP Ammonium perchlorate

ASD Aluminum spherical dispersed

BET Specific surface area analysis

CCP Condensed combustion products

$GIRD$ Gruppa Isutcheniya Reaktinovo Dvisheniya (Group of Investigation on Reactive Motion)

GOX Gaseous Oxygen

$HAST$ High altitude supersonic target

$HTPB$ Hydroxyl-terminated polybutadiene

LAH Lithium aluminum hydride

LOX Liquid Oxygen

$NASA$ National aeronautics and space administration

$ORPHEE$	Operational research project on hybrid engine in Europe
PB	Polibutadiene
$RFNA$	Red fuming nitric acid
$RP-1$	Rocket Propellant-1
SA	Stearic acid
SEM	Scanning Electron Microscope
SW	Solid paraffin wax fuel
TOT	Thickness Over Time
w/o	Without

Greek Symbols

α	Absorption coefficient, m^{-1}
δ	Characteristic thermal thickness, mm
γ	Ratio between the specific heats
κ	Thermal diffusivity, m^2/s
μ	Dynamic viscosity, $Pa \cdot s$
ρ	Density, kg/m^3
σ	Stefan-Boltzmann constant, W/m^2K^4
ε	Emissivity coefficient

Physical quantities

Δh	Enthalpy absorbed in the combustion, J/kg
Δh_1	Heat of depolymerization process, J/kg
Δh_2	Latent heat of gasification of the monomers, J/kg
$\dot{m}$	Mass flow rate, kg/s
$\dot{q}$	Heat flux, W/m^2
a_D	First power law interpolation coefficient (diameters)

A_f	Combustion surface, mm^2
a_r	First power law interpolation coefficient (regression rate)
B	Blowing parameter
C_{f0}	Coefficient of friction without blowing
C_f	Coefficient of friction
C_h	Stanton number
c_p	Specific heat, J/kgK
D	Central perforation port diameter, mm
D_0	Initial central port diameter, mm
G	Mass flux, kg/m^2s
g_0	Gravity acceleration at the Earth's surface, m/s^2
h	Enthalpy, J/kg
I_{sp}	Specific impulse, s
k	Thermal conductivity, W/mK
L	Length of the fuel grain, mm
M	Gravity acceleration at the Earth's surface, m/s^2
n_D	Second power law interpolation coefficient (diameters)
n_r	Second power law interpolation coefficient (regression rate)
Nu	Nusselt number
O/F	Oxidizer to fuel ratio
p	Pressure, Pa
P_d	Dynamic pressure, Pa
Pr	Prandlt number
R	Universal gas constant, $J/kgmol$
r	Regression rate, mm/s

R^2	Fitting coefficient
Re	Reynolds number
T	Temperature, K
t	Time, s
u	Velocity, m/s

Subscripts

amb	Ambient
b	Burning
c	Chamber
$conv$	Convective
e	Free stream
ent	Entrainment
ex	Exhaust
f	Fuel
ff	First flame
g	Gas phase
i	Initial
ign	Ignition
l	Liquid phase
m	Melting
Ox	Oxidizer
rad	Radiative
s	Solid phase
v	Vaporization
w	Wall

BIBLIOGRAPHY

[1] L.T. De Luca, *Problemi energetici in propulsione aerospaziale, 1st Ed.*, Ch. 12, Politecnico di Milano, 2007.

[2] M. J. L. Turner, *Rocket and spacecraft propulsion, 3rd Ed.*, Springer, 2009.

[3] D. Altman, *Highlights in Hybrid Rocket History*, 10th International Workshop on Combustion and Propulsion, Lerici-La Spezia, 2003.

[4] L.T. De Luca, *Problemi energetici in propulsione aerospaziale, 1st Ed.*, Ch. 6, Politecnico di Milano, 2007.

[5] L.T. De Luca, *Problemi energetici in propulsione aerospaziale, 1st Ed.*, Ch. 9, Politecnico di Milano, 2007.

[6] G.P. Sutton, *Rocket propulsion elements, 6th Ed.*, John Wiley & Sons Inc., 1992.

[7] S.F. Sarner, *Propellant chemistry*, Reinhold Publishing Corporation, 1966.

[8] D. Altman, *Hybrid rocket development history*, 27th AIAA/ASME/SAE/ASEE Joint Propulsion Conference and Exhibit, AIAA Paper 91-2515 June 1991.

[9] G. A. Marxman and M. Gilbert, *Turbulent Boundary Layer Combustion in the Hybrid Rocket*, 9th International Symposium on Combustion, The Combustion Institute, 1963.

[10] G. A. Marxman, C.E. Wooldridge, and R.J. Muzzy, *Fundamentals of Hybrid Boundary Layer Combustion*, Heterogeneous Combustion Conference, December 1963.

[11] C. E. Wooldridge, G. A. Marxman, R. J. Kier, *Investigation of Combustion Instability in Hybrid Rockets*, NASA internal report, contract NAS 1-7310, Stanford Research Inst., 1969.

[12] Y. Maisonneuve e G. Lengellé, *Hybrid Propulsion: Past, Present and Future Perspectives*, 8th International Workshop on Combustion and Propulsion, Naples, June 2002.

[13] F. Maggi, G. Gariani, L. Galfetti, L.T. De Luca, *Theoretical analysis of hydrides in solid and hybrid rocket propulsion*, International journal of hydrogen energy Vol. 37, pp. 1760-1769, 2012.

[14] C. Oiknine, *New perspectives for hybrid propulsion*, 42th AIAA/ASME/SAE/ASEE Joint Propulsion Conference and Exhibit, AIAA Paper 2006-4674, July 2006.

[15] C. Paravan, M. Viscardi, L.T. De Luca, L.P. López, *Anisotropy Effects in Hybrid Fuels Burning in a Micro-Burner*, XX AIDAA Congress, 2009.

[16] D. Maggiolini, A. Monferini, *Indagine Sperimentale di Effetti della Radianza Emessa Spontaneamente sulla Balistica di Propellenti Solidi*, Tesi di Laurea in Ingegneria Aerospaziale, Politecnico di Milano, Dipartimento di Energetica, Milano, Dicembre 2003.

[17] G. Frangi, *Indagine Sperimentale di Combustibili Innovativi per Propellenti Ibridi*, Tesi di Laurea in Ingegneria Aerospaziale, Politecnico di Milano, Dipartimento di Energetica, Milano, Ottobre 2005.

[18] F. Bosisio, *Progettazione e Realizzazione di un Banco Sperimentale per un Microcombustore Ibrido*, Tesi di Laurea Specialistica in Ingegneria Aeronautica, Politecnico di Milano, Dipartimento di Energetica, Milano, Aprile 2007.

[19] H. Raina, *Caratterizzazione e Sperimentazione di Additivi Energetici Innovativi per la Propulsione Ibrida*, Tesi di Laurea Specialistica in Ingegneria Aeronautica, Politecnico di Milano, Dipartimento di Energetica, Milano, Dicembre 2007.

[20] L.T. De Luca, L. Galfetti, G. Colombo, F. Maggi, A. Bandera, M. Boiocchi, G. Gariani, L. Merotto, C. Paravan, A. Reina, *Time-Resolved Burning of Solid Fuels for Hybrid Rocket Propulsion*, EUCASS Book 2010.

[21] C. Paravan, *Ballistics of innovative solid fuel formulations for hybrid rocket engines*, PhD Dissertation, Politecnico di Milano, Dipartimento di Ingegneria Aerospaziale, Milano, 2012.

[22] C. Paravan, *Effetti dell'anisotropia nei combustibili a base di paraffina per la propulsione ibrida*, Tesi di Laurea in Ingegneria Aerospaziale, Politecnico di Milano, Dipartimento di Ingegneria Aerospaziale, Milano, Aprile 2008.

[23] A. Reina,, G. Colombo, L.T. De Luca, F. Maggi, I. Lesniak, D.B. Lempert, and G.B. Manelis, *Magnesium and Aluminum Ignition in CO2 Atmosphere*, XX AIDAA Congress, 2009.

[24] T.J. Houser, M.V. Peck, *Research in Hybrid Combustion*, AIAA Progress in Astronautics and Aeronautics, Heterogeneous Combustion, Vol. 15, Pp. 559-581, 1964.

[25] C. Paravan, A. Sossi, A Reina, G. Massini, M. Manzoni, E. Duranti, G. Rambaldi, A. Adami, E. Seletti, L.T. De Luca, *Micro and Nano-sized Metal Additives for Solid Fuels in Hybrid Rocket Lab-scale Burner*, EUCASS Book 2011.

[26] S. Himran, A. Suwono, G.Ali Mansoori, *Characterization of Alkanes and Paraffin Waxes for Application as Phase Change Energy Storage Medium*, Energy Sources Vol. 16, Taylor & Francis, 1994.

[27] M. A. Karabeyoglu, D. Altman *Combustion of Liquefying Hybrid Propellants: Part 1, General Theory*, Journal of propulsion and power Vol. 18, No. 3, May–June 2002.

[28] M. A. Karabeyoglu, D. Altman *Combustion of Liquefying Hybrid Propellants: Part 2, Stability of Liquid Films*, Journal of propulsion and power Vol. 18, No. 3, May–June 2002.

[29] M. A. Karabeyoglu, D. Altman *Development and testing of paraffin-based hybrid rocket fuels*, 37th AIAA/ASME/SAE/ASEE Joint Propulsion Conference and Exhibit, AIAA Paper 2001-4503, July 2001.

[30] A. A. Gromov, Y. I. Strokova, T. A. Khabas, A. G. Melnikov, H-J. Ritzhaupt-Kleissl *Combustion of the "$Ti - TiO_2$" and "$Ti - Al$" powdery mixtures in air*, Journal of the European Ceramic Society Vol. 28, 2008.

[31] D. A. Yagodnikov and E. I. Gusachenko, *Experimental Study of the Disperse Composition of Condensed Products of Aluminum-Particle Combustion in Air*, Combustion, Explosion, and Shock Waves, Vol. 40, No. 2, 2004.

[32] L. D. Smoot, C. F. Price, *Regression Rates of Nonmetalized Hybrid Fuels Systems*, AIAA Journal, Vol. 3, No. 8, August 1965.

[33] K.K. Kuo, Y.C. Lu, M.J. Chiaverini, D.K. Johnson, N. Serin, e G.A. Risha, *Fundamental Phenomena on Fuel Decomposition and Boundary-Layer Combustion Processes with Applications to Hybrid Rocket Motors, Part I: Experimental Investigation*, Final Report, Propulsion Engineering Research Center, June 1996.

[34] J. D. DeSain, T. J. Curtiss, R. B. Cohen, B. B. Brady, S. A. Frolik, *Testing of $LiAlH_4$ as a Potential Additive to Paraffin Wax Hybrid Rocket Fuel*, The Aerospace Corporation, Aerospace Report No. TR-2008(8506)-1, October 2007.

[35] J. D. DeSain, T. J. Curtiss, K. M. Metzler, B. B. Brady, *Testing Hypergolic Ignition of Paraffin Wax / $LiAlH_4$ Mixtures*, 46th AIAA/ASME/SAE/ASEE Joint Propulsion Conference and Exhibit, AIAA Paper 2010-6636, July 2010.

[36] A. McCormick, E. Hultgren, M. Lichtman, J. Smith, R. Sneed, S. Azimi, *TDesign, Optimization, and Launch of a 3″ Diameter N_2O/Aluminized Paraffin Rocket*, 41th AIAA/ASME/SAE/ASEE Joint Propulsion Conference and Exhibit, AIAA Paper 2005-4095, July 2005.

[37] L.T. De Luca, L. Galfetti, F. Severini, L. Rossettini, L. Meda, G. Marra, B. D'Andrea, V. Weiser, M. Calabro, A.B. Vorozhtsov, A.A. Glauznov, G.J. Pavlovets, *Physical and Ballistic Characterization of AlH3-based Space Propellants*, Aerospace Science and Technology, No. 11, pp. 18-25, 2007.

[38] Grant A. Risha, B. J. Evans, E. Boyer, R. B. Wehrman, K. K. Kuo, *Nano-sized aluminum and boron-based solid fuel characterization in a hybrid rocket engine*, 39th AIAA/ASME/SAE/ASEE Joint Propulsion Conference and Exhibit, AIAA Paper 2003-4593, July 2003.

[39] A.Gany, *Scale effects in hybrid motors under similarity conditions*, 32th AIAA/ASME/SAE/ASEE Joint Propulsion Conference and Exhibit,AIAA Paper 96-2846 July 1996.

[40] Advanced Powder Technologies, *Advanced Powder Technologies website*, web address
http://www.nanosized-powders.com/multimedia.

[41] Chemetall GmBH, *Chemetall GmBH website*, web address
http://www.chemetall.com.

[42] MACH I Chemicals, *Mach I website*, web address http://www.machichemicals.com.

[43] *SpaceShipTwo*, SpaceShipTwo *website*, web address http://www.spaceshiptwo.net.

[44] Scaled Composites, *Scaled Composites website*, web address http://www.scaled.com.